An experimental and theoretical investigation of cell cryobiological characteristics and optimal cryopreservation technology

Ji Peng

A dissertation

submitted in partial fulfillment of the

requirements for the degree of

Doctor of Philosophy

University of Washington

2021

Reading Committee:

Dayong Gao, Chair

Jaehyun Chung

Zhiquan Shu

Program Authorized to Offer Degree:

Mechanical Engineering

University of Washington

Abstract

An experimental and theoretical investigation of cell cryobiological characteristics and optimal cryopreservation technology

Ji Peng

Chair of the Supervisory Committee:
Professor Dayong Gao
Mechanical Engineering

Cryopreservation at low temperatures (e.g., in liquid nitrogen) has been proved to be the most reliable and sometimes possibly the only way to preserve cells and tissues alive for months, years, decades, or even centuries. Generally, a cryopreservation process includes a few essential steps, such as the addition of cryoprotective agent (CPA) before the freezing process, the cooling/rewarming of the sample with optimal rates, and removal of CPA after the thawing process, in which cells experience a series of highly stressed conditions, causing injury to cells. Scientists rely on the theoretical interpretation of bio-heat and mass transfer and novel measurement techniques to design the optimal cryopreservation protocol. In this dissertation, several novel devices and methods developed to analyze the fundamentals of cryobiology, determine cryobiological properties of cells, and optimize cryopreservation protocols are discussed.

A microfluidic device with on-chip cooling/heating mechanism, enabling precise and stable temperature control, was developed. A multiphysics simulation of three-dimensional laminar flow conjugated heat transfer, coupled with Joule heating, was conducted. The temperature control stability and response were tested and demonstrated. This platform achieves the following features: (1) hydrodynamic confinement of the single-cell; (2) switching extracellular medium during the cell trapping; (3) controlling surrounding medium temperature from 2 ℃ to 37℃.

A simplified microfluidic device was employed to determine the cell membrane permeabilities of Jurkat cell at room temperature, where a microfluidic chip with a block structure was used to achieve steady trapping. The cell membrane permeabilities of Jurkat cells to water and CPA were determined through simulation and image processing analysis with cell volume excursion captured by a high-speed camera.

A multifunctional cell processing system and related auto-generated CPA removal protocol are proposed to achieve both CPA removal and cell concentration functions. By applying optional hypertonic dilution and an advanced algorithm with cell properties, determined by devices discussed above, as parameters, the optimal CPA removal approach will be generated to minimize cell shrinkage and swelling during the post-cryopreservation process.

Heat transfer models for water-bath and natural air rewarming processes for large samples were developed and validated by experiments. The validated models were then employed to calculate the temperature gradients spatially and temporally. Based on temperature gradient results, natural air rewarming is a better tissue and organ cryopreservation method with relatively more minor thermal stress during rewarming. Specific suggestions about the sample's location in the container and the size of the container were also discussed.

An inverse method to determine the subzero L_p and E_a with cell recovery rate results and water transport model is proposed. The subzero L_p and E_a of Jurkat cells were determined and discussed. The methodology is meaningful for the fundamental research of cryobiology.

The limitations of proposed devices and methods are discussed. Future work is presented, including more biological experiments of new-developed devices, advanced heat transfer models, and the relation of cryobiological properties.

TABLE OF CONTENTS

LIST OF FIGURES

LIST OF TABLES

ACKNOWLEDGEMENTS

I would like to express my earnest gratitude to my supervisor Prof. Dayong Gao, for his great guidance, support, and encouragement throughout my Ph. D. research and life.

I would like to express my sincere appreciation to the other two committee members: Prof. Jae-Hyun Chung and Prof. Yong Tan, for their expertise and suggestions.

I would like to thank Prof. Zhiquan Shu for serving as one of my committee members and helping me in all aspects as a mentor, a friend, and a big brother.

I would like to thank Dr. Shen Ren for his contributions and helps to my research and work. I would like to thank Dr. Cifeng Fang and Dr. Jiaji Pan for their guidance in my Ph. D. career. I also would like to thank all labmates: Dr. Jinyuan Zhang, Praveen Sekar, Ruidong Ma, Ye Jin, Ziyuan Wang, Shaohang Hao, Nanye Du, Alexander Novokhodko, Xiao Ma, Yanyi Wang, Leo Tao, for all their help and support for this work.

Especially, I give my special thanks to my family for their endless support, trust, and encouragement.

DEDICATION

To my dear wife, Tingzhi Fang.

To my family.

To Muffin, you are the cutest.

Chapter 1. INTRODUCTION

1.1 CRYOBIOLOGY AND CRYOPRESERVATION

Cryobiology is a multidisciplinary science to study the physical and biological behaviors of biological materials, including cells, tissues, and organs, and their interaction with the environment at low temperature (especially less than the freezing point of water, 0℃). Any chemical reactions and metabolism of living cells will be slowed down or even paused at low temperatures, which permits the long-term preservation of these biological materials[1]. The "life clock" of these materials will be resumed after thawing to normal temperature. The application and research of this technology and science started from 1949 when Polge et al. found rooster sperm can survive in liquid nitrogen with glycerol[2]. Since then, cryopreservation has been applied for long-term storage of DNA/RNA, proteins, bio-fluids, cells, tissues, and organs by scientists and engineers from various fields, benefiting fundamental research and clinical practice. For example, cryopreservation of stem cells (from bone marrow, cord blood, or peripheral blood) is one of the most important cryobiology applications. Collected stem cells have been cryopreserved and then further used to cure various diseases, including Hodgkin's and non-Hodgkin's lymphoma[3-5], myeloid or lymphoblastic leukemia[5-7], and solid tumors (testis, breast) [4, 5, 7–9]. Other successfully cryopreserved biological material includes red blood cells and platelets[10], sperms[11], oocytes[12-13], liver cells[14], adipose tissue[15], etc.

The implementation of cryopreservation provides continuous supply of biological materials for scientific research, possible banking of a large number of cells, tissues, and even organs for human leukocyte antigen typing and matching between recipients and donors, safe transport of

cells/tissues between different medical centers, and more sufficient time for the screening of transmissible diseases in the donated cells and tissues before transplantation.

1.2 GENERAL PROCEDURES OF CRYOPRESERVATION

Generally, a cryopreservation process includes a few essential steps (Fig. 1.1) : (1) Loading cryoprotective agent (CPA) to the cell suspension; (2) Freezing the cell suspension with a specific protocol (Cooling, ice seeding, and freezing); (3) Storing the samples at low temperatures; (4) Thawing the frozen samples; (5) Removal of CPA.

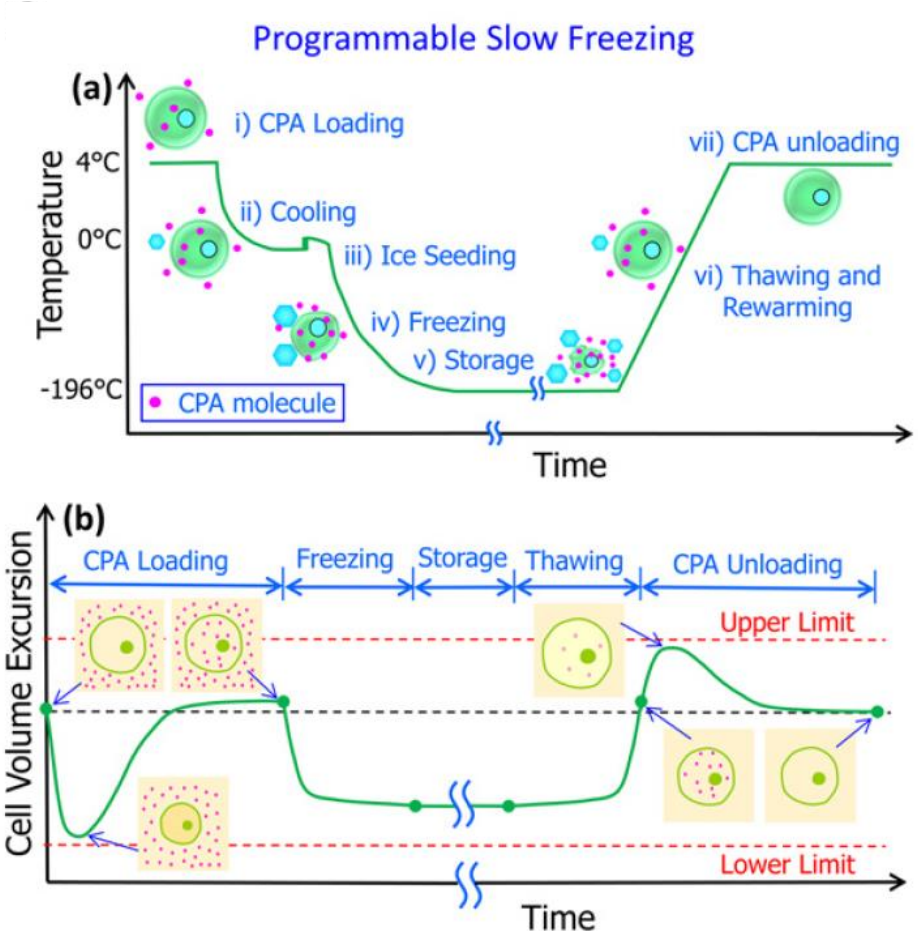

Figure 1.1. Typical temperature profiles (a) and cell volume excursion (b) for slow programable freezing[16].

To decrease cryoinjuries, cryoprotective agents (CPA) need to be added to cell suspension before freezing. Since the first use of glycerol as CPA in 1949 [2], more than 100 types of CPAs have been used, such as glycerol, dimethyl sulfoxide (DMSO), ethylene glycol (EG), propylene glycol (PG), trehalose, sucrose, dextran, hydroxyethyl starch (HES), Polyvinylpyrrolidone (PVP), and so on. They can be mainly classified into two types:

(1) Permeable CPAs, such as glycerol, DMSO, EG, and PG. The mechanism of permeable CPAs is to penetrate cells by intra- and extracellular concentration difference. Firstly, permeable CPAs can inhibit intracellular ice formation and decrease colligatively the freezing temperature of the intracellular environment. On the other hand, by filling in the intracellular volume to compensate for the volume reduction due to water loss, permeable CPAs can prevent severe cell dehydration injury and stabilize protein 3D-structure.

(2) Non-permeable CPAs, such as sucrose, trehalose, dextran, HES, PVP, and albumins. These CPAs cannot penetrate into cells. Their primary function is to inhibit extracellular ice formation and enhance vitrification by increasing the glass transition temperature (Tg) and the extracellular environment's glass transition tendency. Non-permeable CPAs can protect cell membrane integrity and form protective shells around cells. Albumins can also prevent cell and protein aggregation.

To select an optimal CPA for a specific type of cell, one should consider: (1) the permeability of the cell membrane to the CPA; (2) the toxicity of the CPA to the cells; and (3) the availability and cost of the CPA.

1.3 CHALLENGES IN CRYOPRESERVATION

Besides storage at low temperatures, the other four steps could be harmful to the biological material[11,17-18]. “Two-Factor Hypothesis” of cryoinjury, as shown in Figure 1.2, was proposed by Dr. Mazur, which described the cryoinjury mechanisms during the freezing process[19]. When a cell is cooled to subzero temperature, the extracellular ice forms first and decreases the fraction of water in the cell suspension, increasing extracellular osmolarity. The difference in osmolarity caused by extracellular ice formation and the chemical potential of water between intra- and extracellular solution drives the influx of water across cell membranes. If the cooling rate is too high, there is not enough time for water efflux before intracellular ice formation (IIF). IIF may be fatal to cells, which is called “ice injury.”

On the other hand, if the cooling rate is too low, water can keep leaving the cells to reach the balance of osmolarity/water chemical potential, causing the intracellular electrolyte concentration to become very high. A high concentration of intracellular electrolytes can be toxic to cells called “solution injury.” Meanwhile, slow cooling may cause severe cell dehydration and shrinkage, exceeding the excursion tolerance limit.

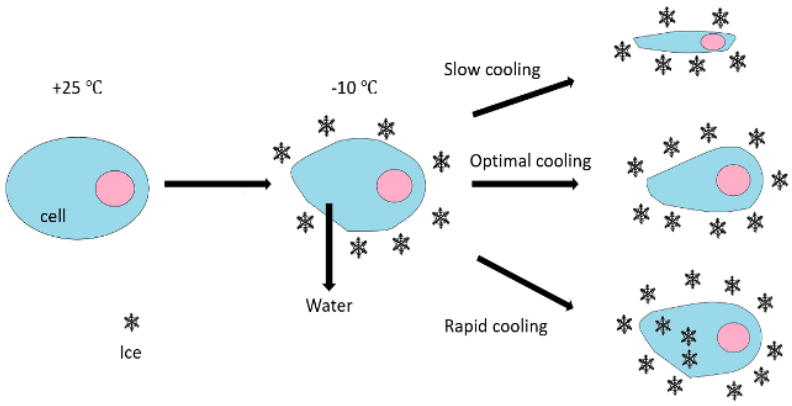

Figure 1.2. “Two-Factor Hypothesis” of cryoinjury

Even if biological samples could survive through the cooling process to the low temperatures, they still have to face challenges caused by warming and thawing. Like the cooling rate in the freezing procedure, the rewarming rate plays a vital role in the survival of biomaterials during thawing. Rapid thawing can rescue many cells, possibly because it can prevent the growth of tiny intracellular ice crystals into harmful large ice (i.e., so-called recrystallization, which can damage the membrane and lead to cell death)[20].

During the process of CPA addition and removal, the biological materials will also face two main challenges. Firstly, some CPAs, such as DMSO, are toxic at suprazero temperature for biological materials. DMSO has become the most widely used cryoprotective agent in the cryopreservation of cells and tissues since 1959[21]. However, toxicity and side effects related to DMSO in clinical practice and biological research have been widely reported, from mild discomfort to fatality in a dose-dependent manner. It was reported that DMSO plays multiple roles in cellular functions and cell growth by affecting metabolism, enzymatic activity, cell cycle, and apoptosis [22-23]. In this case, these two processes should be operated within a short time. Secondly, CPA addition and removal may cause osmotic injury by severe osmotic shift.

In conclusion, to cryopreserve the biological materials successfully, cell-type-specific optimal protocols to prevent all these possible injuries need to be determined.

1.4 CELL MEMBRANE PROPERTIES

The biophysical properties include the cell membrane permeability coefficients to water L_p and CPAs (P_s), the dependence of these properties on temperature or the activation energies of these permeability coefficients (E_a) [2,3]. The determination of such intrinsic cell membrane transport properties is essential for developing optimal cryopreservation in the following three aspects: (I) It helps select the optimal CPA for certain cell types. Generally, it's preferred to use

the CPA with large P_s and low toxicity for the cell type; (II) It helps to optimize the procedures of CPA addition and removal. P_s and L_p reflect how fast the CPA and water transfer across the cell membrane, critical for cell volume excursion during the CPA addition and removal procedures. With such L_p and P_s values determined, we can develop the optimal CPA addition/removal protocol, minimizing both the osmotic injury to the cell and cytotoxicity (the longer of exposure time in the CPA, the higher toxicity to the cells); (III) It helps to optimize the cooling process in cryopreservation, which can minimize the intracellular ice formation and solute injuries during cooling.

1.5 OUTLINE OF THIS DISSERTATION

The structure of the dissertation is shown below.

In chapter 2, a microfluidic device with on-chip cooling/heating mechanism, enabling precise and stable temperature control, was developed. A multiphysics simulation of three-dimensional laminar flow conjugated heat transfer, coupled with Joule heating, was conducted. The temperature control stability and response were tested and demonstrated. This platform achieves the following features: (1) hydrodynamic confinement of single-cell; (2) switching extracellular medium during the cell trapping; (3) controlling surrounding medium temperature from 2 ℃ to 37℃.

Chapter 3 shows a simplified microfluidic device employed to determine the cell membrane permeability of Jurkat cell at room temperature. A microfluidic chip with a block structure was used to achieve steady trapping. The cell volume excursion by a high-speed camera and the cell membrane permeability of Jurkat cells to water and CPA (DMSO) were determined through simulation and image processing analysis.

A multifunctional cell processing system and related auto-generated CPA removal protocol were proposed in chapter 4, achieving both CPA removal and cell concentration functions.

Applying optional hypertonic dilution and an advanced algorithm with cell properties, determined by devices discussed above, as parameters, the optimal CPA removal approach will be generated to minimize cell shrinkage and swelling during the post-cryopreservation process. Experiments validated the functionality of the system.

In chapter 5, heat transfer models for water-bath and natural air rewarming processes for a large sample are developed and validated by the experiment. The validated models were then employed to calculate the temperature gradients spatially and temporally. The temperature gradients results showed that natural air rewarming is a better method for tissue and organ cryopreservation, which has relatively more minor thermal stress during rewarming. Some suggestions about the sample's location in the container and the size of the container were also discussed.

In chapter 6, an inverse method to determine the subzero L_p and E_a with cell recovery rate results and water transport model is proposed. The subzero of L_p and E_a of Jurkat cells were determined and compared with previous literature.

The microfluidics devices are employed to determine the cell membrane permeabilities, including Lp and Ps, used in the applications of the following chapters. The L_p and P_s of Jurkat cells work as crucial parameters in two-parameter formalism, the cell volume excursion model during CPA removal, in chapter 4. The L_p and related temperature work as reference temperature and L_p in the Arrhenius equation, the cell volume excursion model during the cooling process, in chapter 6.

In the last chapter, the proposed device's limitations and some potential research of cryopreservation are described.

Chapter 2. DEVELOPMENT OF A MICROFLUIDIC DEVICE WITH PRECISE ON-CHIP TEMPERATURE CONTROL BY INTEGRATED COOLING AND HEATING COMPONENTS FOR SINGLE CELL-BASED ANALYSIS

2.1 INTRODUCTION

Generally, a cryopreservation process includes a few essential steps, such as the addition of cryoprotective agent (CPA) before the freezing process, the cooling/rewarming of the sample with optimal rates, and removal of CPA after the thawing process, in which cells experience a series of highly stressed conditions, causing injury to cells.[25] To obtain the optimal protocol for cryopreservation, the cell-type-specific cryobiological properties need to be determined first. These biophysical properties include the cell membrane permeability coefficients to water L_p and CPAs (P_s), the dependence of these properties on temperature or the activation energies of these permeability coefficients (E_a) [2,3].

The determination of such intrinsic cell membrane transport properties is essential for developing optimal cryopreservation in the following three aspects: (I) It helps select the optimal CPA for certain cell types. Generally, it is preferred to use the CPA with large P_s and low toxicity for the cell type; (II) It helps to optimize the procedures of CPA addition and removal. P_s and L_p reflect how fast the CPA and water transfer across the cell membrane, critical for cell volume excursion during the CPA addition and removal procedures. With such L_p and P_s values determined, we can develop the optimal CPA addition/removal protocol, minimizing both the osmotic injury to the cell and cytotoxicity (the longer of exposure time in the CPA, the higher

toxicity to the cells); (III) It helps to optimize the cooling process in cryopreservation, which can minimize intracellular ice formation and solute injuries during cooling.

Some early work has been done to understand these properties. Chen[26] measured DC membrane permeability coefficients to water and DMSO with a microfluidic perfusion system. Fang[27] developed an integrated microfluidic system to determine the temperature dependence of membrane permeability of human acute lymphoblastic leukemia cells.

Due to the lack of a reliable on-chip cooling mechanism, present microfluidic systems mostly measure L_p and P_s of interested cells at room temperature or above[4, 5]. Limited successes have been achieved in our group in determining these properties below room temperature as to the challenges of temperature control precision with active cooling[4, 6]. However, as some CPAs, DMSO, for instance, have significant cytotoxicity at room temperature or above. To prevent cytotoxic damage, the CPA addition process for cell cryopreservation is usually conducted at relatively low temperatures, e.g., 4℃.[29] Furthermore, cell membrane permeability changes unpredictably in an extensive temperature range due to membrane phase transition, during which E_a changes[8, 9]. The cell membrane phase transition might happen at different temperatures for various cell types. For example, the membrane phase transition of human oocytes occurs around 16.9℃.[30] In this scenario, using the extrapolation method to calculate L_p and P_s near 0℃ with data collected at room temperature or higher is inaccurate. In a word, a device with precise temperature control for the determination of cell membrane permeability at temperatures below room temperature is in crucial need.

Since temperature variations significantly affect the intrinsic properties of fluids and cells, on-chip temperature control is necessary for stable operations inside microfluidic devices. The cooling mechanism in microfluidic devices can be classified into off-device cooling and on-device cooling

by the design nature. Typically, off-device cooling regards the cooling design that cools down the microfluidic device's environment, for instance, by placing a cooling bath under the microfluidic chip—a microfluidic perfusion system to probe Megakaryocyte membrane transport properties below 0 ℃[28]. Chen[26] used the off-device cooling method to measure properties of Dendritic cell membranes at 12 ℃, 22 ℃, 25 ℃, 32 ℃. However, because of the considerable heat resistance of glass, the heat flux across glass is low, resulting in the slow response of temperature control. Therefore, the on-device cooling method is usually preferred. So far, there are some novel approaches to remove excess heat from hot spots of integrated circuit chips with advanced thermal dissipation technology and prevent the chips from being overheated with the working fluid[10,11]. For example, taking advantage of a large amount of latent heat during the working fluid's vaporization, the ultra-rapid cooling rate in the devices can be more than 10^4 ℃ per min with two-phase cooling agents[10,11].

Nevertheless, the vaporization process makes it hard to observe the cell boundary in image processing, a fundamental approach to calculate the cell volume excursion. Besides, the gas generated by vaporization would highly increase the channel's air pressure, which might damage the whole device. Therefore, to achieve a high rate of heat transfer, the on-device cooling method is preferred, in which the coolant directly contacts the target components. Compared with the conventional off-device cooling method, these novel on-device microfluidic cooling systems have lower heat resistance and higher heat flux.

Another known issue for on-chip temperature control below room temperature is the long settling time if only active cooling is presented in the system, which can be avoided by integrating on-chip active heating into the device. Together with the temperature sensor, a two-way active cooling and heating system is required to achieve quick settling and precise on-chip temperature

control. Previous researches achieved on-device temperature control either globally, by preheating the carrying fluid[34] inside the device, using a printed wiring board (PWB) heating unit under the entire microfluidic device[35]; or locally, through the micropatterning wire on a silicon substrate[14-16] and glass substrate[17-20]. These devices, while can accomplish precise temperature control on the order of ~10 mm, are difficult to achieve rapid responding and precise localized temperature control in a small and confined area ($\sim 10 \mu m^2$). Besides limitation at temperature control scale, global temperature control generally measures the temperature outside the microchannel by using a thermocouple and then utilizes a Peltier element to control the temperature of a thermal stabilizing stage, which lacks exact measurement of transient temperature variation inside the microchannel, causing obtuse temperature feedback and slow cooling and heating at a rate around 10℃/min, with temperature stability in the range of 1 ℃.[43]

In conclusion, it is still challenging to conduct the single cell-based analysis at a specific stable temperature below room temperature because an on-chip cooling mechanism with precise temperature control is still unavailable. In our opinion, the quick response of on-chip temperature control, high accuracy of local temperature monitoring, and real-time observation ease are the indispensable design requirements of such kinds of devices for the study.

A multiphysics simulation of three-dimensional laminar flow conjugated heat transfer coupled with Joule heating was conducted in this study. A microfluidic device with on-chip cooling/heating mechanism, enabling precise and stable temperature control, was fabricated. The temperature control stability and response were tested and demonstrated.

2.2 MATERIAL AND METHOD

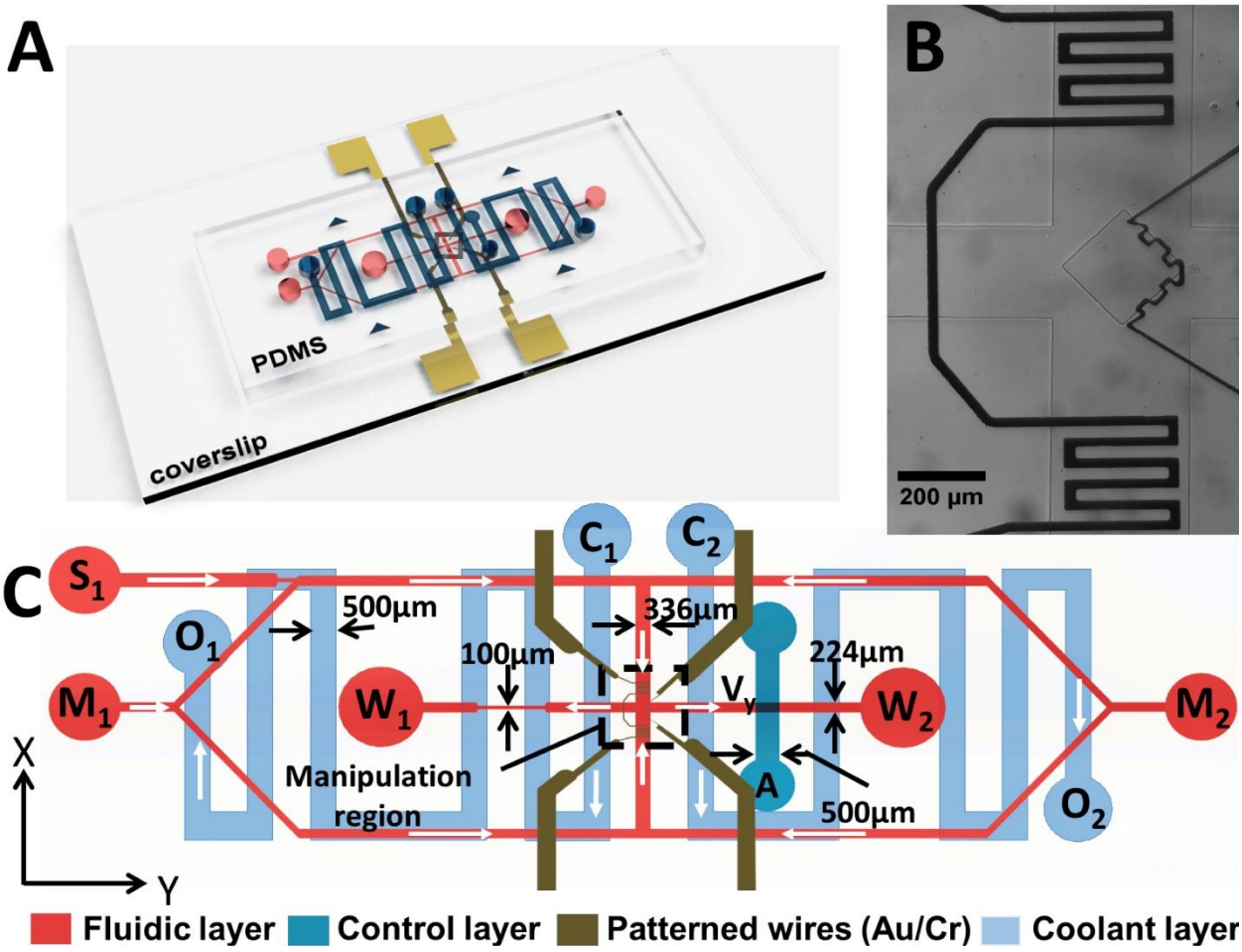

Figure 2.1. Microfluidic platform with the integrated flow and temperature control: (A) 3D rendering illustration of the microfluidic device, showing the glass slide etched with gold wires, double-layered PDMS with microchannels; (B) Microscope picture showing an enlarged view of the boxed region: microheater (rest on the side) and the temperature sensor (sitting at the cross-slot region); (C) Plane view of the microfluidic device, showing: media inlets M_1, M_2; cell inlet S_1; waste outlets W_1, W_2; valve pressure regulation port A.

2.2.1 *Heat transfer modeling in micro-channel*

Figure 2.1 shows the schematics of the device in this analysis. Figures 2.1A and 2.1C show that the device consists of three layers: patterned wires, fluidic layer, control, and coolant layer. Cell suspension flows across the fluidic layer as a thin layer in the chip with a width to height ratio of 5:1. The heat transfer inside the fluidic layer is mainly in the vertical direction. The control and coolant layer is located at the top of the fluidic layer, and the heating circuit is regarded as a thin layer heating source below the fluidic layer. Cell suspension enters the channel at room temperature. The cooling agent's initial temperature is -40℃, and constant voltage (2.5V) is applied to the heating circuit. As to the low Reynolds number lower than 5 inside the micro-channel, the micro-channel fluid acts as laminar flow. To examine the spatial temperature profile created by on-chip active cooling/heating design, we conducted a multiphysics simulation (COMSOL Multiphysics, COMSOL, Inc., Stockholm, Sweden) laminar flow conjugated heat transfer, coupled with Joule heating. The heat transfer in the fluid is governed by

$$\rho C_p \frac{\partial T}{\partial t} + \rho C_p u \cdot \nabla T = \alpha_p T \left(\frac{\partial p_A}{\partial t} + u \cdot \nabla p_A \right) + \nabla \cdot (k \nabla T) + Q \tag{2.1}$$

where $\alpha_p T \left(\frac{\partial p_A}{\partial t} + u \cdot \nabla p_A \right)$ is the pressure term if the fluid density is temperature-dependent. Some assumptions are made to simplify the analysis: negligible viscous effect, the constant density of the fluid, no volumetric heat source term, and steady-state. The heat transfer equation of the fluid can finally be expressed as:

$$\rho C_p u \cdot \nabla T = \nabla \cdot (k \nabla T) \tag{2.2}$$

As for the heat transfer in PDMS and glass, the model of heat transfer in solid was applied, which is dominated by heat conduction

$$\frac{\partial}{\partial x} \left(k \frac{\partial T}{\partial x} \right) + Q = 0 \tag{2.3}$$

The heat source produced inside the microheater is given by $Q_J = J \cdot E = \sigma(\nabla V)^2$ where $J = \sigma E$ is the current density, $E = -\nabla V$ is the electric field, and σ is the electrical conductivity of the microheater. Q_J acts as a boundary heat flux for heat transfer in both solid and fluid.

2.2.2 *Evaluation of heat transfer coefficients in micro-channel*

The heat transfer between fluid and solid is mainly heat convection. The heat flux is described as

$$q'' = h(T_s - T_\infty) \tag{2.4}$$

Since the thermal resistance in the horizon direction is much larger than the vertical direction, as the thermal resistance ratio is 5:1, we assumed the design's heat flux is mainly in the vertical direction. Forced convection on a flat plate model was applied in our design. To evaluate the convective heat transfer coefficient, the Nusselt number in laminar flow is calculated as

$$Nu = 0.664 Re^{\frac{1}{2}} Pr^{\frac{1}{3}} \tag{2.5}$$

where Re is the Reynolds number ($Re = \frac{puD}{\mu}$) and Pr is Prandtl number ($Pr = \frac{C_p \mu}{k}$). Then, the heat transfer coefficient can be obtained ($h = \frac{k}{D} Nu$).

2.2.3 *Multiphysics simulation details*

To seek the coolant channel's optimal shape and dimensions and predict its cooling performance, the numerical simulation was operated first. As multiple physics included in this integrated design: (1) joule heating of gold wire, (2) heat transfer in the solid and fluid, (3) laminar flow inside the cooling channel, and sample channel, the numerical simulation involves multiphysics of joule heating, heat transfer, and fluid flow, with the coupling effect of electrical

heat and non-isothermal flow. The details of material properties used for the simulation are listed in Table 2.1. The boundary and initial conditions of simulation are shown in Figure 2.2 and Table 2.2. The electric circuit domain, coolant domain, and sample layer domain are marked as gold, blue, and red, respectively, in Figure 2.2.

Table 2.1: Material properties used for the Multiphysics simulation

Material	Thermal conductivity K $[Wm^{-1}K^{-1}]$	Heat capacity $C_p[Jkg^{-1}K^{-1}]$	Heat transfer coefficient h $[Wm^{-2}K^{-1}]$	Electrical conductivity $\sigma[Sm^{-1}]$
Gold	317	129	Not required	4.1×10^7
Glass	1.38	703	Not required	Not required
Water	0.56	4200	20	Not required
PDMS	0.15	1460	Not required	Not required
$CaCl_2$ (30%w/w)	493	2700	2019.4	Not required
Air	0.026	1005	0.5	Not required

Table 2.2: Values of boundary conditions

Boundary conditions	V_{ground}[V]	V_{source}[V]	H_{air} $[Wm^{-2}K^{-1}]$	T_{water}[K]	$T_{initial}$[K]	$T_{coolant}$[K]
Value	0	2.5	5	295	295	233

2.2.4 *Experimental Setup*

The fabrication for this system was described in detail in the previous study[27], which consists of several core steps, including patterning of conductive wire on the glass slide, fabrication of the double-layered PDMS microfluidic channel, and assembly of the device. The conductive wire patterning working as the microheater and the temperature sensor was made with a glass slide (EMF, CA-134) with a 1000 Å thick gold film on a 50 Å thick chrome adhesion layer. It was etched by gold etchant (TFA gold etchant, Tranxene) and chrome etchant (TFE chromium etchant, Tranxene) to the target patterning. A Keithley Integra Series 2700 digital multimeter (DMM) was used to detect the electrical resistance response versus temperature. According to the product information from the manufacturer, the ohms resolution of

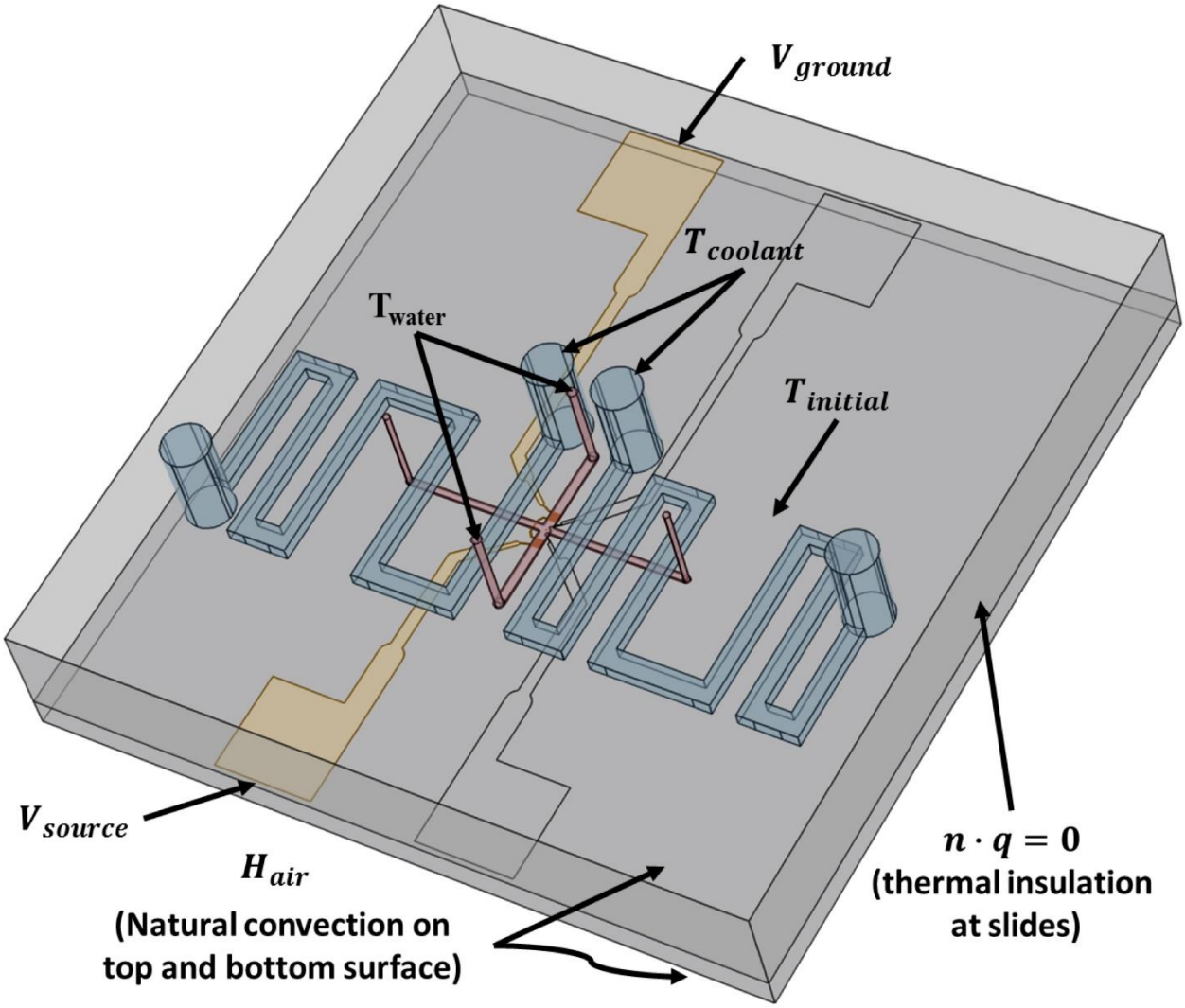

Figure 2.2. Schematic of the multiphysics simulation showing initial and boundary conditions: the gold domain indicating heater wire, the red domain showing the fluid channel, and the blue domain marking the cooling channel.

The multimeter is 100 $\mu\Omega$ resulting in a 1.5 mK resolution for the temperature sensor. Despite existing noises, the resolution satisfied our demand. The calibration process was performed for each sensor before each experiment. Because 37℃ is the physiological temperature of most mammals, adding the fact that cell analysis experiments are generally conducted at or below 37℃,[22-23], it was set as the upper limit temperature in our previous experiments[27].

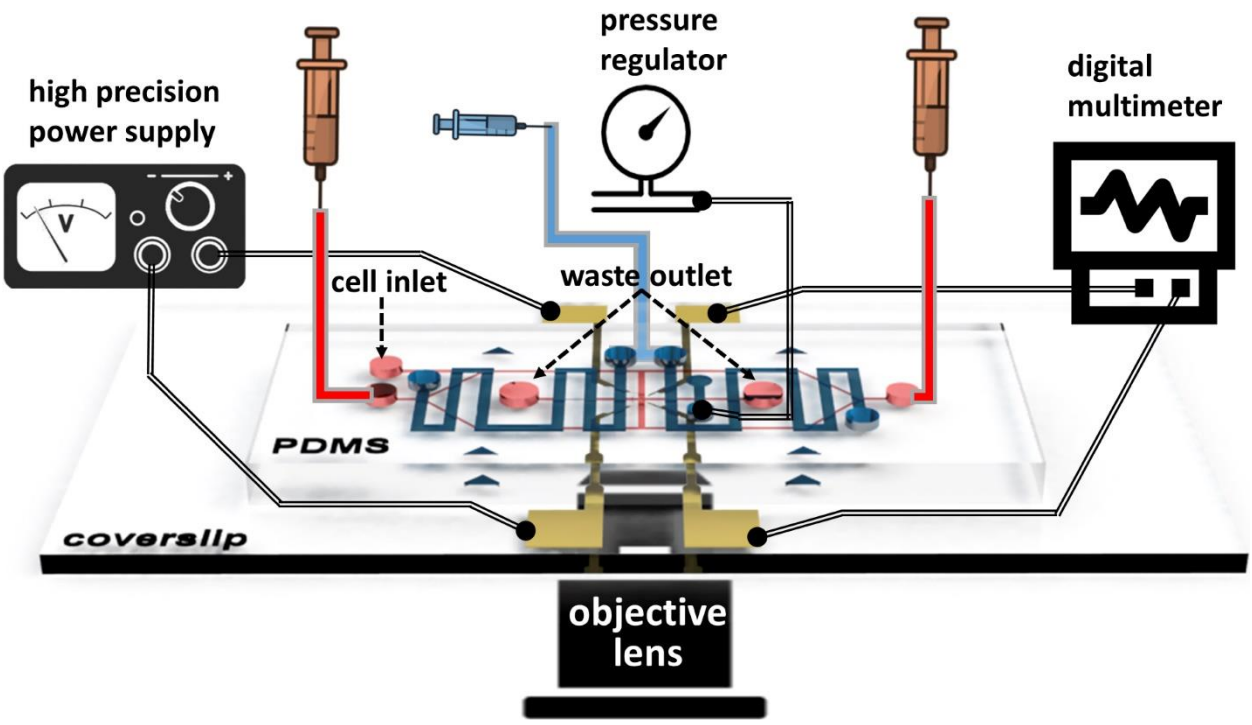

Figure 2.3. Schematic of the cell trapping and microfluidic manipulation platform with the integrated flow and temperature control: a gas regulator controls the fluid resistance in the fluidic channel by regulating the pressure inside the control channel; a syringe pump introduces fluid flow inside the fluidic channel; a high precision power supply and a digital multimeter are connected to the micropatterned wires. The microfluidic platform is placed on an inverted microscope equipped with a high-speed camera (Phantom V310, vision research). A custom-designed LabVIEW virtual interface remotely controls the entire system.

Compared to our previous study[27], an additional coolant channel, whose geometry was designed with simulation guidance, was fabricated in the device in this work. Such a system, including heating and cooling components integrated with precise control algorithms, can theoretically provide any desired temperature range for our cell analysis experiments. Simultaneous on-chip flow and temperature control were accomplished by employing a LabVIEW (National Instruments, Austin, TX) virtual interface that communicated with pressure

regulator, temperature controller, and a digital multimeter (Figure 2.3), which was described in detail in the previous studies. Briefly, the cell can be trapped in the flow's stagnation point by a pressure regulation of pneumatic valves with the feedback control system. Simultaneously, the images were captured by a high-speed camera (Phantom V310, vision research). Besides, with the cooling channel, a microheater, and a temperature sensor, the temperature was controlled and detected during the experiments.

2.2.5 *The choice of cooling agent*

To achieve active on-chip cooling, a cooling agent with a relatively high cooling capacity and low freezing point is necessary. Besides, a non-toxic coolant with low cost would be preferred. We also need to avoid the vaporization of coolant in the channel. Hence, we chose calcium chloride solution with ice as our cooling agent. The freezing point of 30% $CaCl_2$ solution is -52℃, which is low enough for the cooling requirement in most cases. The specific heat of 30% $CaCl_2$ solution is 2.7 kJ/(kg K) at -40 ℃, which meets most applications' needs.

2.2.6 *Evaluation of temperature control response and stability*

The temperature control response and stability were evaluated respectively while the 1x PBS, used to simulate cell suspension, was running through the fluidic layer. To evaluate the temperature control response with the settling time, the temperature was set to 4 ℃, 10℃, 16℃, 10℃, 4℃ and 2℃ in order. As for the assessment of stability, the target temperature was set to 4℃ for 120 sec while the temperature fluctuation during this period was recorded and analyzed.

2.3 RESULTS

2.3.1 *The results of multiphysics simulation*

As seen in Figure 2.4, the Multiphysics simulation results showed that using the identical channel dimensions with properly defined boundary conditions, the fluid temperature at the intersection region can be cooled down to as low as 1℃, which is low enough as a cold source to achieve different target temperature for most cell analysis. With on-chip heating, local temperature sensing, and feedback control for the temperature manipulation, the fluid temperature at the target intersection area can be stabilized for a long time, with a wide range of temperature control capability from 2 ℃ to 37 ℃. When a dynamic temperature changing process is needed, a cooling/heating procedure with a specific cooling/heating rate can also be achieved.

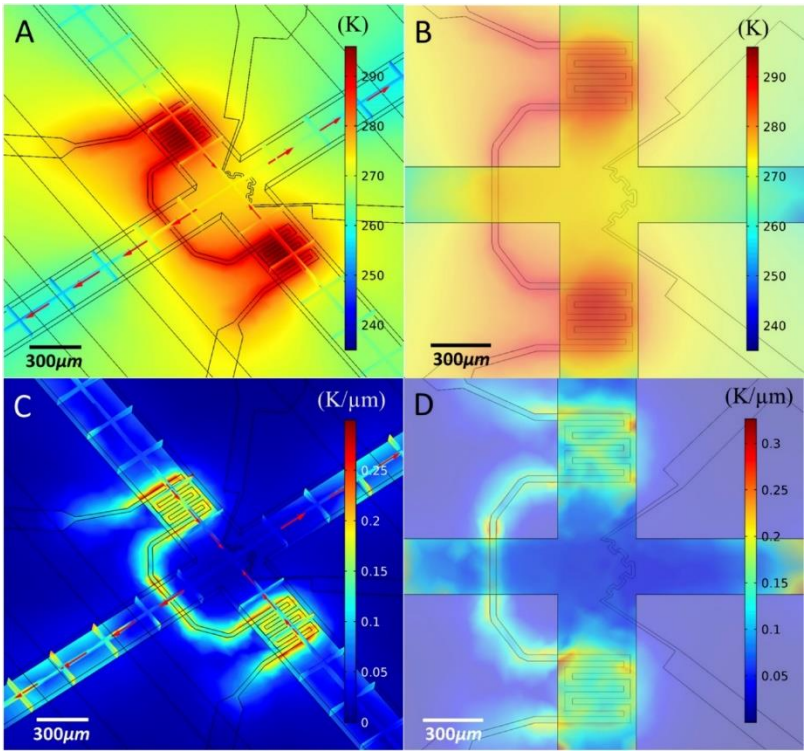

Figure 2.4. Numerical simulation of on-chip spatial temperature profile: (A) spatial temperature distribution; (B) planar temperature distribution; (C) spatial temperature gradient distribution; (D) planar temperature gradient distribution.

2.3.2 *Spatial and planar temperature and temperature gradient*

Figure 2.4 shows the simulation results of temperature and temperature gradients when the boundary conditions are set as described above and the target temperature at the intersection region is set as 1℃. Figures 2.4A and C demonstrate the spatial temperature distribution and spatial temperature gradient distribution, respectively. Figures 2.4B and D show the planar temperature distribution and planar temperature gradient distribution, respectively. The results indicate that the temperature in the trapping region is around 1℃, with a temperature gradient of less than $0.1℃/\mu m$.

2.3.3 *Temperature/temperature gradient along the center vertical line of the trapping region in the fluidic layer*

In Figure 2.5, the simulation results showed that the temperature varied from 2.2 ℃ to 0.8 ℃, from the bottom to the top of the fluidic layer. The temperature in the trapping region is around 1℃, with a temperature gradient less than $0.024\ ℃/\mu m$, which means the temperature nonuniformity would be only 0.24 ℃ for a region of $10\mu m$. Therefore, we can assume that temperature is uniform around a cell with a diameter of $10\mu m$.

2.3.4 *Convective heat transfer coefficient at various flow rates of cooling agent*

The simulation results of the Nusselt number with corresponding convective heat transfer coefficients at various cooling agent flow rates are listed in Table 2.3. The table shows that the convective heat transfer coefficient can be as high as 4039 $\frac{W}{m^2K}$ when the flow velocity of the cooling agent equals 0.05 m/s.

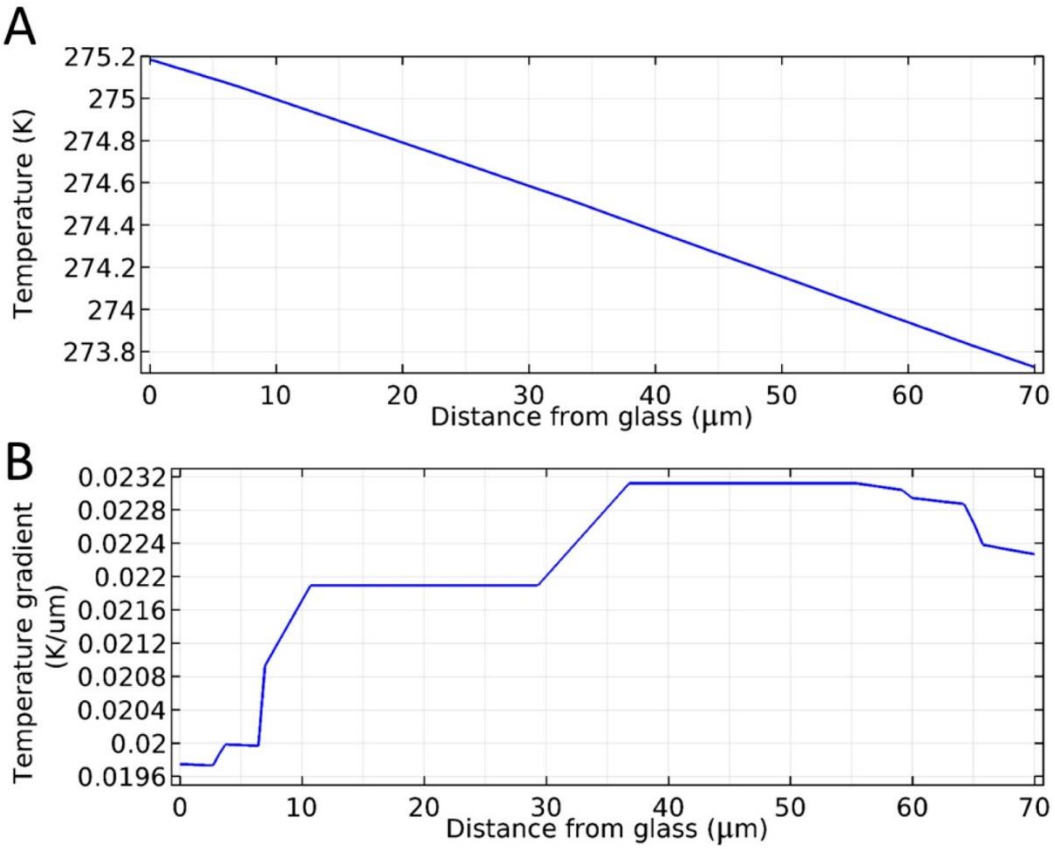

Figure 2.5. Numerical simulation of temperature profile along the trapping region's centerline: (A) temperature variation; (B) temperature gradient variation.

Table 2.3: Convective coefficient at various cooling agent flow rates

Flow velocity V $[m \cdot s^{-1}]$	Reynolds number Re	Prandtl number Pr	Nusselt number Nu	Heat transfer coefficient h $[Wm^{-2}K^{-1}]$
0.01	0.22	139.1	1.628	1806
0.02	0.45	139.1	2.303	2554
0.03	0.67	139.1	2.820	3128
0.04	0.90	139.1	3.256	3612
0.05	1.12	139.1	3.641	4039

2.3.5 *Experiment results of temperature control response and stability*

The experiment results of temperature control response and stability are shown in Figure 2.6. Figure 2.6A presents the actual temperature response to the target temperature change when 4 ℃, 10 ℃, 16 ℃, 10 ℃, 4 ℃, and then 2 ℃ were set as the target temperatures consecutively. It

shows that the temperature of the medium can reach the target temperature in 10 sec. Figure 2.6B shows the temperature stability when keeping 4 ℃ as the set temperature. During the data recording period (120 sec), the temperature reading was very stable, and the fluctuation was within 0.30 ℃.

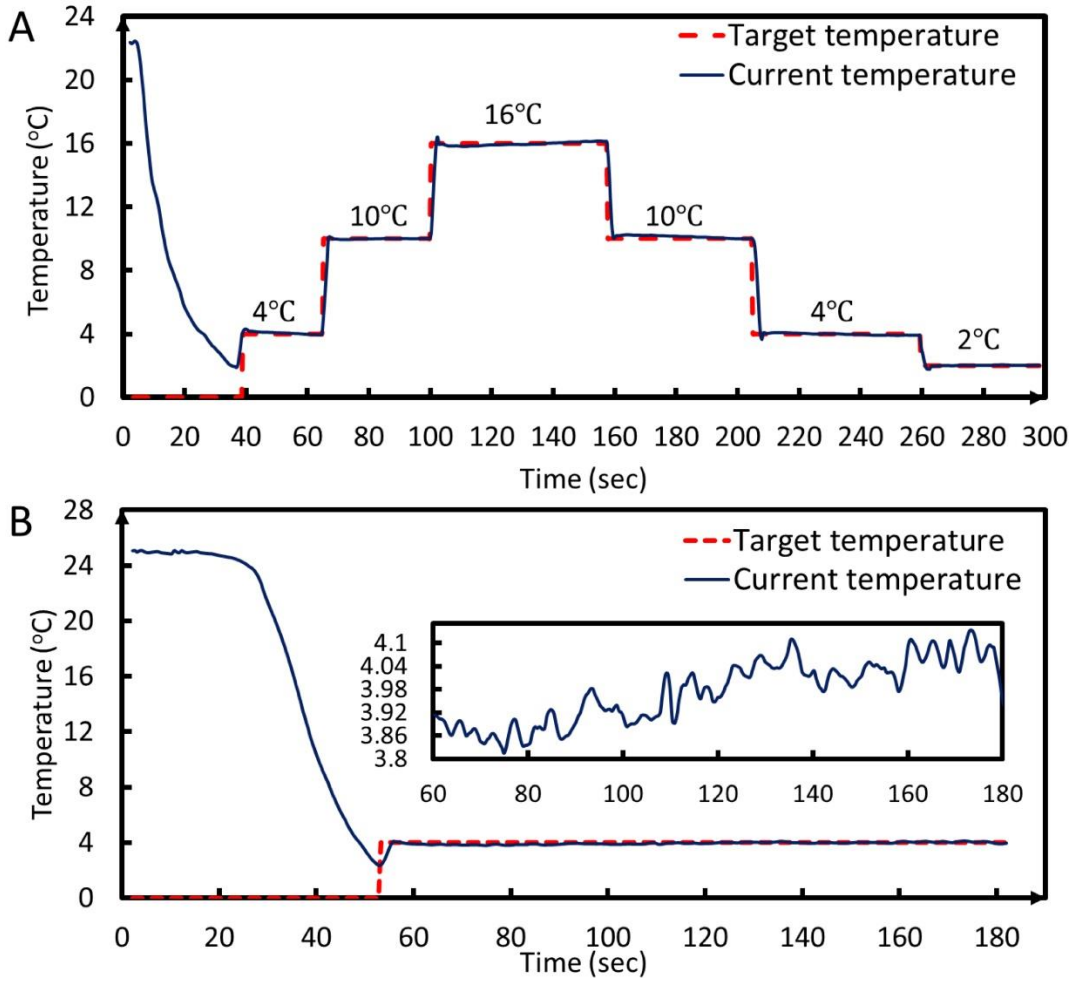

Figure 2.6. Temperature control response and stability: (A) actual temperature response to the target temperature change when 4 ℃, 10 ℃, 16 ℃, 10 ℃, 4 ℃, and then 2 ℃ were set as the target temperatures. (B) temperature stability when keeping 4 ℃ as the set temperature.

2.4 DISCUSSION

Currently, the available methods for determining cell membrane permeability to interested CPA solutions between the freezing point and room temperature are not very satisfactory. Recent developments of micro-fabrication and soft-lithography process provide a unique opportunity for the miniaturized device that integrates on-chip cooling/warming mechanism, localized temperature monitoring, and easy access for cell observation behaviors.

In terms of active cooling design, previous studies often employed an off-chip cooling mechanism without local temperature sensing and feedback control[26-28] or with an on-chip active cooling using materials that are not friendly for optical observation[32]. On the other hand, some previous studies paid more attention to producing extremely high cooling/heating rates instead of providing a well-defined steady thermal region for cell behavior observation[32-33]. To generate a system with such an active cooling mechanism and easy access to observation of cells, the heat transfer analysis is essential for the device's design, mainly based on PDMS in microfluidics. Besides selecting the cooling agent, the cooling channel geometry will also significantly affect the device's cooling performance. The heating elements pattern should be appropriately designed to provide a quick heating response and uniform temperature distribution in the target region for cell analysis. The interaction between the cooling and heating components is the critical issue that can achieve the actual temperature control with desired features, such as quick response, stability, precision, and uniformity. With an in-detail analysis of the heat transfer model of on-chip active cooling/heating microfluidics, the design is highly applicable for other applications with proper modifications.

A thermal control analysis was conducted for the microfluidic device with both on-chip active cooling and heating components in this work. The device consisted of three layers: a thin heating

layer with a gold wire as the boundary heat source, a fluid sample layer, and a cooling layer with a contiguously perfused cooling agent perfusing as the boundary heat sink. Heat transfer in the fluid was applied to the fluid sample layer. Heat transfer in solid was applied to the glass slide. Joule heating by the gold wire heater as in the thin layer worked as a boundary condition. Since the temperature difference in the vertical direction was much larger than that in the horizon direction, only the heat transfer in the vertical direction was considered in our case. Forced convection parallel planes model was applied to the coolant layer, where the bottom surface acted as the heat sink boundary condition for the fluid sample layer.

As shown in the simulation results, the total temperature difference of the cell solution layer from the bottom to the top was less than 1.4 ℃. For a cell with a diameter of 10 μm, the temperature difference in the region around the cell is only 0.25 ℃, which indicated the assumption that the whole cell stays at the same temperature. According to the simulation result, there was a 1 ℃ difference between recorded temperature and the real-time temperature due to the sensor detecting the temperature from the bottom to revise that in the final results.

With both the on-chip active cooling and heating under the proposed conditions, the reported device can achieve a temperature in the target center region ranging from 2 ℃ to 37 ℃. Considering that high temperature may cause injury to cells, we applied a conservative controller setting to avoid significant temperature overshoot. Even though the rise time (the time required for the response to rising from 10% to 90% of its final value) was within 5 sec and the setting time (the time required for the response to reach and stay within 5% of the final value) was within 10 sec, with variation within ± 0.2℃. The temperature could be stable at the desired temperature for more than 2 min with tiny fluctuation. Our system could change local temperature precisely and rapidly with all data and figures recorded.

The integrated microfluidic platform offers a new method for observing cell osmotic behavior under robust temperature control. As it provides a truthful cellular morphology image recording without the interference from the physical barrier and precise local temperature reading, the reported platform improves the precision of intrinsic cell cryobiological property measurement, hence assists cell cryopreservation, including the selection of optimal CPA, the optimization of CPA addition and removal, and the prediction of the optimal cooling rate for biological materials. It is also a valuable tool for studying and analyzing temperature-dependent cell properties that require reliable cell confinement techniques with the ability to manipulate the extracellular environment, such as advanced cell therapy and drug test. If there are potential chemistry experiments that require higher temperatures, our device can also be modified by similar mechanisms.

2.5 CONCLUSION

Through simulation analysis, we developed an integrated microfluidic platform with on-chip active cooling/heating components and automatic feedback control, which achieved the capability of longtime, stable, precise, and wide-range temperature control of the sample fluid layer. To investigate the on-chip temperature control performance, the reported platform was set to various target temperatures (2℃, 4℃, 10℃, and 16℃, consecutively). The experimental data demonstrated it is a reliable device to provide a platform with temperature control. Combining the control of the fluid flow in the channel, the reported platform achieves the following features: (1) single-cell trapping with extracellular medium change; (2) embedded patterned gold wire and the cooling layer filled with coolant acting as active heating and cooling components; (3) embedded patterned gold wire acting as the local temperature sensor as well.

This device can be used for many applications. For example, in cryobiology, it can be used to study the cell membrane's temperature-dependent phenomena, such as the membrane permeabilities to water and cryoprotectants, which are the essential factors for optimizing the cryopreservation approach.

In conclusion, our platform offers a delicate method for many fundamental and applied research providing a truly chemostatic environment, allowing for continuous solution switching, and achieving precise local temperature control.

Chapter 3. DETERMINATION OF THE MEMBRANE TRANSPORT PROPERTIES OF JURKAT CELLS WITH A MICROFLUIDIC DEVICE

3.1 INTRODUCTION

Solution injury and ice injury are both fatal to cells during cryopreservation, and they are firmly related to transmembrane water transportation[18]. The study on transmembrane mass transfer properties of the cell membrane will help researchers optimize the cryopreservation protocols to achieve the best cell viability. The most important properties to be determined are cell membrane permeability coefficient to water (hydraulic conductivity; L_p) and cell membrane permeability coefficient to CPAs (Ps).

Researchers found evidence that mass transfer properties of the biological membrane could be influenced and regulated by many factors, such as cell age[46], attractive optical potential[47], the specificity of membrane proteins [48], and the shape of aquaporins on the cell membrane [49]. Several devices have been developed to quantify L_p and P_s for different cells and were thoroughly reviewed by McGrath [50] and Zhao [16]. The most commonly used technique is using a microfluidic channel to observe the single-cell osmotic volume change under a microscope. Using data processing and a mathematical model for the transmembrane material transport, the related cell membrane properties could be obtained by parameter fitting.

Several devices have been designed to stably capture and observe one or a few cells at specific locations, utilizing multiple strategies. These cell trapping devices can generally be categorized into two types: contact and non-contact. Contact type includes methods using a micropipette, perfusion chamber, and holding block. Non-contact type includes acoustic tweezers, magnetic field, electric field, and flow field[34]. Gao[51] developed a micro-perfusion system using a

micropipette to hold a mouse oocyte by applying slight negative pressure on its zona pellucida. The mouse oocyte could directly be perfused into a solution of interest using another micropipette. This method could immediately switch the extracellular solution, but it could only be applied to limited types of cells. McGrath's group[52] developed a micro-diffusion system consisting of a solution flow channel, a sample chamber, and a porous membrane layer between the channel and the chamber. Cells could be stabilized in the chamber under the hydraulic pressure difference across the membrane. However, the porous membrane can get damaged during the fabrication of such sandwich structures, and the concentration of extracellular solution could not be changed instantaneously. Tseng[28] developed a device by bonding a PDMS layer (Polydimethylsiloxane) with a microfluidic channel onto a glass slide. The upper surface of the glass slide is treated by poly-D-lysine hydrobromide so that cells could adhere to it and then be observed and recorded. The disadvantage of this method is the requirement of a rapid flow rate.

Guo [53] developed a 3D acoustic tweezer using surface acoustic wave generators to generate pressure nodes surrounding the experimental area and trap a single cell in a particular 3D space. This system could manipulate cells without physical contact; however, introducing a high-frequency sound wave (13MHz) and its heat could influence cells' state. Gossett[54] developed a high throughput automated microfluidic technology capable of probing single-cell deformability using inertial focusing at an intersection area to stretch cells in an extensional flow. In that system, cells were carried and measured while being surrounded by fluid. Later, Fang[27] developed a dynamic microfluidic control system using the stagnation point in a flow field to trap individual cells at a similar intersection area. This system could avoid cells basing on precise flow control and could switch extracellular solutions instantly. Although this design could give highly accurate

results, manufacturing the multilayer microfluidic chip and operating such a complex control system requires considerable cost and labor work.

Chalut[55] developed an optofluidic assay to confine single cells. Cells were squeezed into channels smaller than the average cell size under a pressure gradient. Images were taken while cells were entering, passing through, and exiting the channel for deformation analysis. Pagliara[56-57] developed a device to investigate the physiology of VBSN cells with multiple dead-end narrow lateral microchannels connected to the main microchamber. This device could perform drug treatment on the single-cell that filled in the lateral channel, but switching took a considerably long time. Yobas[58-59] and Di Carlo[60] reviewed and summarized cell separation methods and sorting in microfluidic systems. Weir, pillar, crossflow, and membrane are four designs that belong to the microfilter method. The weir filter involves an individual barrier obstructing the flow path to isolate white blood cells from red blood cells in given whole blood. Red blood cells can pass only through a narrow slit located on top of the barrier.

Chen[61], Di Carlo[62], and Heo[63] also developed several microfluidic devices separately using PDMS microfluidic chip with a block inside the channel to trap cells. With a slow and steady flow inside the microfluidic channel, cells can be held at the block. Taking advantage of laminar flow in a micro-scale, the trapped cells could be perfused into CPA solutions immediately and entirely by changing solutions from the channel's inlet. This type of design is easy to fabricate, operate, and could be applied to cells of different sizes by modifying the block and channel size.

Jurkat cell is an immortalized line of human acute lymphocyte leukemia cells widely used in the study of adoptive cell therapy-a novel treatment of several advanced forms of cancer. The ability to transport water and solutes across the cell membrane under different temperatures is an important factor for deciding the specific protocol for cryopreservation of Jurkat cell. This study

proposes a comprehensive process for determining the membrane transport properties of Jurkat cell and using a novel microfluidic controlled single-cell trapping system. The osmotic behavior of individual Jurkat cell to water and dimethyl sulfoxide (DMSO), a commonly used cryoprotective agent (CPA), under constant temperature was recorded under a microscope utilizing the modified microfluidic system. The Jurkat cell images under osmotic change were processed to obtain a relationship between cell volume change and time. The experimental results were fitted using a two-parameter transport numerical model to calculate the Jurkat cell membrane permeability to water and DMSO at room temperature (22 ℃). This model and the calculated parameters can help scientists optimize the cryopreservation protocol for any cell type with optimal cryoprotective agents and cooling rate for future experiments.

3.2 MATERIALS AND METHODS

3.2.1 *Source of cells*

Human acute lymphoblastic leukemia cells (Jurkat cells, Clone E6-1) used in the experiments were purchased from ATCC (American Type Culture Collection, Manassas, VA, USA). Cells were cultured in T25 flasks inside a 37℃ incubator with 5% carbon dioxide and proper humidity. A unit of the culture medium contains 450mL RPMI (the base medium, salts, buffer, sugars, etc., RPMI Medium 1640(1X), Life Technologies, Thermo Fisher Scientific Inc., Waltham, MA, USA), 50mL fetal bovine serum (FBS), 5mL Penicillin-streptomycin and 5mL L-glutamine.

3.2.2 *Preparation of cells*

On the day of the experiment, 2mL cell suspension was collected from the flask. After counting with a cell counter (Countess II FL, Thermo Fisher Scientific Inc., Waltham, MA, USA), the cell suspension was centrifuged at 500g for 5 min and then resuspended with the culture

medium to make a density of 1×10^6 /mL. The experiments were finished within 3 hours to ensure the activity and viability of Jurkat cells. The size, morphology, and viability of cells were also be evaluated by the cell counter.

3.2.3 *Design and fabrication of the microfluidic chip*

Our design uses a block on the top of the microfluidic channel to stop the cells and keep the fluid flowing underneath the block. This block lowered the height of the microchannel at the trapping area. The manufacturing of a PDMS microfluidic chip with a block structure in the microchannel requires a mold with the microstructure of different heights fabricated on a silicon wafer using multilevel soft lithography. The height of both the block and the channel can be modified according to the cell of interest. In our study, since the isosmotic diameter of Jurkat cell usually ranges from 13-20 μm, we chose 5 μm as the height of the microchannel under the trapping block and 20 μm as the height at other parts of the microchannel so that only one Jurkat cell would be trapped at the block vertically. Detailed fabrication steps of the mold and PDMS chip can be found in our previous work[61].

After peeling off the PDMS chip from the mold, a 1mm hole was punched at one end of the channel to serve as the outlet, and a 5mm hole was punched at the other end near the block to serve as the inlet for the fluid flow, see Figure 3.1. A shorter distance between the inlet, blocking area and outlet was chosen to reduce the flow resistance to trap the cells more efficiently. A larger inlet reduces the influence of residual fluids while switching solutions and reduces the pressure disturbance due to different liquid levels. The PDMS chip was irreversibly bonded to a glass slide after oxygen plasma treatment using a plasma cleaner (PDC-32G, Harrick Plasma, Ithaca, NY, USA) under 18 W and 60-90 Pa for 60 sec. The bonding performance of the chip could be enhanced by placing the bonded chip on a hot plate at 60 ℃ for 2 min. 1xPBS solution was added

into the channel immediately after the surface treatment. It modifies the surface from hydrophilic to hydrophobic quickly, and it could be much more challenging to fill the microchannel with liquid after that. Since PDMS itself is permeable to gas[64–66], the negative pressure inside the PDMS chip after plasma treatment also helps eliminate micro air bubbles inside the microchannel.

3.2.4 *Setup of the device and operation procedure*

The whole device consists of an inverted microscope ((Nikon, Eclipse Te2000-s, Chiyoda, Japan), a camera (Phantom V310, Vision Research, Wayne, NJ) with a resolution of 600 by 600 pixels, a PDMS-glass microfluidic cell trapping chip, a precisely controlled microsyringe pump (Cetoni GmbH, neMESYS, Korbussen, Germany). The control system is shown in Figure 3.1. The fluid containing the prepared cells was perfused into the inlet reservoir gently using a pipette and then be sucked into the microchannel under negative pressure provided by a syringe pump at the outlet. One end of the tubing was connected to the matching connector of the precisely controlled microsyringe pump, and the other end was pushed into the outlet hole of the microfluidic chip. The microscope was placed under the trapping area to record the cell volume change.

Since PDMS is an elastic material, the connection between the chip and tubing was well sealed. 20-30 µL of cell suspension (cells in 1xPBS) was put into the inlet reservoir with a pipette, and the syringe pump was set to provide a flow rate of 10-20µL/hr. The flow rate was then adjusted to 5-10 µL/hr after several cells were stopped and trapped at the blocking area. As shown in Figure 3.2, one Jurkat cell in the flow coming from the left side was stopped by the block in the microchannel while the fluid went through under the block. A small low flow rate was used to avoid deformation of cells during the experiments, as cells can be deformed and pushed under the block.

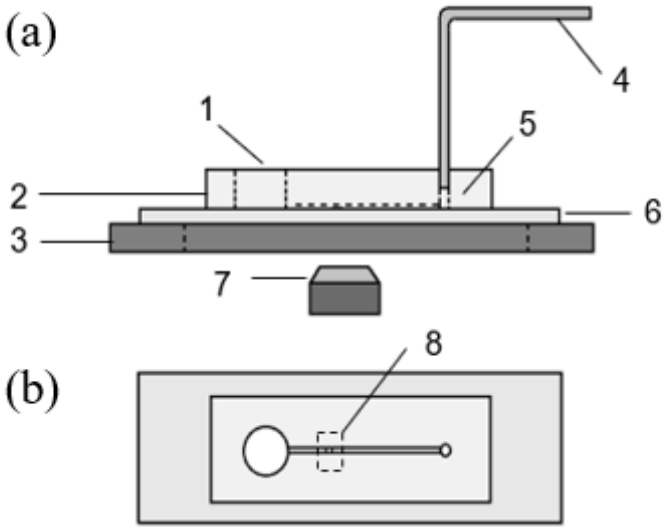

Figure 3.1. Sideview(a) and Top view(b) of the cell trapping system with a block structure: 1 medium solution reservoir(inlet); 2. PDMS microfluidic chip; 3. microscope holding stage; 4. tubings connected to syringe pump; 5. outlet; 6. substrate glass slide; 7. microscope lens and camera and 8. trapping area.

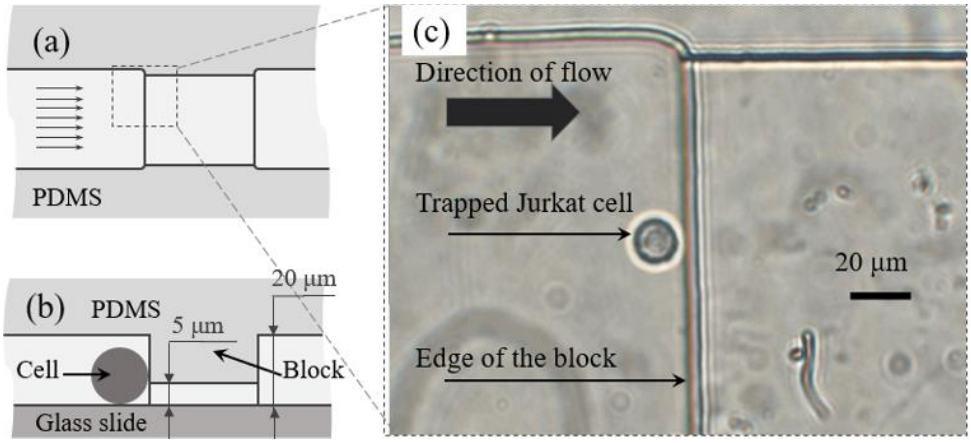

Figure 3.2. Schematic diagram showing top view(a) and side view(b) of trapping area in the microfluidic channel, parallel arrows indicate the flow direction. A Jurkat cell was trapped by the trapping block and recorded by microscope(c).

To switch the solution, the fluid residue was removed from the inlet reservoir gently and 20µL 10% DMSO(v/v) in 1X PBS solution or other isotonic medium was added into it using a pipette.

The camera started to record the images of trapped cells right before the addition of CPA solution. The entire osmotic volume changing process under this circumstance usually happens within few minutes. A frame rate of 5 images per second was optimal for our later parameter fitting work.

3.2.5 *Image analysis and data processing*

In the circumstance of penetrating CPA addition (e.g., DMSO), the water loss from the cytoplasm is usually faster than CPA penetration into cells under chemical potential gradients, which depends on cell membrane property as well. As a result, the cell would appear to be shrinking at first and then swelling as the intercellular environment reached equilibrium with the extracellular environment. In our study, this process was recorded by a camera, as shown in Figure 4.3.

Isolated cells in a better spherical shape on the raw images were cropped out to isolate single cells from background interference. The cropped images were then converted from color to 8-bit grayscale images. Using MATLAB, a gray intensity threshold was chosen where the images were divided at the precise edge of cells based on the gray intensity of pixels. The software could automatically divide and transform the images into small black and white square pixels referring to the threshold so that the cell's image would be distinguished from the background. The number of pixels that belong to the cell part on the processed image was counted. A mathematical relationship was then built to transfer that number of pixels into actual cell volume(V) and cell surface area(A). Utilizing the same relationship, cell volume change while extracellular environment switching from isotonic solution into 10% (v/v) DMSO in 1X PBS solution under room temperature could be obtained.

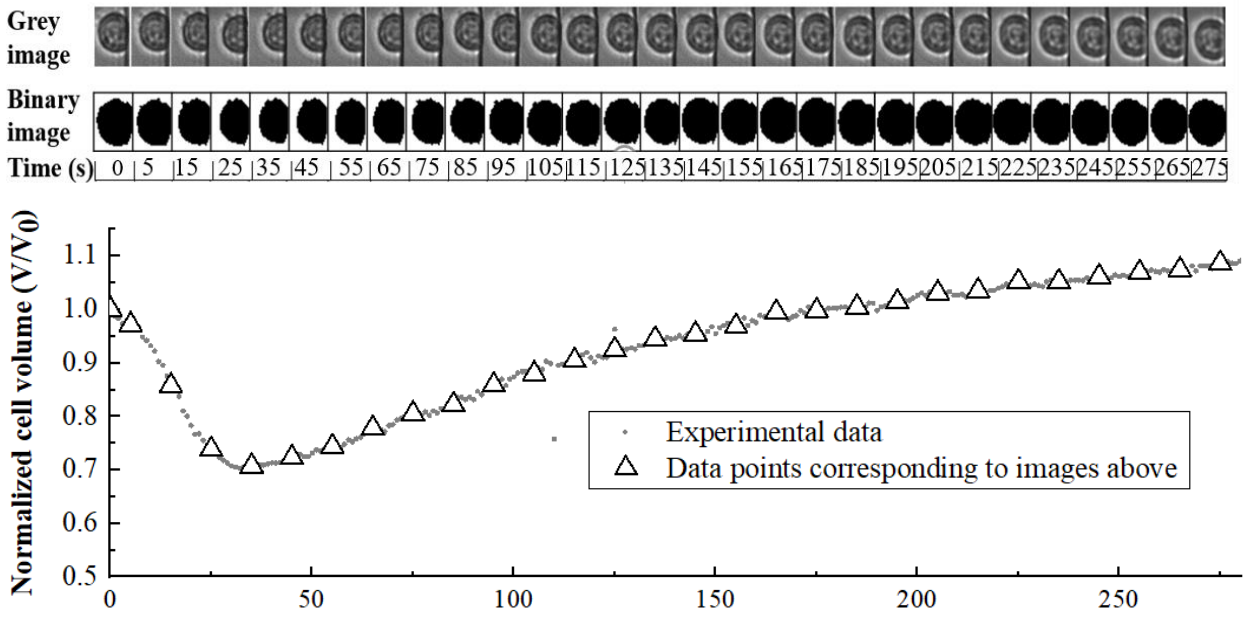

Figure 3.3. Grayscale images, binary images, and quantified cell volume values of single Jurkat cell volume change after environment changed from isotonic solution to 10%(v/v) DMSO in 1X PBS

3.2.6 *Validation of replacement time between different media*

Although the instantaneous step change of extracellular concentration has been claimed/assumed [15,18,47], the solution switch still takes some time. A coupled multi-physical model was built using COMSOL Multiphysics (COMSOL Inc., Palo Alto, CA, USA) to study the solution switch process in the microchannel. Time-dependent osmolarity distributions in the microchannel were simulated and visualized [48].

Peclet number (Pe) was also used to interpret the phenomenon during the solution switch. It is defined as the ratio of the rate of advection of a physical quantity by the flow to the diffusion of the same quantity driven by an appropriate gradient. The Peclet number in our platform is calculated as:

$$Pe = \frac{UL}{D} \tag{3.6}$$

where U represents local linear flow velocity, L is the characteristic length, and D is the mass diffusion coefficient. The Pe during the experiments was around 20, which meant the diffusion at the boundary between two consecutive solutions is negligible. In other words, we can assume that the cell was immediately switched from isotonic solution to hypertonic solution (10% DMSO in our study).

3.2.7 *Mathematical model of cell volume change to CPA addition*

The cell volume change can be expressed by the mass flux across the cell membrane. For the circumstances with only non-permeable solutes being added into the solution, the water flux across the cell membrane that is related to chemical potential gradient can be expressed as [1]:

$$\frac{dV_c(t)}{dt} = L_p \cdot A \cdot (C_n^i - C_n^e) \cdot R \cdot T \tag{3.7}$$

where $V_c(t)$ is cell volume (um^3) at time t (min), L_p is the cell membrane permeability to water (μm/min/atm), A is the average surface area of a single cell (um^2), C_n^i is the intracellular osmolarity (Osmol/L), C_n^e is the extracellular osmolarity (Osmol/L), R is the universal gas constant (0.08207 atm·L/(mol·K)), T is the absolute temperature (K, in our study T, equals to 22 ℃, the room temperature). While the extracellular solution is switched from isotonic to hypertonic, loss of cytoplasmatic water will lead to cell shrinkage until intracellular osmolarity reaches an equilibrium with the extracellular osmolarity. Since the only reason for cell volume change is the loss of water, C_n^i can be expressed as:

$$C_n^i = C_0 \cdot (\frac{V_0 - V_b}{V - V_b}) \tag{3.8}$$

where C_0 is isotonic osmolarity (Osmol/L for blood and body fluid is approximately 0.3 Osmol/L, which is also our initial intracellular osmolarity), V_0 is the isotonic cell volume (um^3), V_b is the osmotically inactive cell volume (um^3) that could be determined by Boyle van't Hoff plot.

Although a few previous researchers considered the interaction between solvent and solute into the numerical model of transmembrane mass transfer while they both transport through a common channel specifically, discoveries in molecular biology indicate that, in natural biological membranes, cotransport of water and penetrating solute is often unlikely or negligible. As a result, for the numerical model of CPA addition with both penetrating and non-penetrating solutes, cell volume change can be expressed as:

$$\frac{dV_c(t)}{dt} = \frac{dV_s(t)}{dt} + L_p \cdot A \cdot (C^i - C^e) \cdot R \cdot T \tag{3.9}$$

where V_C and V_S are cell volume and intracellular CPA volume at time t, respectively. C^i, C^e are intra- and extracellular osmolarity, including CPA and saline, A is cell surface area, R is gas constant, and T is the temperature in kelvin. L_p is the cell membrane permeability coefficient to water.

The CPA flux can be calculated by following two equations:

$$\frac{dM_s(t)}{dt} = P_s \cdot A \cdot (C_s^e - C_s^i) \tag{3.10}$$

$$M_s(t) = V_S(t)/v_s \tag{3.11}$$

where P_s is the cell membrane permeability coefficient to CPA, C_s^e, C_s^i are extra- and intracellular CPA osmolarity. $M_s(t)$ is the mole of intracellular CPA at time t. v_s is the partial volume of CPA (mole/L)

L_p and P_s can be determined by parameter fitting the differential Equations (3.9) and (3.10) with data from experiments using software Mathematica (Wolfram Research, Champaign, IL, USA).

3.3 RESULTS

3.3.1 *Obtaining osmotic inactive cell volume (V_b) of Jurkat cell*

Osmotic inactive cell volume of Jurkat cell can be determined by measuring the average Jurkat cell volume in several saline solutions with different osmolarity and then doing the Boyle van't Hoff plot with the cell volume and the reciprocal of the osmolality of the solution. Cell morphology in several hypotonic and hypertonic PBS solutions was captured using a microscope to obtain the cell volume. Each image taken has 5-9 cells on it. The raw images were processed, and the average cross-section area of cells was given utilizing Image J (Wayne Rasband, National Institute of Health, USA). Average cell diameters could then be obtained with a simple calculation. PBS solutions in different osmolality could be obtained by mixing high concentration PBS solution with different amounts of DI water. The cell suspension was added into the PBS solutions and the mixture was held for 5 min before measuring to reach osmotic equilibrium. The osmolality of the mixture was tested using a vapor pressure osmometer (MODEL 5520, WESCOR Vapro, Logan, UT, USA).

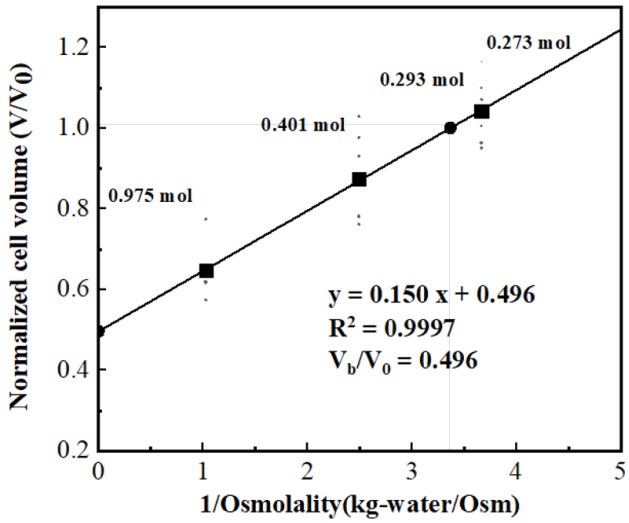

Figure 3.4. Measurement of osmotic inactive cell volume (Vb).

This study measured the cell equilibrium volume under 173, 401, and 975 mOsmol/kg environments, with data collected from at least 6 sets. According to Boyle van't Hoff equation, a linear line can be obtained by linear fitting cell volume that normalized to isotonic cell volume to the reciprocal of corresponding osmolality, and the intercept of that fitting line at y-axis equals to the ratio of the osmotically inactive volume (V_b) to isotonic cell volume (V_0). As the Boyle van't Hoff plot shown in Figure 3.4, for Jurkat cell, V_b/ V_0 equals 0.496 in our study.

3.3.2 *Solution switching in the microchannel*

In our study, the solution in the microchannel was switched from cell suspension (297 mmol/L) to 10% DMSO (v/v) in 1X PBS solution (1823 mmol/L). As indicated in the methods section, the osmolarity distribution inside the microchannel at 3, 4, 5, and 6 sec after changing the solution at the inlet of the device was simulated using COMSOL, as shown in Figure 3.5. The trapping block is located at the middle line of the microchannel in Figure 3.5.

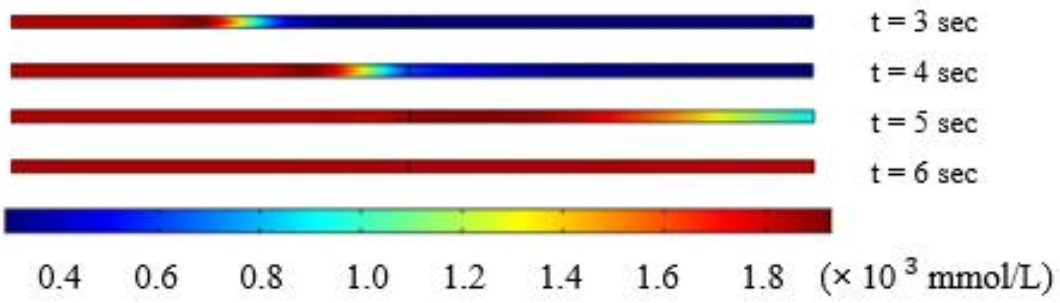

Figure 3.5. Osmolarity change inside the microchannel.

As a result of physical phenomena in the micro-scale, CPA diffusion developed rather slowly during the switching process. Solution switching at the trapping block from isotonic to hypertonic environment was completed within 1.5 sec, as shown in Figure 3.6. The results indicate that the extracellular environment changed in a very short time, and we could assume that solution was switching completed instantly.

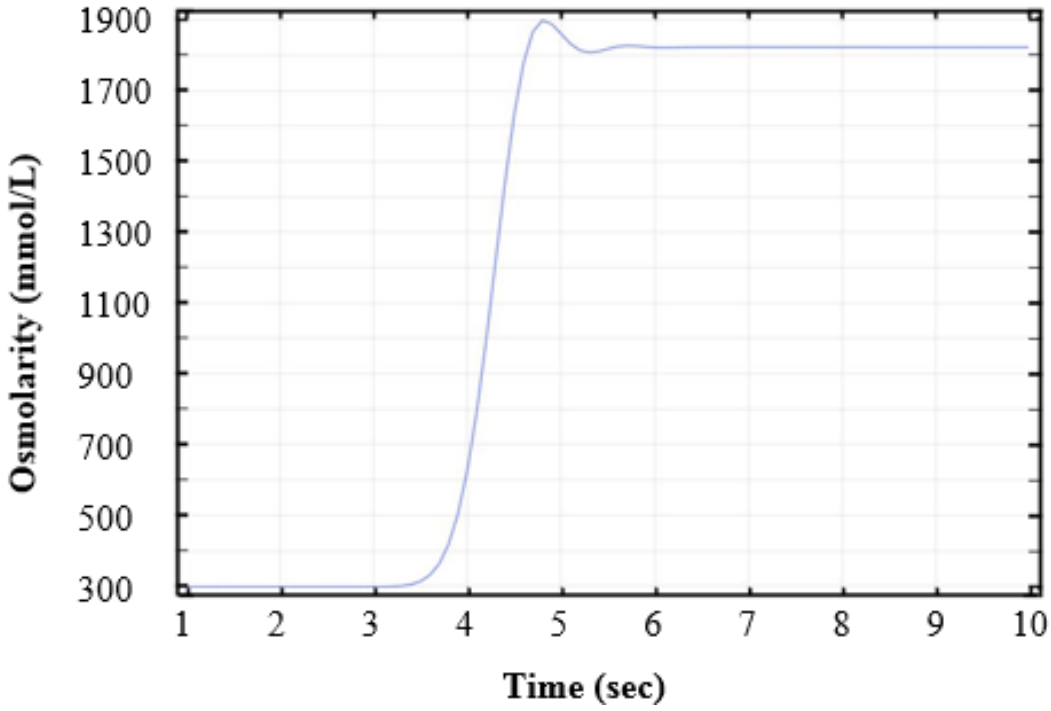

Figure 3.6. Time-dependent osmolarity change at the block.

3.3.3 *Cell membrane permeability coefficient to water (L_p) and CPAs (P_s) by curve-fitting*

To find the cell membrane properties L_p and P_s, the data sets of cell volume change to time were used as V_c and t respectively to do a parameter fitting in coupled differential equation (4) and equation (5). As shown in Figure 3.7, both water loss and CPA transport happened at a rather fast speed during the initial part of the change. The Jurkat cell membrane permeability coefficients to water and DMSO were found by our method to be 0.148±0.051 μm/min/atm and 0.00034±0.000014 cm/min (n=8).

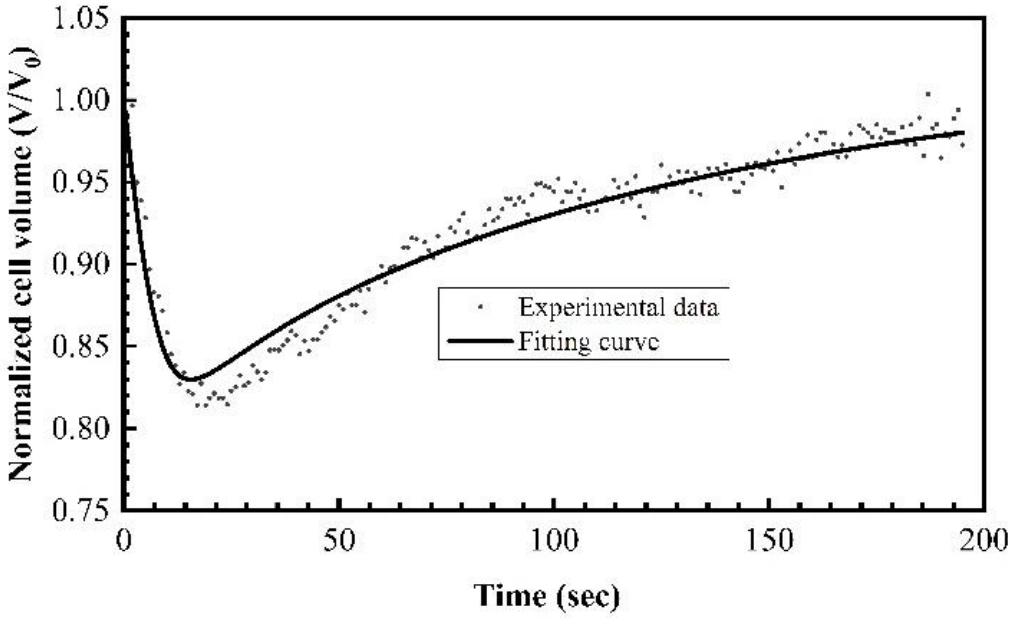

Figure 3.7. Parameter fitting of Jurkat cell volume change during the switch from 1xPBS to 10% DMSO (v/v) in 1X PBS at room temperature.

3.4 DISCUSSION

Jurkat cell is an immortalized line of human acute lymphocyte leukemia cells that have been used in many studies, such as T-cell activation and T-cell receptor signaling. Those studies have great importance to virus and cancer treatment. Several Jurkat cell lines are available from commercial companies nowadays. However, to keep the consistency of cells for research purposes and save the cost of materials, the cryopreservation of Jurkat cells is still significant. During the optimization of the cryopreservation protocols, including the choice of CPA solution and optimum cooling rate, the measurement of its cell membrane permeability to water and CPA, such as DMSO, is one of the most critical procedures. Researchers could find out how the cell volume and intracellular osmolarity would change during different situations using numerical simulation with

the help of those parameters. A proper choice of both CPA and cryopreservation protocol would protect cells from osmotic injury during CPA addition/removal and leave minimum yet necessary water inside the cell to avoid lethal intracellular ice crystallization. Therefore, to measure the L_p and P_s of Jurkat cell, a simple, reliable microfluidic platform was developed by our group. With our device, suspended Jurkat cell would flow into the microchannel under negative pressure, be stopped by a trapping block in the channel, perfused by the CPA solution, and undergo volume change recorded by a camera.

In our design, the solution switch's instantaneity at the cell trapping part is extremely important for the following data analysis and the accuracy of calculated cell membrane properties. To verify this assumption, the transport process of the CPA solution in the microfluidic channel was simulated with COMSOL. Based on the experimental settings, CPA diffusion is relatively tiny compared to the fluid flow convection. The unwanted osmolarity gradient of CPA at the cell-trapping block would only exist for a short time. Based on the simulation results, the time is around 1.5 seconds or less for the replacement of isotonic solution by the target hypertonic solution, comparable to the previous study[61]. The result was also qualitatively proved by the relatively high value of Pe number for the channel flow.

The parameter fitting result of L_p in our study is 0.14 μm/min/atm and Ps (to DMSO) is 0.00034 cm/min. For reference, former results have shown L_p as 0.38 μm/min/atm and P_s as 0.00049 cm/min for rat basophilic leukemia cell[61], L_p as 0.18 μm/min/atm and P_s as 0.00046 cm/min for human granulocyte[67], and L_p as 0.295 μm/min/atm and P_s as 0.00098 cm/min for human vaginal mucosal macrophage[68]. A considerably convincing result was determined by parameter fitting process in this study compared with other results.

Combining the experimental setup and two-parameter transport model could be used as a standard investigating approach for other cell types. Using the microfluidic device, the cell membrane permeability to water and CPA were determined, which will assist cell cryopreservation, including selecting optimal CPA, the optimization of CPA addition and removal, and the prediction of the optimal cooling rate for the cells. For example, the current work shows that the measured Ps value to DMSO for Jurkat cells is relatively low compared to that for many other cells presented in previous papers. From this study, DMSO, a widely used CPA for cryopreservation, may not be the optimal choice of CPA for Jurkat cells. Further research to investigate other CPAs for Jurkat cells will be conducted.

3.5 CONCLUSIONS

Through simulation and image processing analysis, the cell membrane permeability of Jurkat cells to water and CPA (DMSO) was determined with our microfluidic device. The measured properties would be used to generate optimal cryopreservation protocols for Jurkat cells. Potential research can also be inspired by the results, such as exploring optimal CPAs (high Permeability and low toxicity) and optimizing the cooling process for Jurkat cells.

Chapter 4. DEVELOPMENT OF A MULTIFUNCTIONAL CELL PROCESSING SYSTEM AND AN AUTO-GENERATED PROTOCOL MINIMIZING OSMOTIC INJURY

4.1 INTRODUCTION

The traditional CPA removal method uses a centrifuge to separate extracellular solution and cells by relative centrifugal force (RCF), replacing supernatant with desired CPA-free media for future use. However, this method can result in cell clumping and loss, stem cell activation, and contamination risk [69]. Some non-centrifuge methods have been applied in CPA addition and removal in the last twenty years. Arnaud first proposed using a hollow fiber membrane to remove dimethyl sulfoxide(DMSO), the most common CPA, from platelet concentration[70]. Many theoretical and experimental investigations of removal CPA from cryopreserved blood with hollow fibers were performed and published by Dr. Ding[69–71]. The dilution-filtration method was then kept developed by Zhou, Qiao, and Liu[72–74] with a modified dilution method and removal protocol. To fulfill the demands from small-amount cell suspension, microfluidic technology was also employed to achieve CPA loading and unloading in micro size[75-76].

Previous pioneers made a significant contribution aiming to recover more valuable biological materials by different CPA removal methods. However, a universal system with a cell-type optimal removal protocol is still unavailable and desired. In our opinion, sterile processing, automatic procedures without too much human workload, and specific optimal protocols for certain cell types are indispensable design requirements of such kinds of devices.

In this work, a multifunctional cell processing system with functions of CPA removal and cell concentration in sterile was developed. The system is based on the dilution-filtration method and innovatively added hypertonic dilution option to minimizing osmotic injury. Theoretical discussion regarding cell membrane properties and hypertonic dilution approach was performed. An advanced algorithm to generate optimal CPA removal protocol was proposed. Cell-free CPA removal experiments and in-vitro cell concentration experiments were conducted.

4.2 THEORETICAL BACKGROUND

The experimental setup is shown in Figure 4.1. The system consists of three peristaltic pumps, three 3-way T-pattern valves, an oscillating shaker, a dialyzer, and the tubing connecting them. Peristaltic pumps provide driving force to make liquid circulate and move along the tubing. The dialyzer membrane, whose pore sizes are much smaller than human cells, keeps cells in the cell loop and prevents them from being removed by ultrafiltration. Valve 1 can be switched between hypertonic dilution solution and isotonic dilution solution for different modes. Valve 2 and 3 are used to recover cell solution left in the cell loop after CPA removal and cell concentration processes by letting dilution solution skip cell bag, flow into cell loop, and push the cell solution back to the cell bag through the right end. The control settings for each mode are shown in Table 4.4.

Table 4.4: Control settings for different working modes

Mode	P1	P2	P3	V2	V3	Oscillating shaker
CPA removal	On	On	On	Left-Right	Left-Right	On
Recycle	On	On	Off	Left-Top	Left-Bottom	Off
Concentration	Off	On	On	–	Left-Right	On

The assumptions have been made that: (1) The dilution solution and cell solution will mix well at once when dilution solution is pumped into cell bag; (2) Osmolarity in cell loop is regarded as uniform. During the CPA removal process, the extracellular osmolarity was analyzed first to set up a transient environment for cells. Facing changing extracellular osmolarity, cell volume changes were discussed considering water and CPA movements. The cell concentration process was simulated based on the total volume change of cell suspension. The simulation and figures are conducted with MATLAB(The Mathworks Inc.).

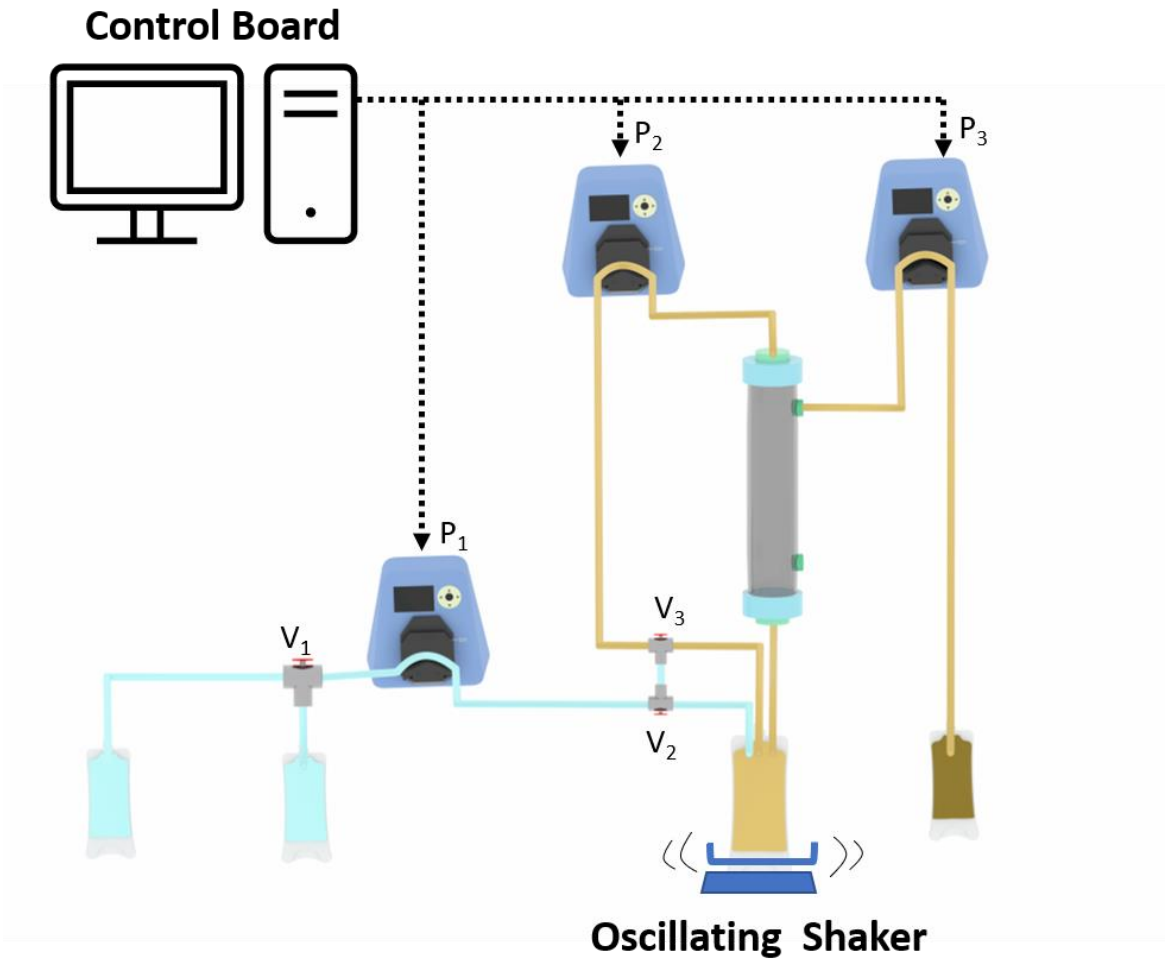

Figure 4.1. Diagram of the multifunctional cell processing system

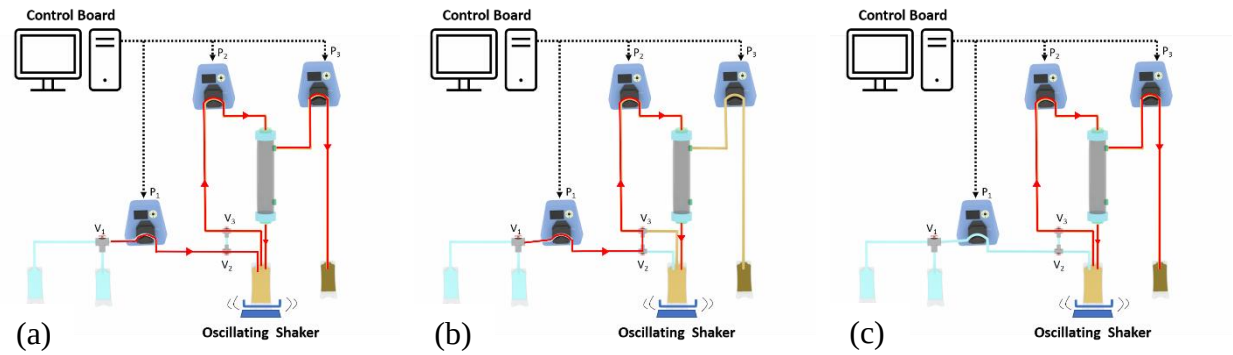

Figure 4.2. Flow directions of each mode: (a) CPA removal; (b) Cell recycle; (c) Concentration.

4.2.1 *Extracellular osmolarity*

The cytocrit (α) can be calculated with the size, volume, and concentration of cells. Such for Jurkat cells, the diameter is 11.5 μm and volume is 796.33 μm^3[77] with a concentration of 10^6 /mL. The cytocrit can be calculated as:

$$\alpha = 796.33\mu m^3 \times \frac{10^6}{mL} = 7.96e-4$$

which is less than 0.1%.

After determining the cytocrit (α) of experimental Jurkat cell suspension, the effects of intracellular water can be ignored during the extracellular osmolarity calculation. Thurs, extracellular osmolarity is governed by the following equations:

$$\frac{dV}{dt} = Q_d - Q_f \tag{4.12}$$

$$\frac{d(C^eV)}{dt} = C^dQ_d - C^eQ_f \tag{4.13}$$

Where V is the total volume of the cell suspension, Q_d and Q_f are flow rates of dilution and ultrafiltration separately, C^e represents the osmolarity of extracellular osmolarity and C^d represents osmolarity of dilution.

4.2.2 *Cell volume change over the time*

The cell volume change is dominated by water and CPA transportation across cell membrane during the CPA removal process, which can be calculated by two-parameter transport formalism[11] with obtained cell membrane properties and extracellular osmolarity profiles. Equations (3-9), (3-10), and (3.11) were employed to simulate cell volume excursion.

4.2.3 *Additional hypertonic dilution step during CPA removal*

During the CPA removal process, the cell volume is controlled by two factors: expansion caused by the inflow of water and shrink caused by the outflow of CPA. At the early stage, the inflow of water dominates the cell volume change since the incoming dilution solution generates a huge osmolarity, including both saline and CPA, drop. As the ultrafiltration gradually removes extracellular CPA, the continual decrease of extracellular CPA osmolarity forced the intracellular CPA to keep moving out, making the cell shrink back to the isotonic volume in the end. According to the above two-factor mechanism, the cell volume change during CPA removal is like a reversed U-shape. To minimize the solute injury during this process, the peak of this curve should be as low as possible, which is mainly dominated by the inflow of water at the early stage.

In this work, the method with an additional hypertonic dilution step is proposed. Instead of directly diluting with isotonic saline, the cell suspension with CPA is first diluted with hypertonic saline solution for a small amount of time and then switched to isotonic saline. This additional step can decrease osmolarity difference across the cell membrane at the first tens seconds, decreasing the inflow of water and lowering the “peak” of the cell volume curve. At the same time, the hypertonic saline solution does not include any more CPA. So that the performance of CPA removal is not affected, the osmolarity and dilution time of hypertonic saline solution can be modified for different cell types to achieve optimal performance.

4.2.4 *Cell concentration*

The standard pore size of hollow fiber is around 200 nm, which is much smaller than most human cells[78]. In this work, the diameter of Jurkat cells is mainly from 10 μm to 16 μm. So that the cells do not pass across hollow fiber membrane but stay in the cell loop during the concentration process. As the fluid of cell suspension is removed by ultrafiltration, the total cell suspension volume gradually decreases, and desired cell concentration will finally be reached. The following equations can express this process:

$$\frac{dV}{dt} = Q_f \tag{4.14}$$

$$n(t) = \frac{N}{V(t)} \tag{4.15}$$

where N is total cell numbers in the cell suspension and n(t) (mL^{-1}) is the cell concentration at time t.

4.3 METHODS

4.3.1 *Cell preparation*

Human acute lymphoblastic leukemia cells (Jurkat cells) used in this work were purchased from ATCC(American Type Culture Collection, Manassas, VA) and cultured in a 37℃ incubator with 5% carbon dioxide and proper humidity. 500 mL culture media consists of 440mL RPMI medium 1640(Life technologies), 50 mL fetal bovine serum (FBS), 5mL Penicillin-streptomycin, and 5 mL L-glutamine. Cells with a density of ~ 10^6/mL were used for experiments.

4.3.2 *CPA addition*

10% v/v DMSO in PBS is a standard CPA concentration in cryopreservation. To minimize osmotic injury to cells during the CPA addition, 20% DMSO solution is prepared first and then added to cell solution with 1:1 ratio dropwisely to achieve final concentration as 10% DMSO.

4.3.3 *Cell-free CPA Removal Experiment*

Three different groups were tested to compare their performances of CPA removal.

Group 1: 1*PBS was pumped into the loop from the tubing near the dialyzer's inlet with a speed of 20mL/min, not shown in Figure 4.1. To keep cell solution volume constant, the ultrafiltration rate was also set as 20mL/min.

Group 2: 1*PBS was pumped into the solution reservoir directly with a speed of 100 mL/min. The ultrafiltration rate was set as 100mL/min as well to keep the cell solution volume constant.

Group 3: The flow rates of addition and ultrafiltration were same as group 2. The additive solution was changing between hypertonic and isotonic saline solution.

Detailed information can be found in Table 4.5:

Table 4.5: Setup of Cell-free CPA Removal Experiments

Group	Group 1	Group 2	Group 3
Dilution/Filtration Rate	20mL/min	100mL/min	100mL/min
Total Volume	1110mL	1110mL	1113mL
Osmolality of Dilution Fluid	292	292	1153 (0-60s) 549(61-120s) 376(121-180s) 292(181s-)

4.3.4 *Cell concentration*

Prepared 50-mL cell solution with cell concentration of 4.4×10^5 was diluted with PBS to 250mL. The system, whose priming volume is 40 mL, was first primed with PBS for 5 min to

remove the air bubble, affecting concentration performance. Diluted cell solution then was circulated inside the system with ultrafiltration pump open. The solution sample was first collected at the beginning and then every 2 min for cell counting. Once the cell solution bag was almost empty, the artery tube was removed from the solution bag, and the ultrafiltration pump was turned off. 42mL cell solution was then recovered by cell pump, which pumped cell solution left in the tubing to the bag. As for the cell counting process, 10 μL cell suspension was mixed with 10 μL Trypan Blue solution (Sigma-Aldrich) and counted by Countess II FL Automated Cell Counter (Invitrogen).

4.4 RESULTS

4.4.1 *The removal performance of three approaches and validation of the CPA removal model*

As seen in Figure 4.3, extracellular osmolality profiles of three different CPA removal approaches are shown. The initial osmolalities of the three groups are 1859, 1715, 1650 mmol/kg, respectively. After 18-min experiments, the osmolality of group 1 dropped to 1462 mmol/L while these of the other two groups were 570 and 591 mmol/kg, respectively. Numerical simulation based on Equations (4.12), (4.13) has been conducted and plotted in Figure 4.3. Detailed data and comparison can be found in Table 4.6.

Table 4.6: Validation of CPA removal model under three different working conditions (Unit: mOsmol/kg)

Time(min)	Group 1			Group 2			Group 3		
	Exp.	Num.	Error (%)	Exp.	Num.	Error (%)	Exp.	Num.	Error (%)
0	1859	1859	0.00	1715	1715	0.00	1650	1650	0.00
2	1806	1804	0.11	1464	1481	1.16	1495	1517	1.47
4	1755	1750	0.28	1246	1283	2.97	1303	1320	1.30
6	1696	1698	0.12	1071	1118	4.39	1130	1149	1.68
8	1648	1648	0.00	954	981	2.83	987	1007	2.03
10	1603	1600	0.19	829	866	4.46	877	887	1.14
12	1558	1553	0.32	746	770	3.22	782	788	0.77
14	1514	1508	0.40	667	690	3.45	692	705	1.88
16	1497	1465	2.14	603	623	3.32	621	635	2.25
17	1462	1448	0.96	570	593	4.04	591	605	2.37

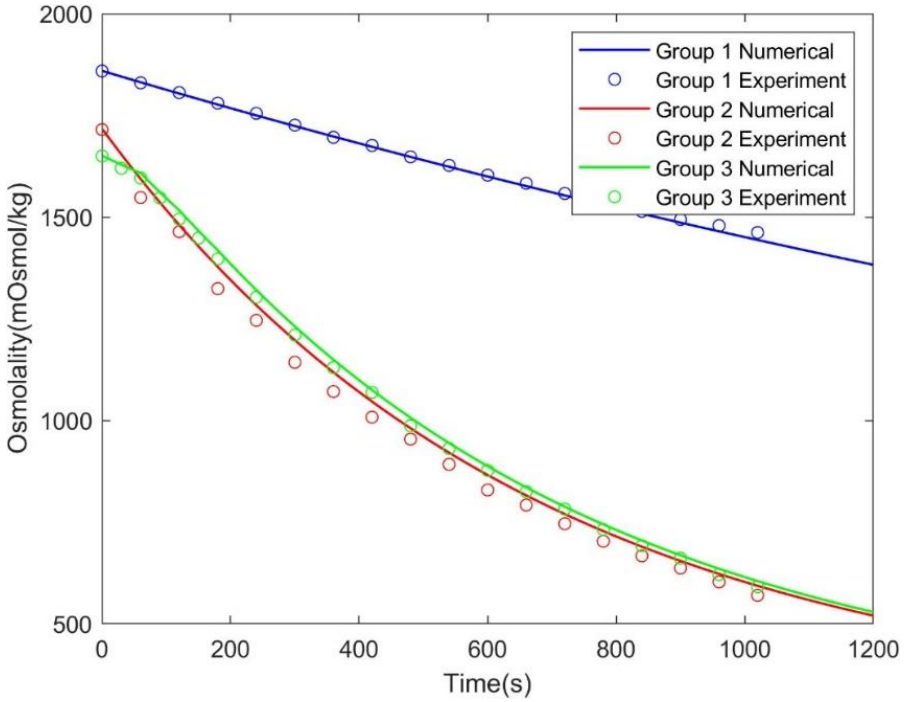

Figure 4.3. Simulation and experiment results of cell-free CPA removal experiments

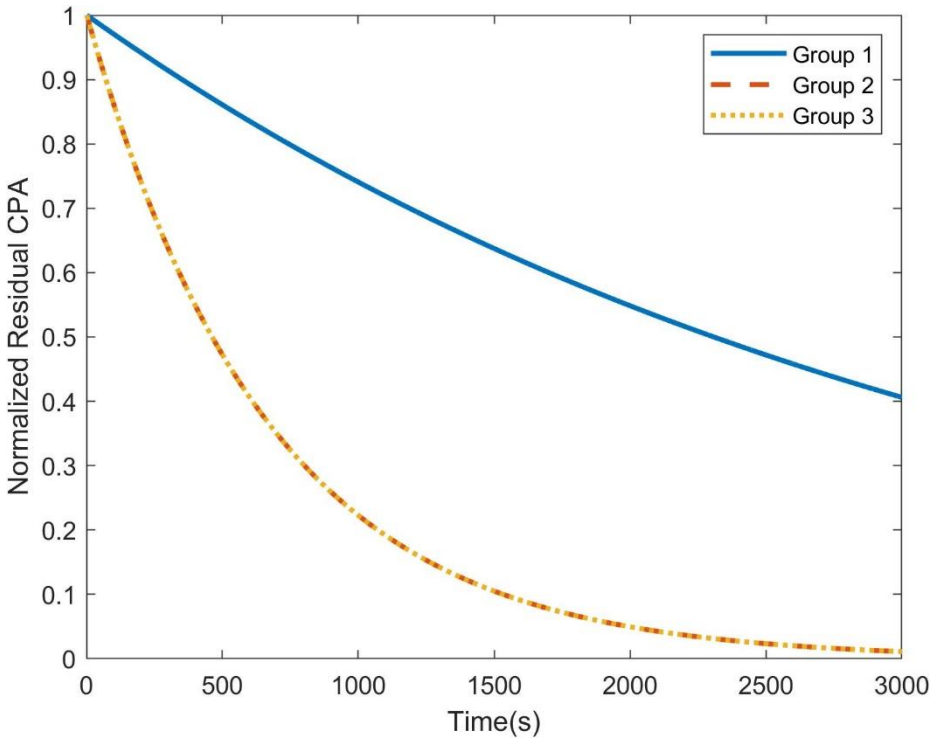

Figure 4.4. Normalized Residual CPA with different removal approaches

Figure 4.4 shows normalized residual CPA of different groups when initial osmolarity is set as 1800 mOsm/L. The curves of groups 2 and 3 are precisely the same since every parameter is the same regarding the CPA.

4.4.2 *Cell volume change of different cell types and different CPA removal approaches*

The numerical extracellular osmolality profiles had been validated in the previous subsection and then further used to calculate cell volume change during the CPA removal. Three types of human cells, Jurkat cells, vaginal T cells, and vaginal macrophage, were investigated for their cell volume reactions with different CPA removal approaches discussed in the section. Related cell properties and membrane permeabilities used during simulation can be found in Table 4.7. The initial condition was set as 10% DMSO (1800 mOsm/L). The hypertonic saline solution of group

3 had been modified to 500 mOsm/L for the first half minute. And then, the isotonic saline was used as a dilution solution starting from the 31st second.

As shown in Figures 4.5, 4.6, 4.7, normalized cell volumes, cell volume at time t divided by the initial cell volume, were calculated for each removal approach. For Jurkat cell, group 1 has the smallest maximal cell volume, 1.012, during the CPA removal process. Group 2 and 3 have relatively similar peak values, which are 1.048 and 1.035, respectively. For vaginal T cells, the maximal cell volumes for groups 2 and 3 are 1.022 and 1.009, respectively, while group 1 is 1.005. Vaginal macrophage got 1.004 for group 1 and 1.017 for group 2. The maximal cell volume of group 3 is 1.003, which is even smaller than group 1.

Table 4.7: Cell properties and membrane permeabilities of different cells when DMSO is present[68, 77, 79]

Cell types	Diameter(um)	V_b	L_p (um/min/atm)	P_s (xe-3 cm/min)
Jurkat Cells	11.5	49.6%	0.14	0.34
Vaginal T Cells	8.43	51.6%	0.089	0.47
Vaginal Macrophages	9.62	45.7%	0.234	0.99

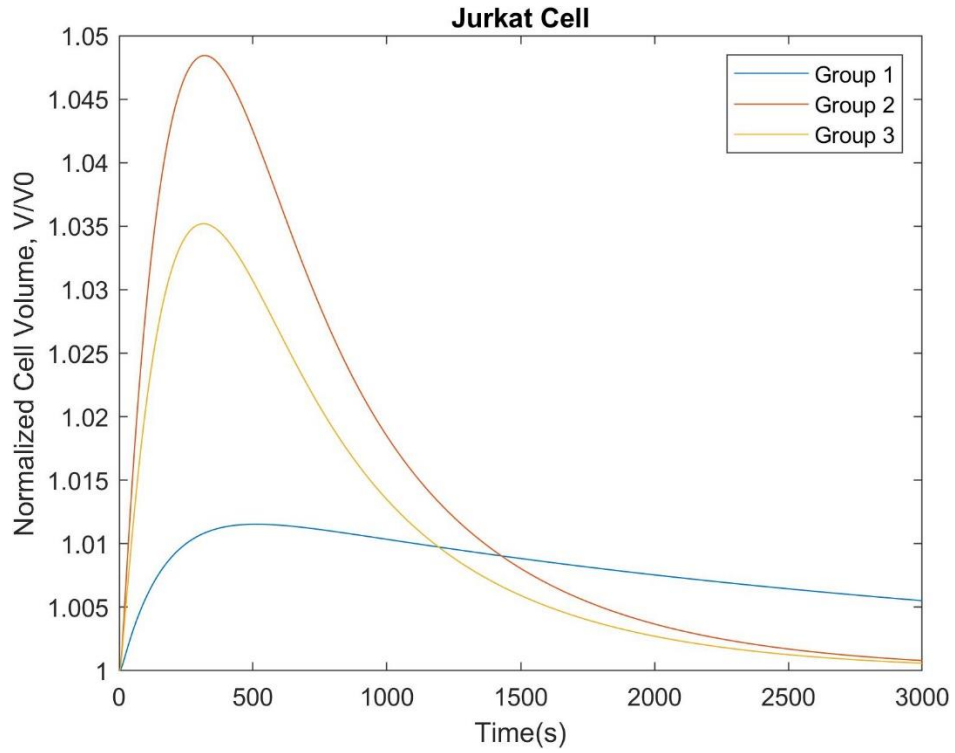

Figure 4.5. Jurkat cell volume change with different CPA removal approaches

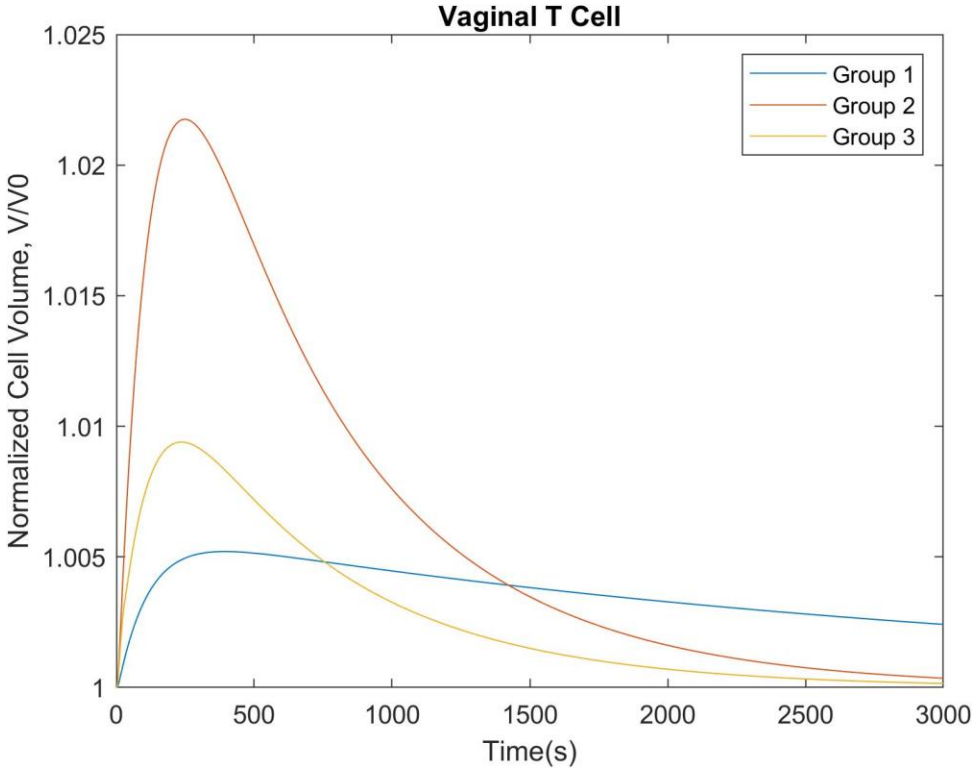

Figure 4.6. Human vaginal T cell volume change with different CPA removal approaches

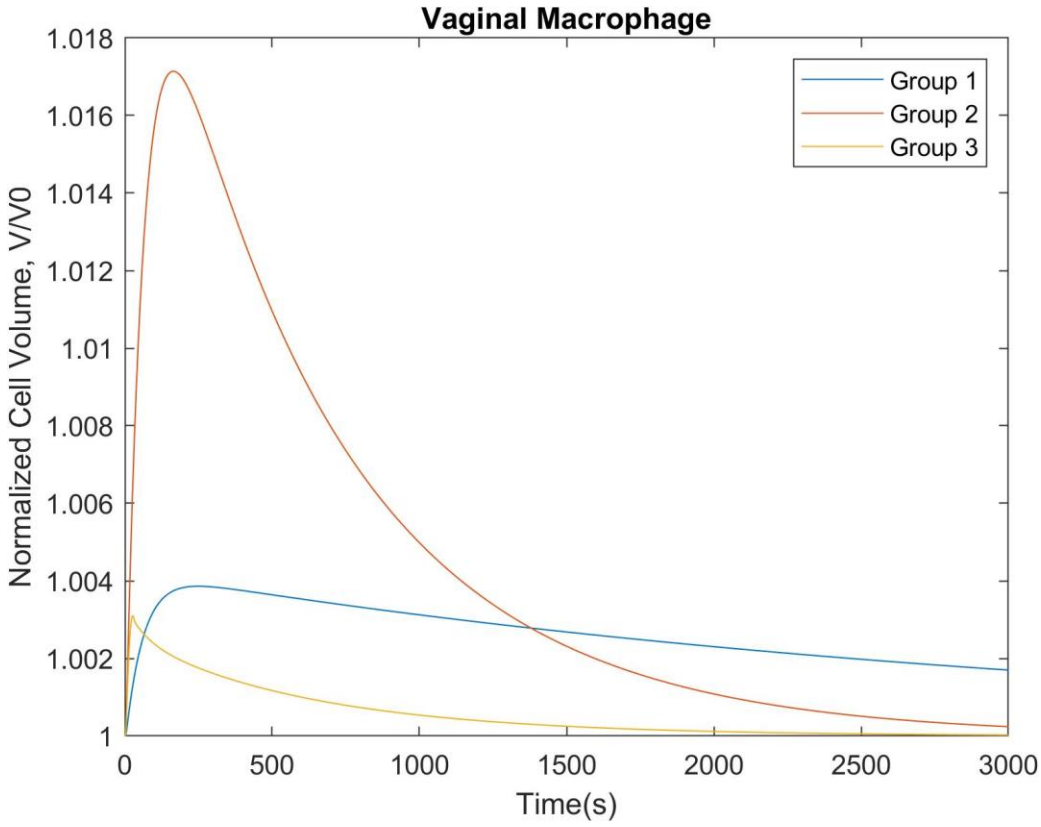

Figure 4.7. Human vaginal macrophage volume change with different CPA removal approaches

4.4.3 *Selection of the fastest dilution rate with the isotonic method*

According to the simulation of volume change with different approaches in the previous subsection, it takes too much time, longer than one hour, to remove CPA for the group 1 method. Thurs, group 1 was not selected for further consideration and simulation. Group 2 and 3 were renamed as isotonic and hypertonic methods, respectively, based on different dilution solutions. To demonstrate cell volume excursion clearer, the initial osmolarity of cell suspension has been increased to 4000 mOsmol/L. The CPA solutions at that high osmolarity, or even higher, are called vitrification solutions, widely used for cryopreservation to avoid ice formation during the cooling process[1].

Once the isotonic method is selected, as shown in Figure 4.8, the removal rates of CPA are directly related to the flow rates of dilution and ultrafiltration, which are set to be the same during the CPA removal process volume constant. The faster dilution and ultrafiltration, the quicker CPA is removed. However, the increase of dilution rate would also cause worse cell swelling, as shown in Figure 4.9. In this case, Figure 4.10 shows that the removal of CPA becomes the trade-off problem between removal speed and cell excursion. The multifunctional cell processing system provides an editable standard for cell excursion. For example, 5% expansion was selected as the maximal tolerance for Jurkat cells, and Figure 4.10 shows that 39 mL/min is the maximal flow rate under this limitation.

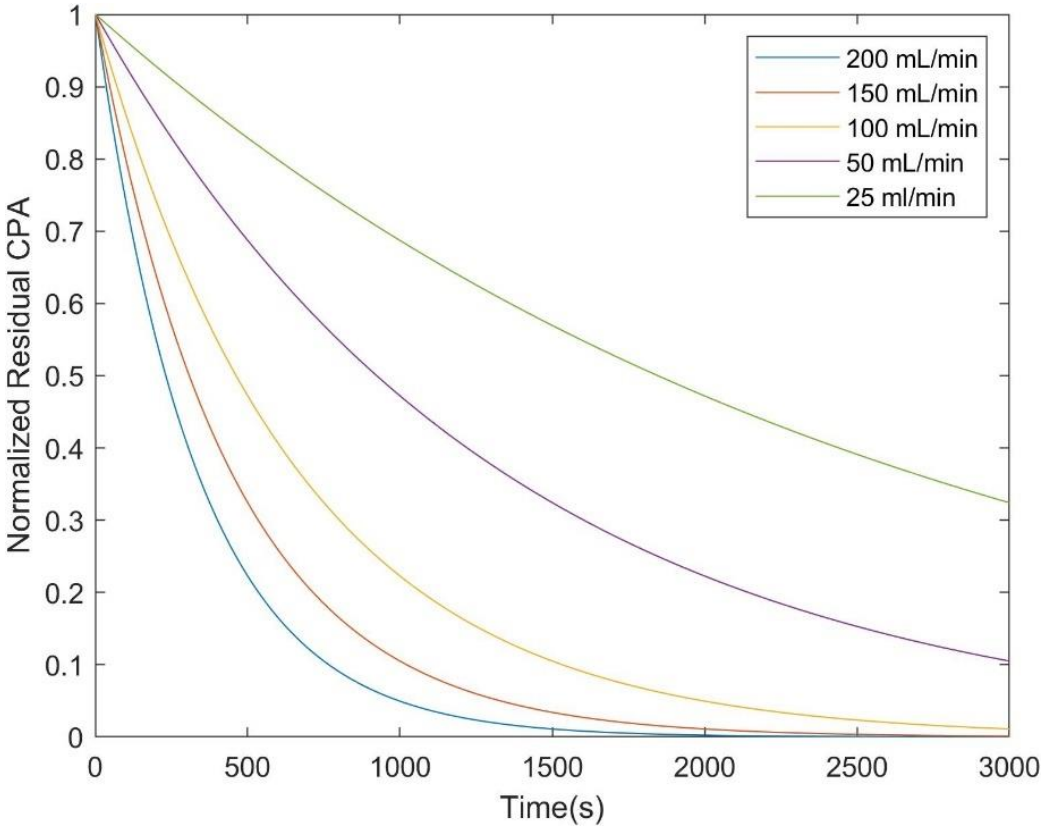

Figure 4.8. Normalized residual CPA with different dilution rates on isotonic mode.

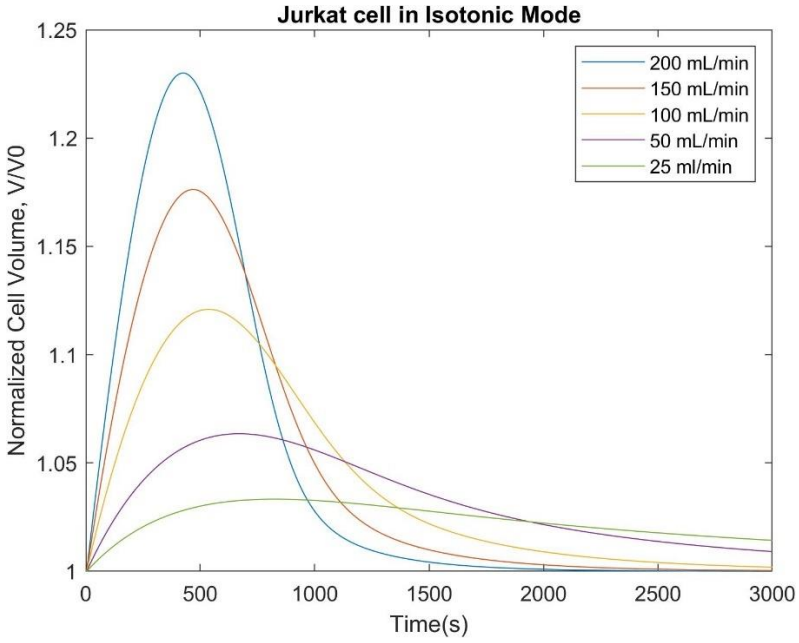

Figure 4.9. Normalized cell volume change with different dilution rates for Jurkat cell in isotonic mode

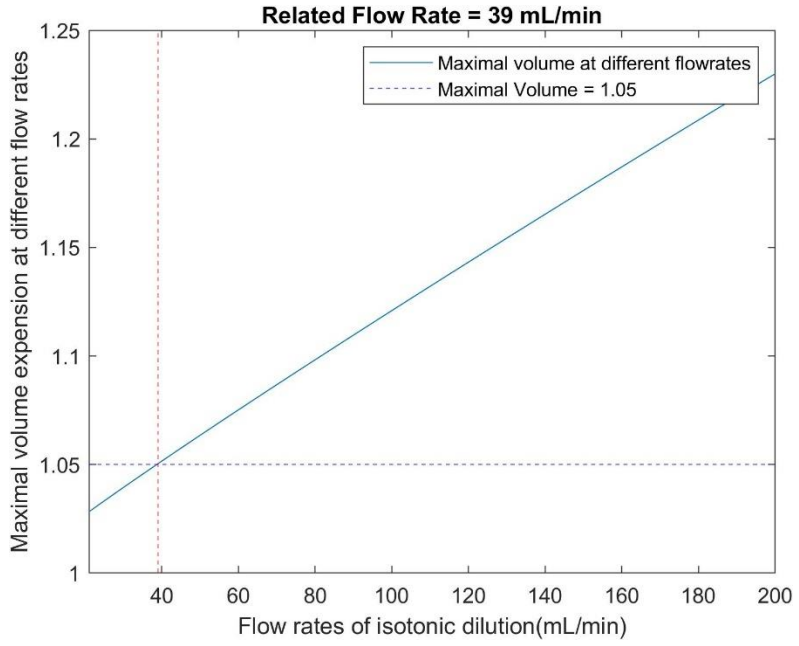

Figure 4.10. Selection curve for isotonic mode

4.4.4 *Selection of minimal volume change with the hypertonic method*

Once the hypertonic mode is selected, the cell suspension will be diluted by hypertonic solution in the first-half minute and isotonic solution in other times. The osmolarity of hypertonic saline solution has a considerable impact on the cell volume change during CPA removal. The cell volume change of Jurkat cell with different hypertonic saline solution in the first-half minute has been shown in Figure 4.11. According to the simulation results, the higher osmolarity of the hypertonic saline solution, the lower peaks of cell volume curves would be obtained. Once the osmolarity is more significant than a particular value related to the cell membrane properties, cells would suffer a shrink after a small peak at the very beginning. With a higher osmolarity, the curve will obtain a deeper valley. This phenomenon could help us obtain a theoretical optimal CPA removal protocol in hypertonic mode. The cell volume change will be accumulated and compared. No matter what initial conditions it has, the "selection curve" shown in Figure 4.12 will give us a theoretical optimal hypertonic solution to achieve minimal cell excursion.

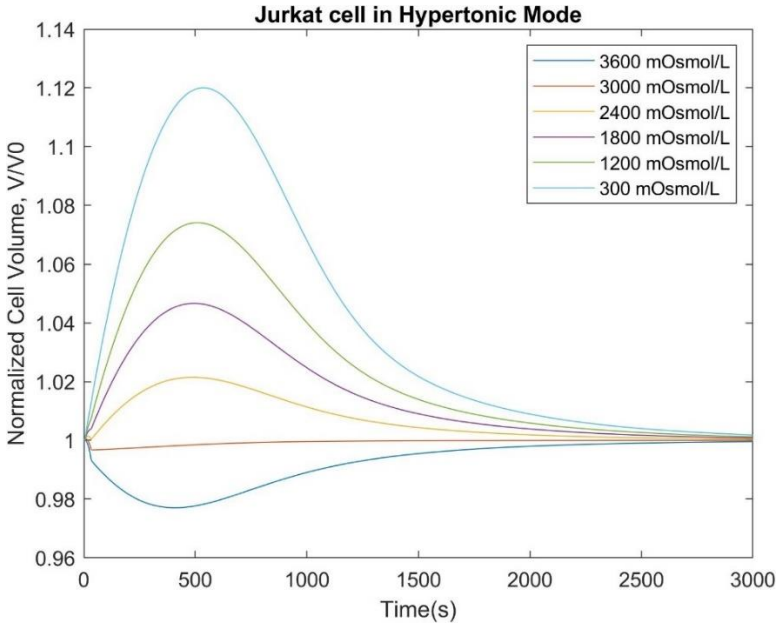

Figure 4.11. Normalized cell volume change with the different hypertonic solution in a first-half minute on the hypertonic mode

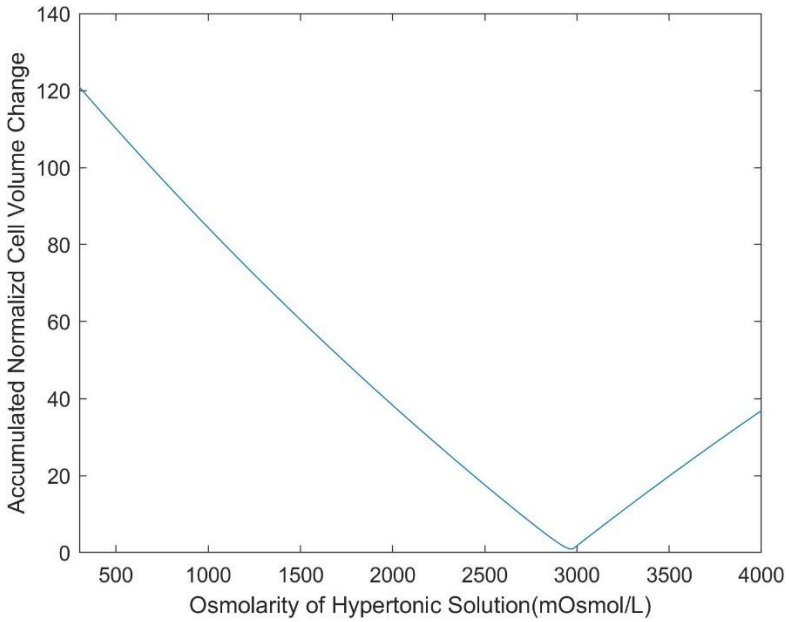

Figure 4.12. Selection curve for hypertonic mode

4.4.5 *Performance of concentration*

The results of concentration experiments can be found in Figure 4.13. The theoretical curve had been plotted based on Equations (4.14),(4.15). Cell concentrations were counted every 2 min for three times. The final recovery rate of Jurkat cells is 86.0%.

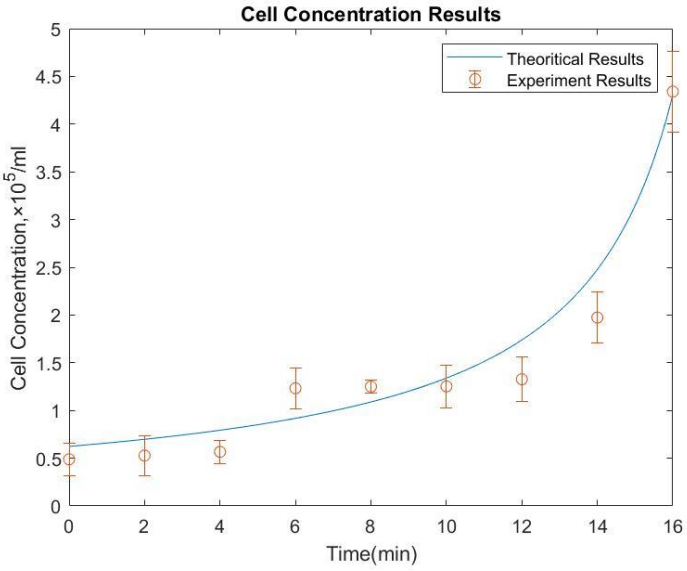

Figure 4.13. Cell concentration function of the multifunctional cell processing system

4.5 DISCUSSION

The multifunctional cell processing system is necessary to improve the CPA removal process and further the cell preparation process. It highly decreases the processing time and osmotic injury during the CPA removal process. Compared with the traditional centrifuge method, the multifunctional cell processing system can reduce cell clumping and loss, stem cell activation, and contamination risk. Another huge advantage of the system is that all these post-cryopreservation procedures can be automatically performed. Pumps, valves in this closed system can be controlled by PC or other processers without manual operation needed during centrifuge, which will induce personal error and uncertainty. To probe the scenarios of CPA removal, simulation models and algorithms are built. A cell-free experiment first validated the simulation model. The results showed that the assumptions are reasonable, and theoretical results can be used as a reliable reference for further investigation.

According to the cell volume results based on the validated numerical model, cell properties' excursion is mainly determined by cell properties, including L_p, P_s, diameter, and inactive volume. Comparing the results shown in Figure 4.5, 4.6, 4.7, and Table 4.7, with the same dilution protocol, three different cells have different responses. Generally, traditional low-speed isotonic dilution (group 1) would cause very mild osmotic injury to cells. But it takes too much time for the CPA removal process, and the cell would stay in a high-CPA solution for a long time, which might induce cell damage caused by the toxicity of CPA. High-speed isotonic dilution and hypertonic dilution (groups 2 and 3) have similar CPA removal performance. Hypertonic dilution can further reduce osmotic injury by balancing water influx and CPA outflux of cells. Based on the results, as for CPA removal starting from middle-level osmolarities, such as 1800 mOsmol/L for 10% DMSO, the cell excursion is less than 5% no matter which dilution mode is selected. The isotonic

mode could be a potential option if mild cell excursion can be tolerated since the isotonic mode is relatively simpler to operate. But if the vitrification solution or other high-CPA solution is the operation sample, the hypertonic mode will be the desired selection to reduce severe cell swelling.

In other words, with the given cell properties, the specific CPA removal protocol or treatment can be generated by the algorithm derived from mass transfer equations. Based on this theory, isotonic and hypertonic modes had been further improved. As shown in Figures 4.8 to 4.12, isotonic mode pursuits simpler and faster removal under given tolerance, while the hypertonic mode is looking for minimal osmotic injury.

Cell concentration function can be operated individually or included as part of post-cryopreservation procedures depending on needs. In-vitro experiments have been conducted, and the results are very promising.

Besides developing the multifunctional cell processing system and algorithms, the interesting relation between cell properties including L_p, P_s, diameter, and inactive volume was also noticed. In a specific combination of these parameters, the cell can balance its water influx and CPA outflux itself during the CPA removal process. It could explain why some cell kinds are easier to be successfully cryopreserved while others are not. We will keep investigating this phenomenon in our future research.

4.6 CONCLUSION

A multifunctional cell processing system and related auto-generated CPA removal protocol are developed, achieving both CPA removal and cell concentration functions. Applying optional hypertonic dilution and an advanced algorithm with cell properties as parameters, the optimal CPA removal approach will be generated to minimize cell shrinkage and swelling during the post-cryopreservation process. Compared with the traditional centrifuge method, this novel

system/method can provide a sterile, automatic, and less osmotic/mechanical injury option for academic and clinical research.

Chapter 5. DEVELOPMENT OF HEAT TRANSFER MODELS AND THERMAL STRESS ANALYSIS DURING REWARMING PROCESS

5.1 INTRODUCTION

Biological materials that survived the cooling process could also be killed by the warming and thawing process. Recrystallization is the major fatal factor during the warming process, which means some intracellular water stay supercooled during the cooling and storage processes but format intracellular ice crystal during warming. Intracellular ice formation(IIF) is one of the main reasons for cell injury during cryopreservation. To prevent IIF from happening, the sample's warming rate should be fast enough so that it can reach the melting point of the intracellular solution before large-scale IIF. Another main fatal factor during the warming process, especially for large specimens such as tissue and organs, is the nonuniform rewarming, which results in thermal stress in the materials and causes irreversible damage.

The discussion and concerns about thermal stress during tissue and organ cryopreservation was started earlier than the 1970s[72–74]. Dr. Rubinsky used mathematical models to investigate temperature distributions and thermal stress during the cryopreservation of organs. Fahy discussed the fracturing caused by thermal nonuniformity during the cooling process of vitrification of large biological systems[83]. Dr. Robin developed a new model of thermal stress in cryosurgery[76-77].To evaluate the thermal stress with more accurate parameters, he also developed a new experimental apparatus and measured the thermal expansion of DP6 and VS55, two common vitrification solutions[78-80]. Dr.He established a multiphysics finite element model with ANSYS

to analyze thermal stress during cryosurgery of kidneys[89]. Baicu and Pascual further proved the importance of the uniformity during the rewarming process with biological experiments[82-83].

In this chapter, numerical models of different warming methods during cryopreservation were established and validated with experiments. The numerical models include conductive heat transfer in freezing medium and cylindrical containers and convective heat transfer between the container's exterior surface and warming fluid(air and water). The validated models were further used to investigate thermal stress during rewarming by virtualizing temperature gradients spatially and temporally. The natural air rewarming approach was proposed as a better option than the water-bath method considering the temperature gradient results. The size of the container and placement of tissue or organs during cryopreservation were also discussed considering thermal stress analysis results.

5.2 MATERIAL AND METHODS

5.2.1 *Heat transfer modeling*

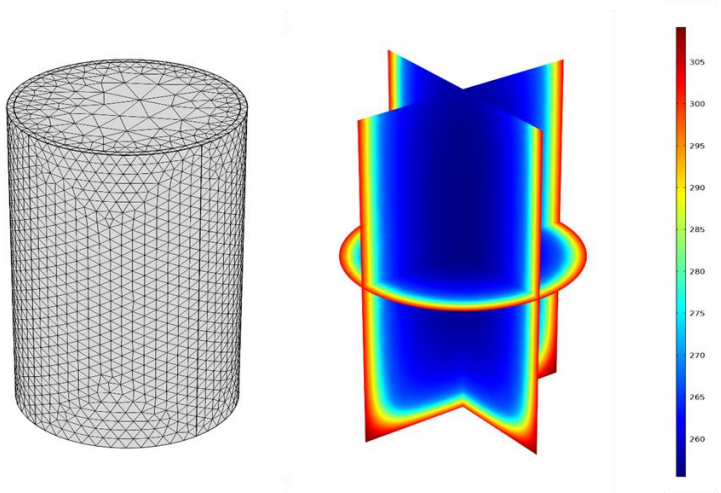

Figure 5.1. a) Geometry and mesh of heat transfer model for natural air and water-bath rewarming. b) Temperature distribution of sample solution during water-bath rewarming at T=120s

The shaking water-bath and natural air rewarming models are conducted with COMSOL in this study. The geometry of these two models is the same, shown in Figure 5.1, and the only difference is the convective heat transfer coefficient on the beaker's exterior surface. The heat transfer of the sample solution and the beaker is governed by:

$$\frac{\partial}{\partial x}\left(k\frac{\partial T}{\partial x}\right)+\frac{\partial}{\partial y}\left(k\frac{\partial T}{\partial y}\right)+\frac{\partial}{\partial z}\left(k\frac{\partial T}{\partial z}\right)=\rho c_p\frac{\partial T}{\partial x} \tag{5.16}$$

There is no internal heat source term since heat is transferred into the system by convection at the boundaries. The heat flux at the exterior surface of the beaker can be described by Equation (2.4).

5.2.2 *Evaluation of convective heat transfer coefficients*

As for water-bath rewarming, the beaker with sample solution was rewarmed in 37℃ SB-12L Shaking Water Bath (Benchmark Scientific) with 120 RPM. In this case, the cylinder in the crossflow model was applied in our calculation. To evaluate the average convective heat transfer coefficients, the average Nusselt numbers were first determined by the correlation due to Hilpert[92]:

$$\overline{Nu}_D = 0.683Re_D^{0.466}Pr^{1/3} \tag{5.17}$$

Then, the heat transfer coefficients can be obtained($h=\frac{k}{D}Nu$).

As for the natural air rewarming, the beaker with sample solution was placed in the air at room temperature. In this case, the free convection with the vertical plate model was applied in the calculation. To evaluate the average convective heat transfer coefficients, the average Nusselt numbers were first determined by the correlation due to Churchill and Chu[93]:

$$\overline{Nu}_L = \{0.825+\frac{0.387Ra_L^{1/6}}{[1+(0.492/Pr)^{9/16}]^{8/27}}\} \tag{5.18}$$

where Ra is the Rayleigh number defined as:

$$Ra_L = \frac{g\beta(T_s - T_\infty)L^3}{\nu\alpha} \quad (5.19)$$

All temperature-dependent properties during the calculation of convective heat transfer coefficients are evaluated at the film temperature, $T_f = \frac{T_s + T_\infty}{2}$, with the linear interpolation of data from Bergman and Lavine[94].

The calculated convective heat transfer coefficients, shown in Figure 5.4, were employed to calculate the heat flux at the beaker's exterior surface as the boundary conditions.

5.2.3 *Determination of thermal properties*

In our numerical simulation and experiments, 10% DMSO + 0.25 M trehalose in PBS was used as the freezing solution. The thermal conductivity *k* and heat capacity c_p of the solution was extremely important for the numerical modeling.

Thermal conductivities of the freezing solution were measured with a thermal-needle approach using a microfabricated thermal conductivity sensor. The sensor was designed by former lab members Liang at el[95] and assembled in Washington Nanofabrication Facility. As shown in Figure 5.2, the other components in the measurement system including, CryoMed controlled rate freezer, a digital multimeter, and a data acquisition system(Integra 2700, Keithley, Cleveland, OH).

The temperature-dependent heat capacity of the freezing solution was determined by a differential scanning calorimetry (DSC 8500, Perkin Elmer, Waltham, MA), shown in Figure 5.3, which measures the difference of the heat flow between the target solution and reference solution during the warming process.

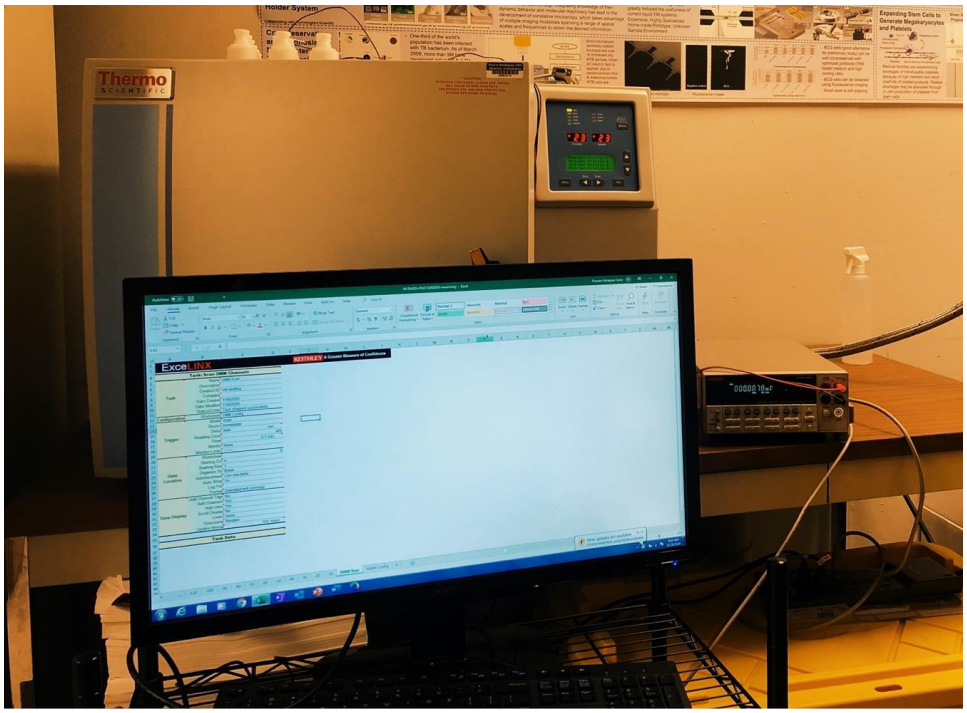

Figure 5.2. Setup of the thermal-needle approach using a microfabricated thermal conductivity sensor.

Figure 5.3. Perkin Elmer DSC 8500 used to determine the heat capacity of the sample solution.

5.2.4 *Warming experiments of large samples*

The 10% DMSO + 0.25 M Trehalose in PBS was the sample solution for numerical simulation and warming experiments. A cylindrical beaker made by Pyrex was chosen as the container of the sample solution. The 25ml beaker with sample solution was placed in -80℃ freezer overnight and ready for the rewarming. Two thermocouples were inserted into the sample solution to monitor the temperature profiles of during the rewarming process. One of the thermocouples is at the beaker's center, while the other is at the same elevation but the beaker's internal surface (no contact with the beaker).

For the water-bath rewarming method, the sample holder at -80℃ was fully immersed into 37℃ water bath. The holder was shaking at 120 RPM in an orbital motion until the thermal couple reading reached 0 ℃, and no clear ice crystal was observed.

The sample holder was placed on the countertop at room temperature for the natural air rewarming method until the thermocouple reading reached 0 ℃, and no clear ice crystal was observed.

5.3 RESULTS

5.3.1 *Thermal Properties of Sample Solution*

The thermal conductivity and specific heat were measured with the microfabricated sensor and DSC, respectively, shown in Figure 5.4. The experiments were conducted by Shen[96].

5.3.2 *Calculation of convective heat transfer coefficients*

The calculated convective heat transfer coefficients for different rewarming methods are shown in Figure 5.5. The x-axis is the temperature of the exterior surface. The orange line

represents the coefficients for water-bath rewarming, using the right y-axis. The coefficient increased from 1283 at -33℃ to 1534 at 32℃. The increase of the coefficient was mainly related to the decrease of the viscosity. The blue line represents the coefficients for natural air rewarming, using the left y-axis. The coefficient decreased from 10.4 at 180 ℃ to 2.08 at 295 ℃. The decrease of the coefficient was mainly related to the decrease of the temperature difference between the exterior surface and air, which resulted in a smaller Rayleigh number showing weaker buoyancy-driven flow near the surface.

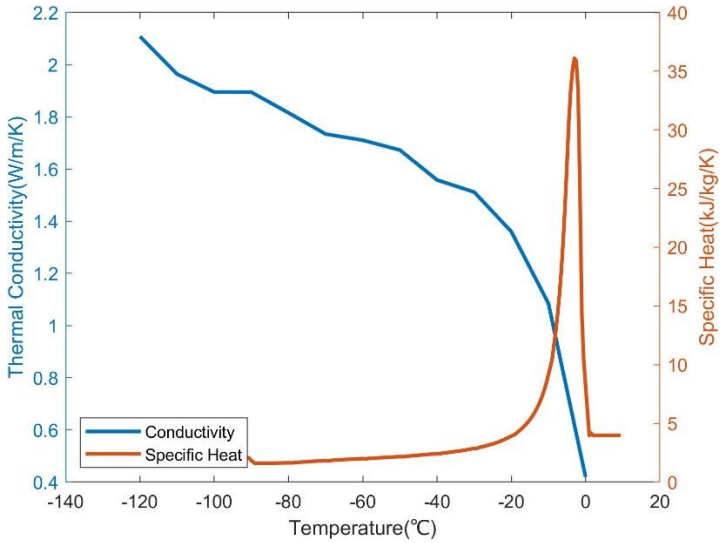

Figure 5.4. Specific heat and thermal conductivity of sample solution.

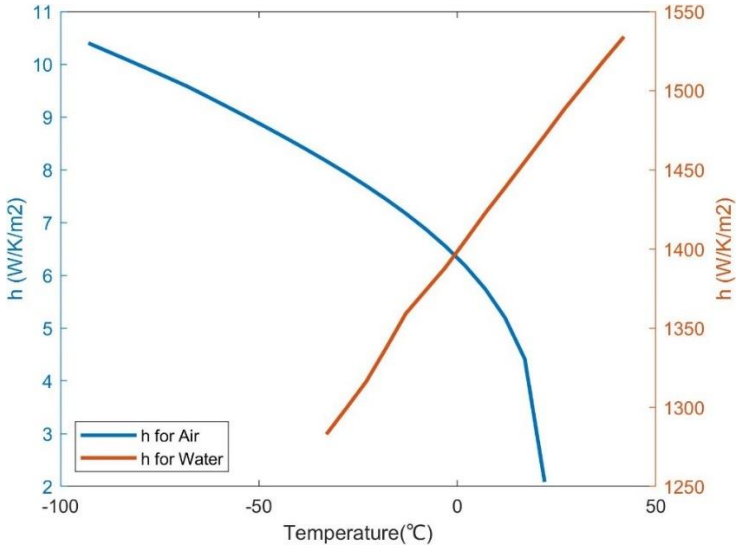

Figure 5.5. Convective heat transfer coefficients between the exterior surface of the beaker and external fluid

5.3.3 *Validation of heat transfer models*

The simulated temperature profiles at the center point and side point for each rewarming method were plotted in Figures 5.6 and 5.7, compared with experiment results. Experimental rewarming curves were measured by a thermocouple (N=6 for natural air, N=7 for water bath), and the standard deviation(SD) was shown as the error bars on the curves.

For water-bath rewarming, simulated results and experiment results fitted very well, and the maximal difference is 5.63 K around the phase change process near 0℃. Simulated temperatures at the center point have good similarities to the experimental data but were not as close as side ones, especially for the end part. The significant differences during the last 50s are probably caused by the central unmelt part movement, which works as a mixing bar in the beaker. This “mixing bar” highly helped rewarming rate and uniformity.

For the natural air rewarming method, the simulated results were very close to the experiment data at the first 50 minutes. The temperature difference increased once the sample solution entered the phase change region.

Overall, the models were validated, and the temperature distributions calculated by these models are credible.

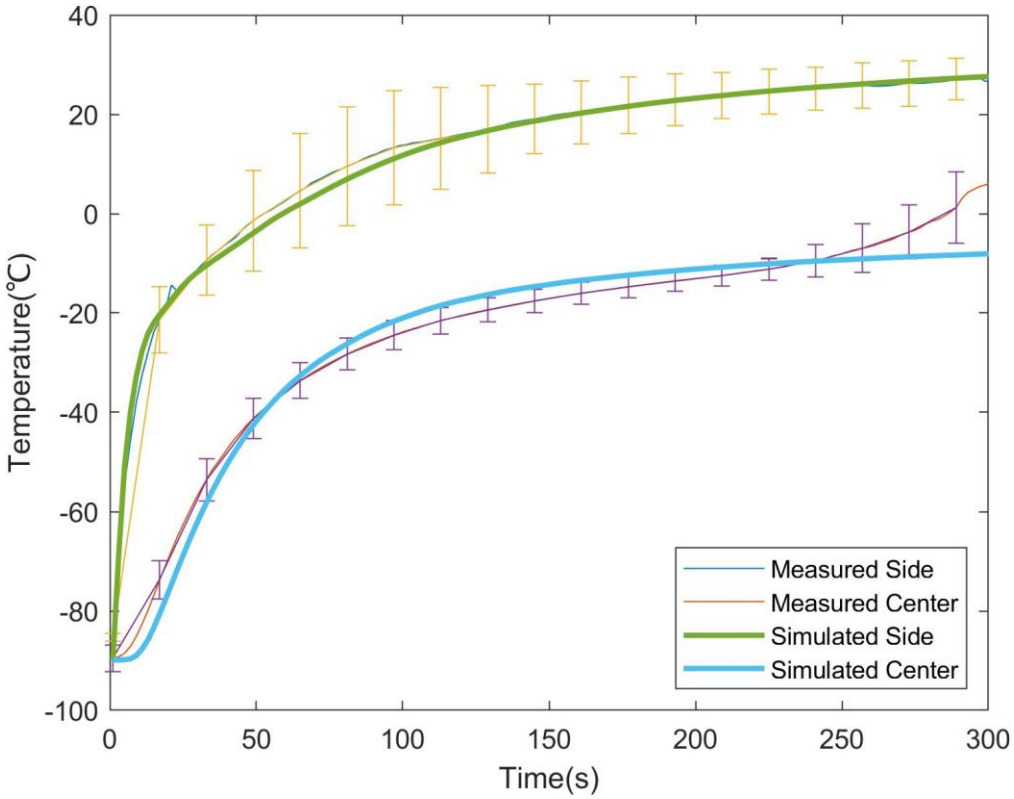

Figure 5.6. Experiment and simulation results of water-bath rewarming

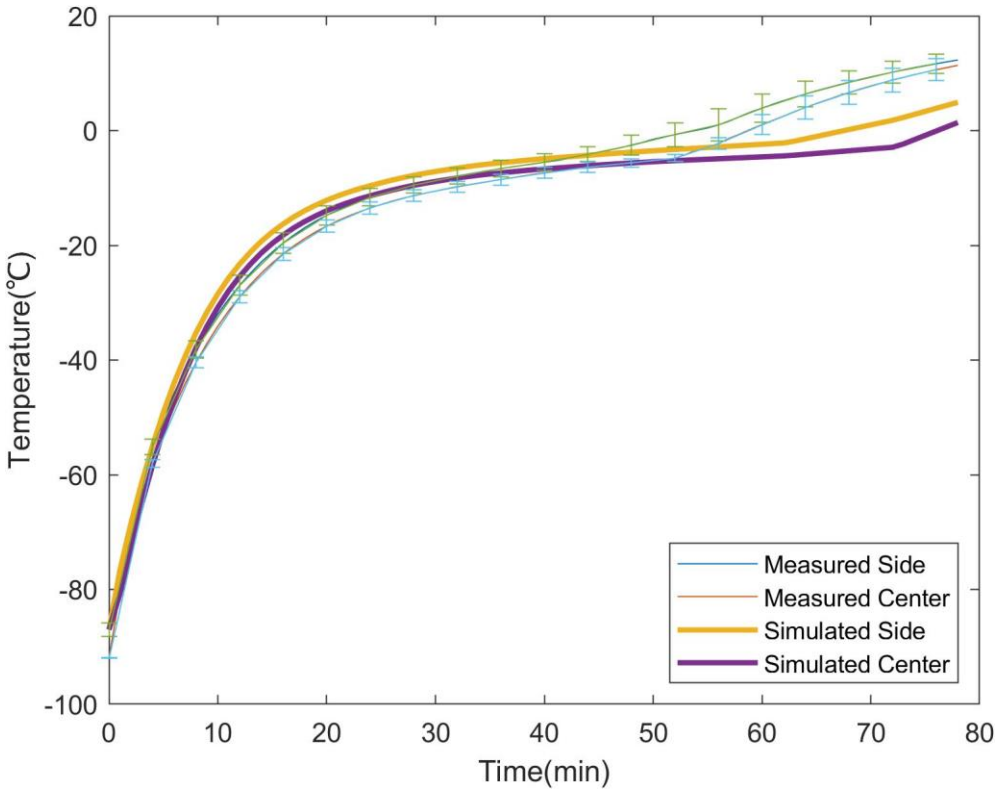

Figure 5.7. Experiment and simulation results of natural air rewarming

5.3.4 *Temperature gradients according to validated heat transfer models*

The validated models were employed to simulate temperature gradients during the rewarming process with different warming methods. The temperature data along the central radius, shown in Figure 5.8, were selected.

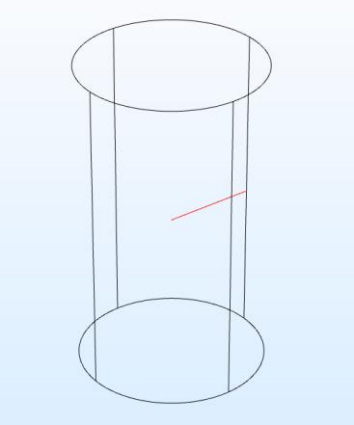

Figure 5.8. Central radius (red line) of the sample solution

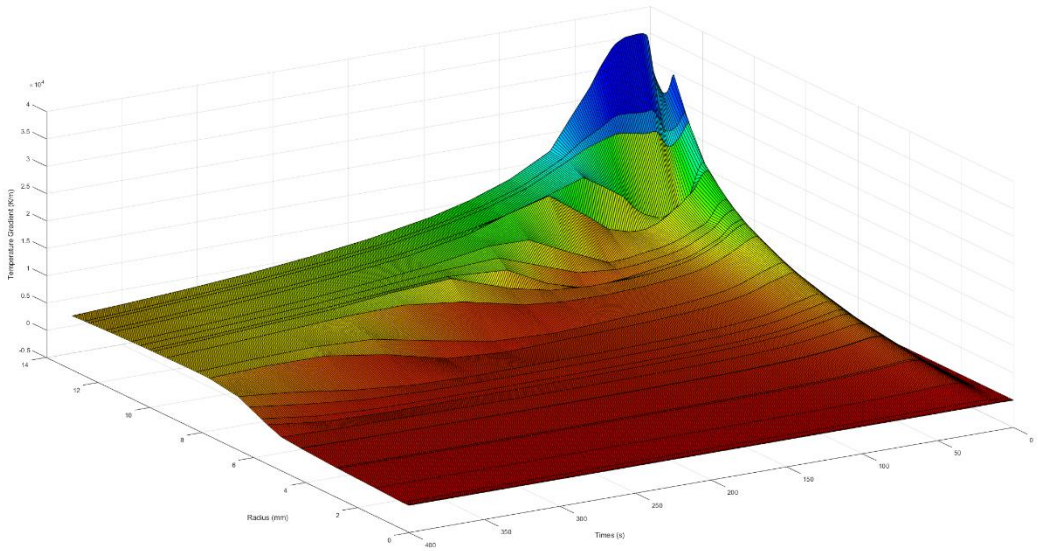

Figure 5.9. Temperature gradients at the central radius during water-bath rewarming process

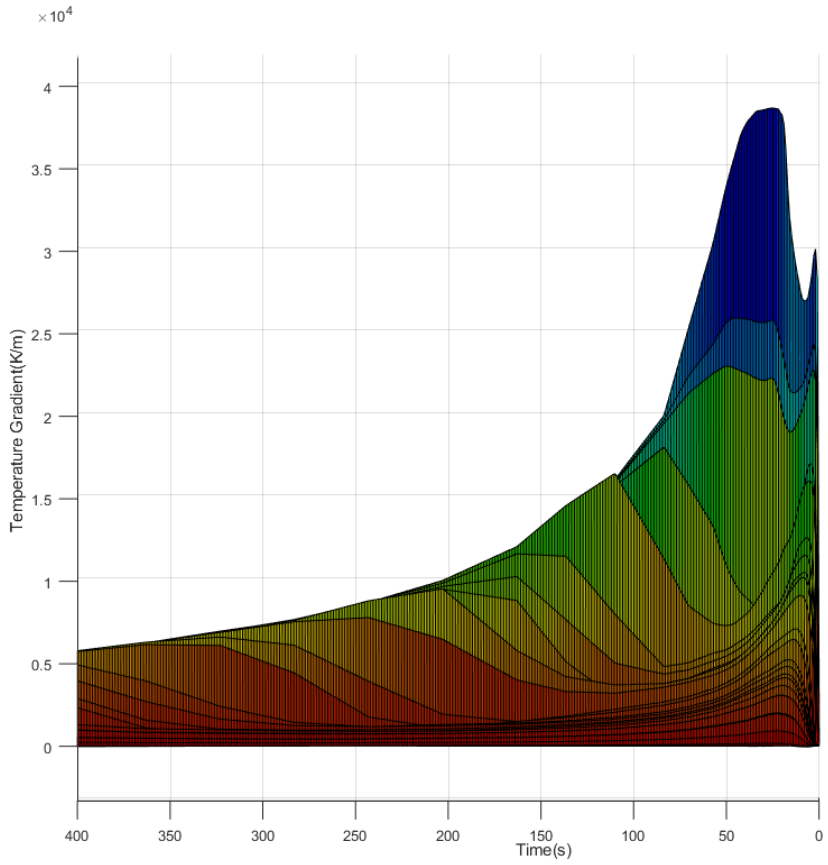

Figure 5.10. Maximal temperature gradients at each second observed by looking at Figure 5.8 in the radius direction

According to the spatial and temporal temperature gradients of water rewarming shown in Figures 5.9 and 5.10. The maximal temperature gradient happened at the sample solution's contact surface and beaker at t = 13s, which is as large as 38473 K/m. After that, the magnitude of maximal temperature gradients decreased as the rewarming process went by. The locations of transient maximal temperature gradients moved toward the center of the sample solution.

As for natural air rewarming, the first peak temperature gradient happens at t = 2 min, 655.3 K/m. The maximal temperature gradient is 687.8 K/m, happening at t = 73 min. In general, the temperature gradients of this warming method are stable. In most times, the outer temperature gradients are more significant than the inner ones.

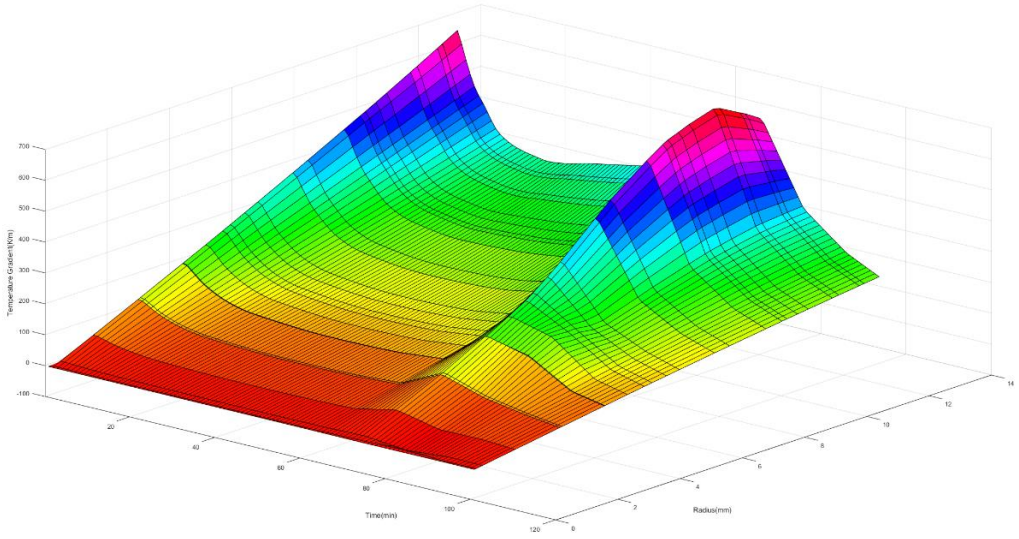

Figure 5.11. Temperature gradients at the central radius during the natural air rewarming process

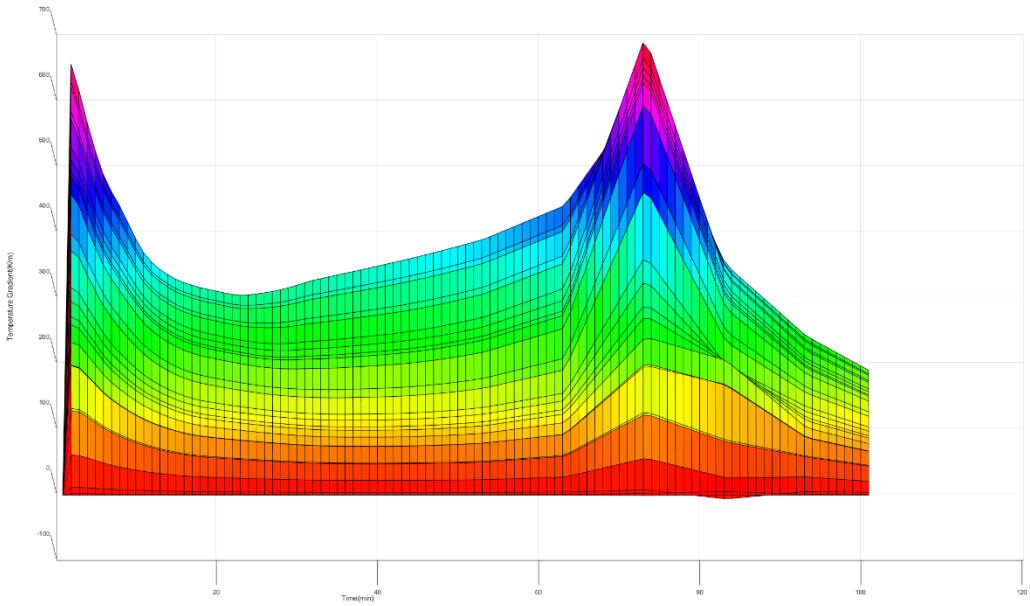

Figure 5.12. Maximal temperature gradients at each second observed by looking at Figure 5.10 in the radius direction

5.4 DISCUSSION

The mechanisms of injury related to the mechanical stress associated with the material's thermal expansion, known as “thermomechanical stress, " have been discussed since the 1970s[78-81]. It is known as the cause for fractures during cryopreservation, which is lethal for tissues and organs. The magnitude of thermal stress σ is positive correlated to the gradient of temperature($\sigma \propto \nabla T$). In this study, the distribution of the temperature gradient during the rewarming process have been calculated by validated heat transfer models.

The consistent results of simulation and experiment proved the reliability of the numerical model. The central unmelt solid movement worked as a “mixing bar” to enhance rewarming rate and uniformity, which was not considered in the simulation model. In this case, two curves of central temperature didn’t fit very well. The same situation may also happen in the natural air warming model. Even though some mismatches happened in a particular region, the overall model and simulated results are credible.

According to the water-bath rewarming results, the transient maximal temperature gradient moved toward the center direction as the rewarming process went by. The maximal temperature gradient at the last second of the experiments was located around half radius. Based on these results, the placement of the sample in the beaker is crucial to avoid thermal stress. If the tissues or organs are placed in the central area, they might experience a relatively uniform rewarming. However, the thermal stress would be tremendous if these biological materials are placed near the beaker's surface.

Furthermore, the size of the container might play an essential role in tissue cryopreservation. A relatively larger container would provide a “buffer zone” for the central region's biological

materials. A very “fit” container will force the sample to endure the high thermal stress caused by a large temperature gradient.

Comparing the temperature gradient results for both models, the natural air rewarming method was proposed as the better option for tissue and organ cryopreservation. The maximal temperature gradient of the water-bath rewarming is 56 times that of natural air rewarming. The experiment results can generate a similar conclusion by Baicu[90] and Pascual[91]. Baicu conducted experiments to evaluate contractile function in response to the agonists norepinephrine and phenylepinephrine of the cryopreserved carotid segments. It showed a significantly better result in the slowly rewarmed group of carotid segments (74 ± 9% and 62 ± 11%, respectively) than for the more rapidly warmed group 31 ± 7% and 45 ± 15%, respectively)[90]. Pascual concluded that slow rewarming better preserved the structure, shown in Figure 5.13, and viability of pig iliac arteries[91].

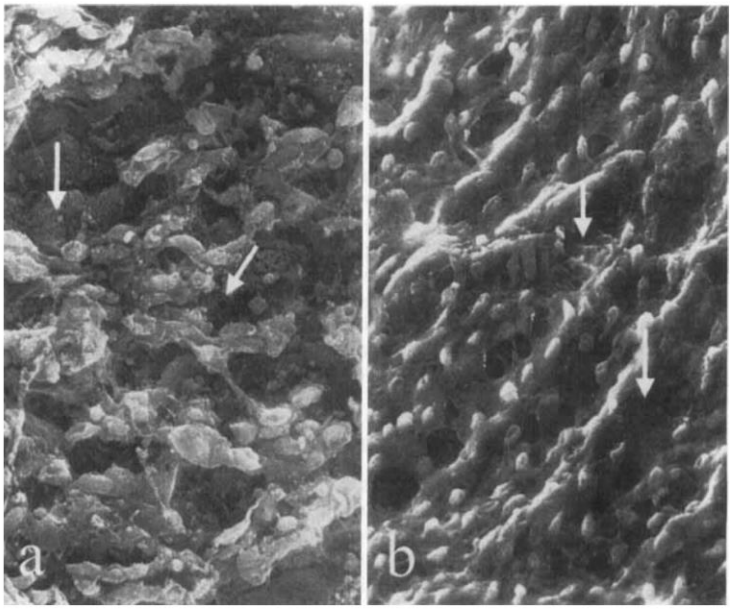

Figure 5.13. Denuded areas(arrows) of the vascular endothelium after a) rapid and b) slow thawing with exposure of a dense subendothelial matrix. These patches are most extensive after rapid thawing[91]

5.5 CONCLUSION

In general, heat transfer models for water-bath and natural air rewarming processes for the large sample were developed and validated by the experiment. The validated models were then employed to calculate the temperature gradients spatially and temporally. The temperature gradients results showed that natural air rewarming is a better method for tissue and organ cryopreservation, which has relatively more minor thermal stress during rewarming. Some suggestions about the sample's location in the container and the size of the container were also discussed.

Chapter 6. DETERMINATION OF THE WATER PERMEABILITY(L_P) OF JURKAT CELLS AND ITS ACTIVATION ENERGY AT SUBZERO TEMPERATURES

6.1 INTRODUCTION

According to the "Two-factor hypothesis", the cells undergo a shrinkage process during the cooling. Two critical factors determining the degree of shrinkage at various cooling rates to subzero temperatures are the cell membrane permeability to water, L_p, and its temperature coefficient or activation energy, Ea. The microfluidic method has been applied in previous chapters to measure the suprazero theses cell membrane properties with solution switch, microscopy, and on-chip heating and cooling. The assumption has generally been that the L_p values obtained from suprazero cell volume changing can be extrapolated to subzero temperatures. However, this assumption might not be correct.

Some direct measurements have been conducted and can be divided into two categories: cryomicroscopy method and differential scanning calorimetry(DSC) method. The former method combines a cryostage with the microscope to measure the cell volume excursion at certain subzero temperatures. It fits the experiment data with L_p and E_a at adjustable parameters. However, this method requires a long working distance for lenses and complex light pathways, making it hard to get accurate cell volume excursion assessment in image analysis. Another intractable problem is that the external ice nearly obscures the cells at sub-freezing temperatures, and cells are usually distorted. The second method uses DSC to measure the heat flow histograms of dead cell suspension and alive cell suspension, respectively. The difference between the two curves can be interpreted as the volume change during the cooling, and the same fitting process is needed to get L_p and E_a. However, the assumptions made during this method, including all cells are alive during

the first slow-cooling step and all cells are dead after the fast-cooling step, might not be correct. What's more, this method can only determine the subzero L_p and E_a when no CPA exists, which are not suitable for cryopreservation in the actual cases when CPA usually is inevitable.

In this study, an inverse method to determine the subzero L_p and E_a with cell recovery rate results was proposed. Following the "10 percent" restriction and "Two-factor hypothesis", the cooling rate achieving the highest cell recovery rate was used to fit the Mazur-Toner's water transport model and Arrhenius equation during the cooling process with L_p and E_a as the adjustable parameters. The cell recovery experiments of Jurkat cell were conducted and used to determine subzero L_p and E_a for Jurkat cell.

6.2 METHODS

6.2.1 *Cell preparation*

Jurkat cells were cultured in an incubator (VWR International, Radnor, PA) that setting at 37 ℃, 5% carbon dioxide, and proper humidity. The cell growth medium consists of 450 mL RPMI medium (Life Technologies, Carlsbad, CA), 50 mL fetal bovine serum (Life Technologies), 5 mL Penicillin-Streptomycin (Life Technologies), and 5 mL L-glutamine (Life Technologies). The experiments were conducted once the cell concentration reaches $1 \times 10^6 mL^{-1}$. The stock solution (20%(v/v)DMSO + 0.5 M trehalose) was added to the cell suspension slowly with a dropwise method until the final concentration of CPA(10%(v/v)DMSO + 0.25 M trehalose) was reached. The CPA addition process was performed on ice to compensate for the heat released from DMSO dissolving.

6.2.2 *Cooling device and protocol*

A programmable controlled rate freezer (CryoMed 7456, ThermoFisher Scientific) was implemented to achieve different cooling rates under controlled cooling processes. From slow to fast, the cooling rates were 0.1, 0.5, 1, 5, 10, and 20 ℃ min−1, respectively.

An example of the 0.1℃/min cooling protocol for the controlled rate freezer is given as follows:

1) Wait at 4 ℃,

2) Cooling the sample temperature to −4 ℃, at 1 ℃ min−1,

3) Cooling the chamber temperature to −40 ℃, at 25 ℃ min−1,

4) Heating the chamber temperature to −12 ℃, at 10 ℃ min−1,

5) Cooling the sample temperature to −85 ℃, at 0.1 ℃ min−1,

6) The cooling ends at -85 ℃.

2 mL of sample solution (1 mL cell suspension + 1 mL CPA) was used as the sample volume with cooling rates at 0.1, 0.5, and 1 ℃/min. Considering the cooling capacity of the controlled rate freezer may not fulfill the cooling needs, a smaller volume of 500 μL (250 μL cell suspension + 250 μL CPA) was selected to achieve the faster cooling rate at 5, 10, and 20 ℃/min.

6.2.3 *Modification of the calculation method for cooling rate*

Steps 3 and 4 of the cooling protocols discussed in the previous section were meant to seed the ice crystal to avoid large supercooling, the shift shown in the sample solution's cooling curves. Then, the cooling rate was controlled in step 5. However, the water transportation across the cell membrane started when the shift happened, the extracellular ice started formatting, and ended around -35℃, the eutectic temperature of the sample solution[97]. Under the IIF mechanism, only

the cooling rate in this region should be considered the theoretical analysis parameters. In this case, updated average cooling rates of original 5, 10, and 20 ℃/min groups were recalculated in the water transport region and worked as the parameters in the cell recovery rate and activation energy analysis.

Table 6.8: Updated cooling rates for original 5, 10, and 20 ℃/min groups

Original Cooling rates(℃/min)	Ice formation starting time(min)	Ice formation starting temperature(℃)	Eutectic time (T =−35℃)(min)	Updated cooling rate(℃/min)
5	19.88	-4.02	45.98	1.19
10	20.35	-5.93	39.63	1.51
20	21.75	-7.50	37.80	1.71

6.2.4 *Determination of cell recovery rate*

As for the rewarming process, the cryopreserved sample solutions were fully immersed in the pre-warmed, 37 ℃ water bath. The water bath was shaking at 60 RPM in an orbital motion to reduce the temperature gradient within the sample solution. The rewarming process was terminated until the thermal couple reading reached 0 ℃.

Cell membrane integrity was determined by Trypan blue (Life Technologies) staining assay to calculate the Jurkat cells' recovery rate. The live cells would not be colored since the intact cell membrane have a high selectivity to the compounds that traverse the membrane, and Trypan blue is blocked. On the other hand, dead cells would be colored since the dye can penetrate the unfunctional cell membrane. Both live and dead cells can be counted by a cell counter (Countess II, Invitrogen).

6.2.5 *Permeability analysis*

The optimal cooling rate has been observed by cell recovery experiments. Following the “ten percent” restriction, this proportion of the water in the cells is incapable of freezing[98]. This

percentage of water should be left in the cells when the water transportation ended to achieve the cells' optimal recovery. The related cooling rate is the optimal cooling rate for this kind of cell. The faster cooling rate will cause too much water left to generate IIF, lethal to cells. In comparison, the slower cooling rate will induce "solution injury" caused by high intracellular osmolarity[99]. The simulation of water loss during the cooling process is following Mazur-Toner and Arrhenius equations as follows:

$$\frac{dV(T)}{dT} = \frac{ART}{B\bar{v}} L_P(T) * \{[\frac{L}{R}\left(\frac{1}{T_{f,0}} - \frac{1}{T}\right) - ln\left[\frac{V(T)-V_b}{V(T)-V_b+\Phi_s n_s \bar{v}_w}\right]]\} \quad (6.20)$$

$$L_P\ (T) = L_P\left(T_{ref}\right) exp\ [-\frac{E_a}{R}\ \left(\frac{1}{T} - \frac{1}{T_{ref}}\right)] \quad (6.21)$$

Here, A is the cell surface area, R is the universal gas constant, L is the heat of fusion of water, B is the cooling rate, $T_{f,0}$ is the freezing temperature of pure water, V_b is the osmotically inactive cell volume, n_s is the number of moles of salts, $\bar{v}_w$ is the specific molar volume of water, ϕ_s is the dissociation constant (=2 for NaCl), and E_a is the activation energy of L_p.

Following this mechanism, the optimal cooling rate should have corresponded to the 10 percent water residual in the cells. With the L_p at room temperature obtained in Chapter 2 as the reference, E_a can be simulated by iterations.

6.3 RESULTS

6.3.1 *Temperature profiles for different cooling rates*

Figure 6.1 shows the temperature profiles of cooling rates at 0.1, 0.5, and 1 ℃ /min, respectively. The average cooling rate was calculated as 0.10 ± 0.03, 0.48 ± 0.04, and 1.07 ± 0.12 ℃/min. Figure 6.2 shows the temperature profiles of cooling rates at 5, 10, and 20 ℃/ min, respectively. The average cooling rate was 4.8 ± 0.7, 9.6 ± 1.1, and 21.4 ± 1.8 ℃ min for the last half part after the phase change region.

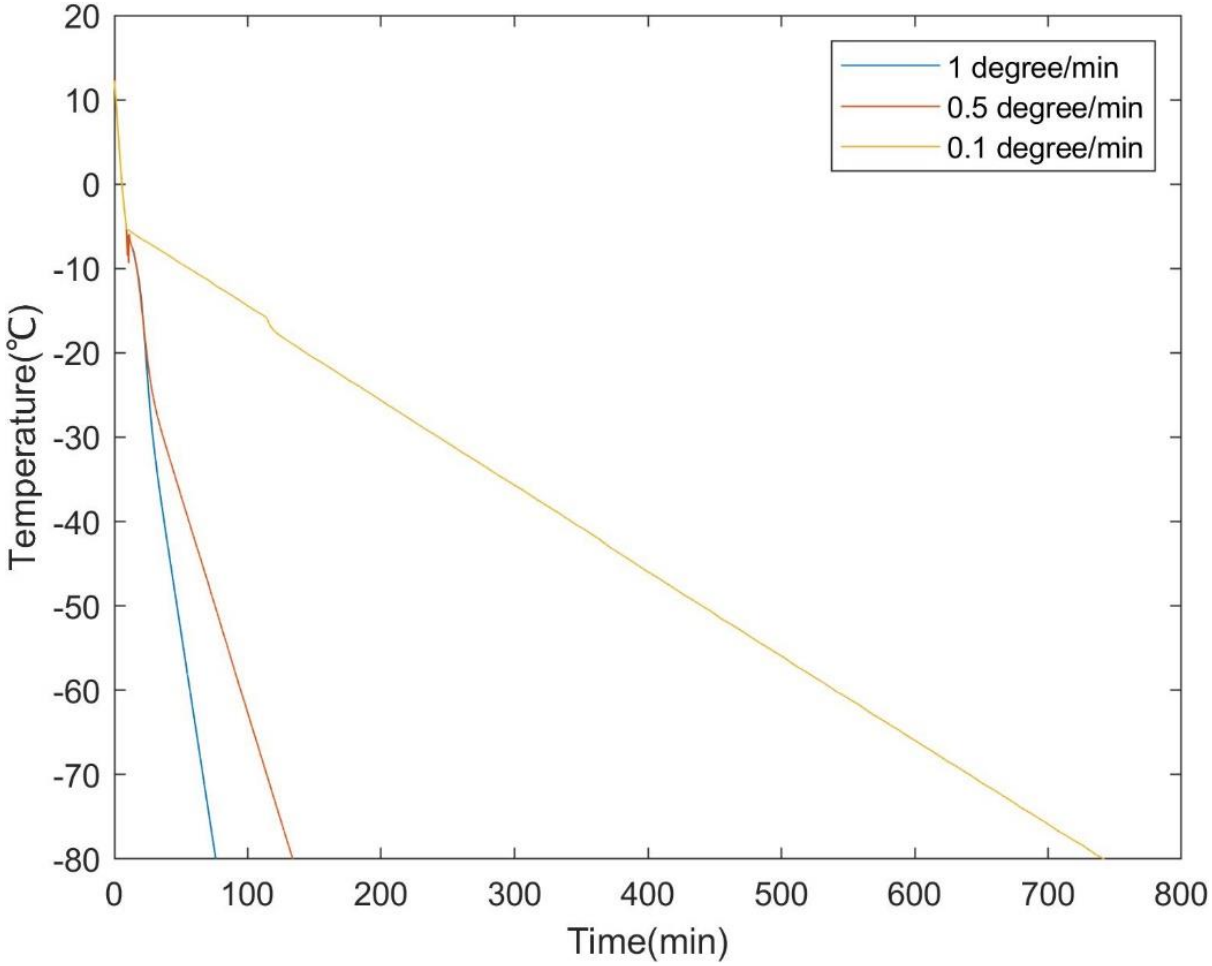

Figure 6.1. Temperature profiles of cooling rates at 0.1, 0.5, and 1 ℃ /min

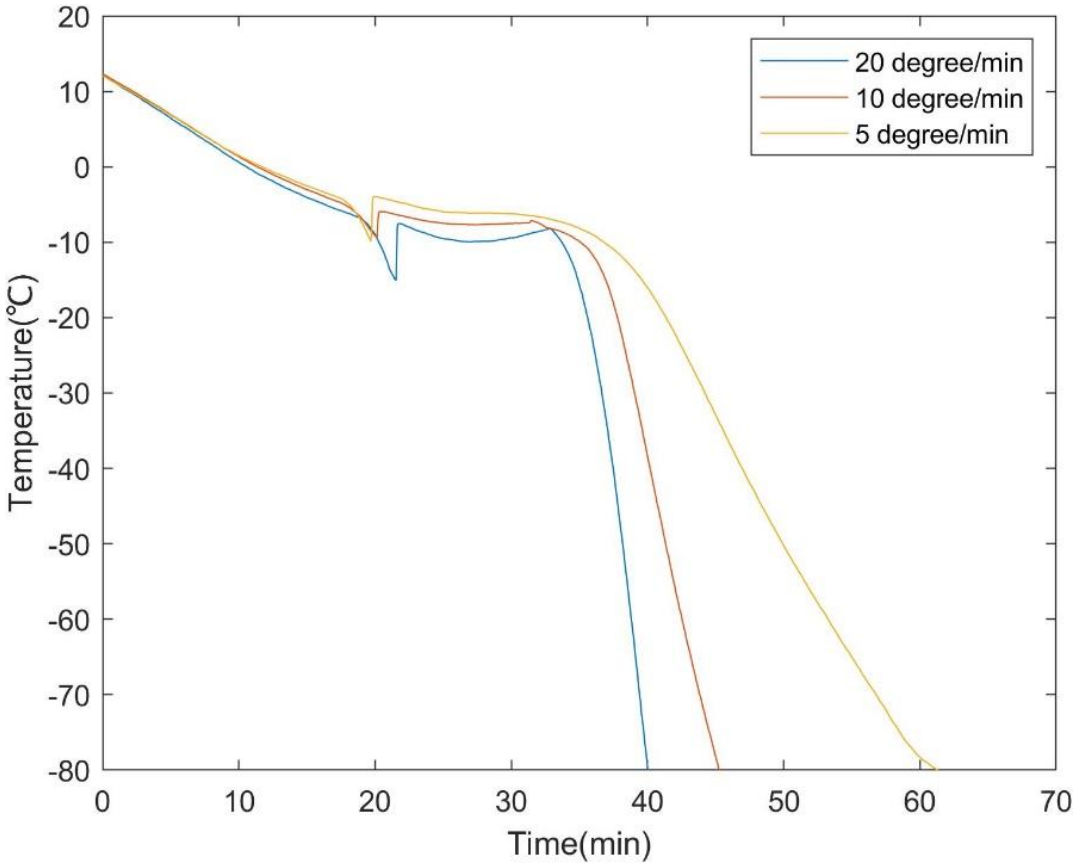

Figure 6.2. Temperature profiles of cooling rates at 20, 10, and 5 ℃ /min

6.3.2 *Cell recovery rate with different cooling rates*

The recovery rates of Jurkat cells of different cooling rates are shown in Figure 6.3. The recovery rates of the 0.1, 0.5, and1 ℃ /min group are $6.03\pm4.16\%$ (N=8), $12.39\pm7.47\%$ (N=8), and $83.18\pm4.51\%$ (N=14), respectively. The recovery rates of the 5, 10, and 20 ℃ /min group are $80.79\pm10.05\%$ (N=16), $53.33\pm10.9\%$ (N=20), and $20.93\pm3.29\%$ (N=10). The recovery rates of 5, 10, and 20 ℃ /min groups were updated as 1.19, 1.51, and 1.71 ℃ /min for theoretical analysis, shown as Figure 6.3b.

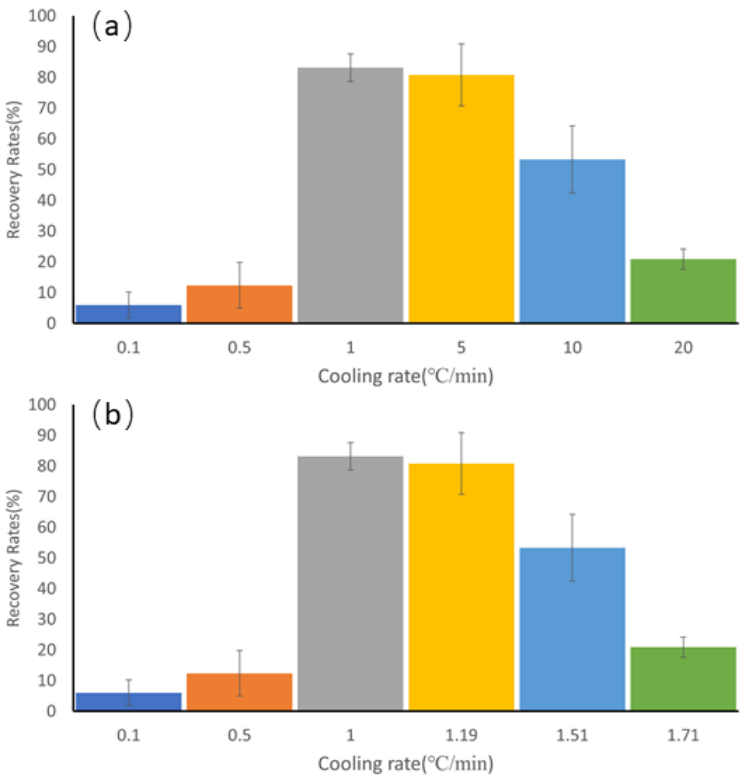

Figure 6.3. The recovery rate of Jurkat cells with different cooling rates: (a).Original cooling rates based on freezer setting. (b) Updated cooling rates.

6.3.3 *Determination of Ea based on water loss model during the cooling process*

To follow the "10 percent" restriction, the residual intracellular water of optimal cooling rate observed by biological experiments(1 ℃ /min) should be around 10 %. The simulated Ea is 27.53 kcal/mol. With calculated Ea, the water loss curve during the cooling processes with different cooling rates was plotted in Figure 6.4. The curves with a cooling rate lower than 1 ℃ /min lost more than 95% intracellular water before -10 ℃. The curves with a cooling rate higher than 5 ℃ /min had more than 81.9% intracellular water left. The residual intracellular water with updated cooing rates(1.19, 1.51, and 1.71 ℃ /min) was between 24.2% to 47.1%.

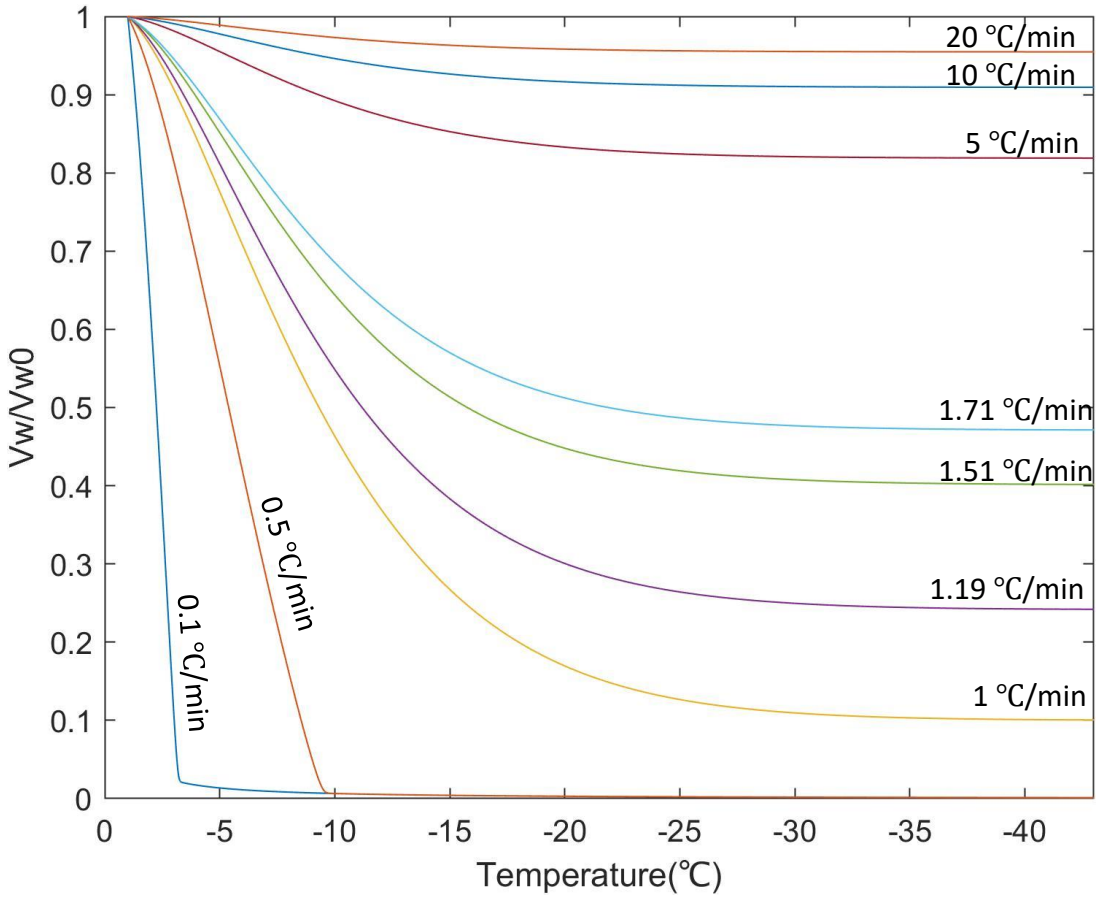

Figure 6.4. Water loss curves during the cooling process with Ea = 27.53 kcal/mol

6.4 DISCUSSION

This study used the cell recovery rate results to calculate the activation energy of cell membrane permeability to water under the "10 percent" restriction and "Two-factor Hypothesis". The optimal cooling rate should neither be too fast to leave too much intracellular water resulting in IIF nor too slow to induce long-time high intracellular osmolarity to cause "solution injury". Calculated subzero Ea can be employed for various research, including L_p at different subzero temperatures, the cooling protocol for different sample sizes, theoretical analysis of water transportation, etc.

According to the cell recovery rate experiments, 1 ℃ /min was observed as the optimal cooling rate for Jurkat cells. In this case, the residual intracellular water with 1 ℃ /min should be 10% of the initial intracellular free water, following the "10 percent" restriction and "Two-factor Hypothesis"[88-89]. The E_a in the cooling process was calculated with Mazur-Toner's water transport model and the Arrhenius equation, equal to 27.53 kcal/mol. The water loss curves during the cooling process with different cooling rates were plotted then.

However, according to Figure 6.4, the cooling rate larger than 5 ℃ /min had more than 81.9% intracellular water left, resulting in severe IIF. The recovery rates of these high cooling rates should not be such high. The method to calculate the average cooling rate of 5, 10, and 20℃ /min groups is needed to be modified after reviewing the protocol. The water transportation across the cell membrane started when the shift happened, the extracellular ice started formatting, and ended around -35℃, the eutectic temperature of the sample solution. Under the IIF mechanism, only the cooling rate in this region should be considered the theoretical analysis parameters. In this case, updated average cooling rates of original 5, 10, and 20 ℃/min groups were recalculated, shown in Table 6-7, and worked as the parameters in the cell recovery rate and activation energy analysis. The water loss curves with updated cooling rates were also plotted in Figure 6.4. The residual intracellular water of these three cooling rates varies from 24.2% to 47.1%. The coupled results of updated cooling rates, water loss curves, and recovery rates verified the credibility of the method proposed by this study.

The values of E_a at subzero temperature for different cell types have been reported by other scientists with different methods, including cryomicroscopy method, calorimetric method, and an inverse method[100] study. A summary has been shown in Table 6.8. for both E_a above and below 0℃.

Table 6.9: Published activation energies(E_a) for water permeability(L_p)

Cell type	Medium	$E_a \geq 0$	Reference	Subzero E_a	Reference
Yeast	Water			11-16	[101]
Monocytes	PBS			14.6	[102]
				52.2	[69]
	DMSO			39.7	[102]
Granulocytes	PBS	14-18	[103]		
Keratinocytes	PBS			10.7	[104]
Dermal fibroblasts	PBS			39-43	[105]
Hepatocytes	PBS			19.6	[106]
				18-81	[107]
				18-102	[108]
				18	[109]
	DMSO			28	[109]
Drosophila eggs	PBS	8-18	[110]	39	[111]
Mouse oocytes	PBS	14.5	[112]	13.3	[113]
		11.4	[114]	19.3	[115]
		12.3	[116]		
	EG	14	[117]	21	[100]
Lymphocytes	PBS	13	[103]	15.5	[118]
		7.1	[27]	11.1	[69]
	DMSO	9.6	[27]		

Comparing E_a from previous literature, some trends can be found. Firstly, the suprazero Ea about typically smaller than the subzero E_a for the same cells in the same medium. In this case, it is not correct to assume that suprazero E_a can be applied below 0℃ [100]. What's more, the E_a usually is larger when CPA and salts co-exist and smaller when no CPA exists [27,100]. In our study, the subzero E_a of Jurkat cell, one kind of lymphocyte, was determined as 27.53 kcal/mol in the presence of DMSO and salts. Compared with the suprazero E_a of lymphocyte, 9.6 kcal/mol when DMSO and salts co-exist, and subzero E_a of lymphocyte, 11.1-15.5 kcal/mol when no CPA exits, the value obtained in this study is very reasonable.

According to the modified cooling rates and related cell recovery rates, the cooling rate is critical during cryopreservation. As shown in Figure 6.4, the minor change of cooling rates will make a massive difference in cell recovery rates. It can be concluded that the investigation of the optimal cooling rates is essential.

6.5 CONCLUSION

In conclusion, an inverse method to determine the subzero L_p and E_a with cell recovery rate results and water transport model was proposed. The subzero of L_p and E_a of Jurkat cells were determined and compared with previous literature. The reasonable results show the assumption that suprazero cell membrane permeability values can be extrapolated to subzero temperatures are not correct. The proposed method reduces the demand for expensive equipment and labor work. The results also indicate the importance of the cooling rate during cryopreservation.

Chapter 7. SUMMARY AND FUTURE WORK

7.1 SUMMARY

Cryopreservation, storing biological materials at low temperatures (e.g., in liquid nitrogen), has been employed to preserve DNA/RNA, cells, tissues, organs, etc., for decades by slowing down any chemical reactions and metabolism. This technology and science benefits biobanking, cellular therapy, academic/clinical research, and so on. However, to successfully cryopreserve biological materials, many challenges are needed to be overcome. Explicitly speaking, challenges include selecting the optimal CPAs, addition, and removal of CPA, optimization of cooling and warming protocols. The optimal cryopreservation protocol of biological materials is determined by cell-type-specific cryobiological characteristics. In this dissertation, some novel technology, approaches, and devices were developed to determine these fundamental properties and solve these challenges in cryopreservation.

To determine cell membrane properties, two novel microfluidic devices were developed. A multiphysics simulation of three-dimensional laminar flow conjugated heat transfer, coupled with Joule heating, was conducted. A microfluidic device with on-chip cooling/heating mechanism, enabling precise and stable temperature control, was fabricated. The temperature control stability and response were tested and demonstrated. This platform achieves the following features: (1) hydrodynamic confinement of single-cell; (2) switching extracellular medium during the cell trapping; (3) controlling surrounding medium temperature from 2 ℃ to 37℃.

Secondly, a simplified microfluidic device was developed and employed to determine the cell membrane permeability at room temperature. A microfluidic chip with a block structure was used to achieve steady trapping. The cell volume excursion by a high-speed camera and the cell membrane permeability of Jurkat cells to water and CPA (DMSO) were determined through

simulation and image processing analysis. The measured properties would be used to generate optimal cryopreservation protocols for Jurkat cells. Potential research can also be inspired by the results, such as exploring optimal CPAs (high Permeability and low toxicity) and optimizing the CPA addition and removal process.

A multifunctional cell processing system and related auto-generated CPA removal protocol were developed to achieve both CPA removal and cell concentration functions. Applying optional hypertonic dilution and an advanced algorithm with cell properties, determined by devices discussed above, as parameters, the optimal CPA removal approach will be generated to minimize cell shrinkage and swelling during the post-cryopreservation process. Compared with the traditional centrifuge method, this novel system/method can provide a sterile, automatic, and less osmotic/mechanical injury option for academic and clinical research. This system will be further employed in the CPA addition process.

The multifunctional cell processing system and related algorithms' developments provide a powerful tool to solve the problems during CPA addition and removal. The other two essential processes, cooling, and warming, have been quantized and optimized.

For the heating process, heat transfer models for the water-bath and natural air rewarming process for the large sample were developed and validated by the experiment. The validated models were then employed to calculate the temperature gradients spatially and temporally. The temperature gradients results showed that natural air rewarming is a better method for tissue and organ cryopreservation, which has relatively more minor thermal stress during rewarming. Some suggestions about the sample's location in the container and the size of the container were also discussed.

For the cooling process, an inverse method to determine the subzero L_p and E_a with cell recovery rate results and water transport model was proposed. The subzero of L_p and E_a of Jurkat cells were determined and compared with previous literature. The reasonable results show the assumption that suprazero cell membrane permeability values can be extrapolated to subzero temperatures are not correct. The proposed method reduces the demand for expensive equipment and labor work.

With cryobiological cell characteristics determined by proposed devices and methods, the comprehensive models covering CPA loading/unloading, cooling, and warming build a clear structure for cryopreservation and its research. The biological experiments and cryopreservation performance can be predicted, quantized, and further improved with these models and devices.

7.2 FUTURE WORK

This dissertation has proposed a few novel methods and devices for the analysis and application of cryopreservation. Some work is still needed to achieve further improvements.

Firstly, the microfluidic device proposed in chapter two achieved fluid and temperature control for single-cell analysis. Some cell experiments have been done but not enough to be published. Because of the complexity of the device setup, the success rate is still not very high. The simplification of the setup and more biological experiments are desired for this microfluidic device since the cell membrane properties at suprazero temperature are more valuable than the ones at room temperature, measured by the simplified device in chapter three. The cell membrane permeabilities above zero degrees are mainly employed to select the optimal CPAs and optimize the CPA addition and removal process, which are typically operated on ice to reduce the heat release caused by CPA dissolving. On the other hand, the cytotoxicity of CPA is more severe at a

higher temperature. In this case, the robust microfluidic device at suprazero temperature would be more desirable for researchers.

According to the analysis in chapter four, the interesting relationships among cell membrane permeabilities to water(L_p) and CPA(P_s), cell diameter(D), and inactive volume(V_b) have been noticed. Combining these four parameters determined the water and CPA transportation during all four essential procedures of cryopreservation(CPA addition/removal, cooling, and warming). On the other hand, these biological properties have determined cells' ability to stand cryoinjury from the very beginning. It might explain why certain cells are extremely hard to be cryopreserved, and other kinds of cells are very robust. It also provides another potential approach to cryopreserve some valuable and sensitive cells by modifying their membrane permeabilities with biological, physical, or chemical methods. Or that is the mechanism of some of the current supplemental CPAs like trehalose. This new cryopreservation theory will be further probed and investigated with theoretical analysis and biological experiments in future work.

Besides the previous discussion about mass transfer, cryopreservation is also a science about heat transfer, especially for the cooling and warming process. Heat transfer models have been proposed in chapter five about the warming process and applied to thermal stress analysis. However, the analysis stopped at the comparison of the temperature gradients. It can be more quantitative if more mechanical parameters, including thermal expansion coefficient, are employed for further stress simulation. Other scientists have discussed the model about cooling process including the difficulty caused by supercooling, but it still needed to be further improved in future work.

On the other hand, electromagnetic rewarming has been regarded as one of the most promising technology for large sample rewarming benefited by its volumetric heating mechanism[119]. This

method can rapidly and uniformly rewarm large samples to achieve an optimal recovery rate. The simulation of the heat transfer process coupled with the resonance of electromagnetic waves is very complex and desired.

As mentioned in chapter six, the subzero cell membrane properties are significant during the analysis of cooling. However, the current DSC method by measuring heat flow difference during two cooling steps is restricted by the supercooling. One solution is to add Pseudomonas syringae, one kind of bacteria, as the nucleator to reduce supercooling. It highly increases the experiment time and complexity. Meanwhile, the added Pseudomonas syringae may change the thermal-physical properties of cell suspension as well. There are two potential approaches to solve this problem. Firstly, the constant latent heat of the given sample during cooling makes it possible to predict the heat flow curve using machine learning technology. In this method, supercooling is acceptable, and the heat flow curve will be predicted with the model trained by cooling profiles with different freezing points. On the other hand, it might be possible to use the warming heat flow curves to obtain cell volume profiles, during which there is no obstruction of supercooling.

Reference

[1] D. Gao and J. K. Critser, “Mechanisms of cryoinjury in living cells,” *ILAR J.*, 2000, doi: 10.1093/ilar.41.4.187.

[2] C. Polge, A. U. Smith, and A. S. Parkes, “Revival of spermatozoa after vitrification and dehydration at low temperatures [12],” *Nature*. 1949, doi: 10.1038/164666a0.

[3] R. Cordoba, R. Arrieta, A. Kerguelen, and F. Hernandez-Navarro, “The occurrence of adverse events during the infusion of autologous peripheral blood stem cells is related to the number of granulocytes in the leukapheresis product,” *Bone Marrow Transplant.*, 2007, doi: 10.1038/sj.bmt.1705861.

[4] A. M. Bakken, O. Bruserud, and J. F. Abrahamsen, “No differences in colony formation of peripheral blood stem cells frozen with 5% or 10% dimethyl sulfoxide,” *J. Hematotherapy Stem Cell Res.*, 2003, doi: 10.1089/152581603322023089.

[5] J. D. Hidalgo *et al.*, “Supraventricular tachyarrhythmias after hematopoietic stem cell transplantation: Incidence, risk factors and outcomes,” *Bone Marrow Transplant.*, 2004, doi: 10.1038/sj.bmt.1704623.

[6] A. Donmez, M. Tombuloglu, A. Gungor, N. Soyer, G. Saydam, and S. Cagirgan, “Clinical side effects during peripheral blood progenitor cell infusion,” *Transfus. Apher. Sci.*, 2007, doi: 10.1016/j.transci.2006.05.019.

[7] G. A. Martín-Henao *et al.*, “Adverse reactions during transfusion of thawed haematopoietic progenitor cells from apheresis are closely related to the number of granulocyte cells in the leukapheresis product,” *Vox Sang.*, 2010, doi: 10.1111/j.1423-0410.2010.01341.x.

[8] F. O. Mueller, T. A. Casey, and P. D. Trevor-Roper, “Use of Deep-frozen Human Cornea in Full-thickness Grafts,” *Br. Med. J.*, 1964, doi: 10.1136/bmj.2.5407.473.

[9] B. Calmels, P. Houzé, J. C. Hengesse, T. Ducrot, C. Malenfant, and C. Chabannon, “Preclinical evaluation of an automated closed fluid management device: Cytomate™, for washing out DMSO from hematopoietic stem cell grafts after thawing,” *Bone Marrow Transplant.*, 2003, doi: 10.1038/sj.bmt.1703905.

[10] A. Sputtek, “Cryopreservation of red blood cells and platelets.,” *Methods in molecular biology (Clifton, N.J.)*. 2007, doi: 10.1007/978-1-59745-362-2_20.

[11] D. Y. Gao, E. Ashworth, P. F. Watson, F. W. Kleinhans, P. Mazur, and J. K. Critser, “Hyperosmotic tolerance of human spermatozoa: Separate effects of glycerol, sodium chloride, and sucrose on spermolysis,” *Biol. Reprod.*, 1993, doi: 10.1095/biolreprod49.1.112.

[12] C. Chen, “PREGNANCY AFTER HUMAN OOCYTE CRYOPRESERVATION,” *Lancet*, 1986, doi: 10.1016/S0140-6736(86)90989-X.

[13] A. Demirol, S. Guven, M. Benkhalifa, T. Sari, and T. Gurgan, “Successful birth following transfer of frozen-thawed embryos produced from in-vitro matured oocytes,” *Reprod. Biomed. Online*, 2010, doi: 10.1016/j.rbmo.2010.04.020.

[14] B. Diener, D. Utesch, N. Beer, H. Dürk, and F. Oesch, “A method for the cryopreservation of liver parenchymal cells for studies of xenobiotics,” *Cryobiology*, 1993, doi: 10.1006/cryo.1993.1011.

[15] Z. Shu, D. Gao, and L. L. Q. Pu, “Update on cryopreservation of adipose tissue and adipose-derived stem

cells," *Clinics in Plastic Surgery*. 2015, doi: 10.1016/j.cps.2014.12.001.

[16] G. Zhao and J. Fu, "Microfluidics for cryopreservation," *Biotechnology Advances*. 2017, doi: 10.1016/j.biotechadv.2017.01.006.

[17] J. Farrant, C. A. Walter, H. Lee, and L. E. McGann, "Use of two-step cooling procedures to examine factors influencing cell survival following freezing and thawing," *Cryobiology*, 1977, doi: 10.1016/0011-2240(77)90176-6.

[18] P. Mazur and J. J. Schmidt, "Interactions of cooling velocity, temperature, and warming velocity on the survival of frozen and thawed yeast," *Cryobiology*, 1968, doi: 10.1016/S0011-2240(68)80138-5.

[19] P. Mazur, "The role of intracellular freezing in the death of cells cooled at supraoptimal rates," *Cryobiology*, 1977, doi: 10.1016/0011-2240(77)90175-4.

[20] P. Mazur, "Freezing of living cells: mechanisms and implications.," *The American journal of physiology*. 1984, doi: 10.1152/ajpcell.1984.247.3.C125.

[21] J. E. Lovelock and M. W. H. Bishop, "Prevention of freezing damage to living cells by dimethyl sulphoxide," *Nature*, 1959, doi: 10.1038/1831394a0.

[22] K. Aita *et al.*, "Apoptosis in murine lymphoid organs following intraperitoneal administration of dimethyl sulfoxide (DMSO)," *Exp. Mol. Pathol.*, 2005, doi: 10.1016/j.yexmp.2005.07.001.

[23] R. Pal, M. K. Mamidi, A. K. Das, and R. Bhonde, "Diverse effects of dimethyl sulfoxide (DMSO) on the differentiation potential of human embryonic stem cells," *Arch. Toxicol.*, 2012, doi: 10.1007/s00204-011-0782-2.

[24] P. Mazur, "Equilibrium, quasi-equilibrium, and nonequilibrium freezing of mammalian embryos," *Cell Biophys.*, 1990, doi: 10.1007/BF02989804.

[25] P. Mazur, "Cryobiology: The freezing of biological systems," *Science*. 1970, doi: 10.1126/science.168.3934.939.

[26] H. hung Chen *et al.*, "A microfluidic study of mouse dendritic cell membrane transport properties of water and cryoprotectants," *Int. J. Heat Mass Transf.*, vol. 51, no. 23–24, pp. 5687–5694, 2008, doi: 10.1016/j.ijheatmasstransfer.2008.04.013.

[27] C. Fang, F. Ji, Z. Shu, and D. Gao, "Determination of the temperature-dependent cell membrane permeabilities using microfluidics with integrated flow and temperature control," *Lab Chip*, 2017, doi: 10.1039/C6LC01523A.

[28] H. Y. Tseng, S. Sun, Z. Shu, W. Ding, J. A. Reems, and D. Gao, "A microfluidic study of megakaryocytes membrane transport properties to water and dimethyl sulfoxide at suprazero and subzero temperatures," *Biopreserv. Biobank.*, 2011, doi: 10.1089/bio.2011.0027.

[29] S. M. Hughes *et al.*, "Cryopreservation of human mucosal leukocytes," *PLoS One*, 2016, doi: 10.1371/journal.pone.0156293.

[30] Y. Ghetler, S. Yavin, R. Shalgi, and A. Arav, "The effect of chilling on membrane lipid phase transition in human oocytes and zygotes," *Hum. Reprod.*, 2005, doi: 10.1093/humrep/dei236.

[31] D. Papahadjopoulos, K. Jacobson, S. Nir, and I. Isac, "Phase transitions in phospholipid vesicles

Fluorescence polarization and permeability measurements concerning the effect of temperature and cholesterol," *BBA - Biomembr.*, 1973, doi: 10.1016/0005-2736(73)90314-3.

[32] X. Zhou, Z. Liu, X. M. Liang, Z. Shu, P. Du, and D. Gao, "Theoretical investigations of a novel microfluidic cooling/warming system for cell vitrification cryopreservation," *Int. J. Heat Mass Transf.*, 2013, doi: 10.1016/j.ijheatmasstransfer.2013.06.022.

[33] Z. Zhou, J. Shi, H. H. Chen, S. R. Schafer, and C. L. Chen, "Two-phase flow over flooded micro-pillar structures with engineered wettability pattern," *Int. J. Heat Mass Transf.*, 2014, doi: 10.1016/j.ijheatmasstransfer.2013.12.057.

[34] G. Velve Casquillas *et al.*, "Fast microfluidic temperature control for high resolution live cell imaging," *Lab Chip*, 2011, doi: 10.1039/c0lc00222d.

[35] K. Lian *et al.*, "Integrated microfluidic components on a printed wiring board platform," *Sensors Actuators, B Chem.*, 2009, doi: 10.1016/j.snb.2009.01.071.

[36] D. Resnik, D. Vrtačnik, M. Možek, B. Pečar, and S. Amon, "Experimental study of heat-treated thin film Ti/Pt heater and temperature sensor properties on a Si microfluidic platform," *J. Micromechanics Microengineering*, 2011, doi: 10.1088/0960-1317/21/2/025025.

[37] H. Yang, C. A. Choi, K. H. Chung, C. H. Jun, and Y. T. Kim, "An Independent, Temperature-Controllable Microelectrode Array," *Anal. Chem.*, 2004, doi: 10.1021/ac035270p.

[38] A. I. K. Lao, T. M. H. Lee, I. M. Hsing, and N. Y. Ip, "Precise temperature control of microfluidic chamber for gas and liquid phase reactions," *Sensors Actuators, A Phys.*, 2000, doi: 10.1016/S0924-4247(99)00356-8.

[39] K. S. Lee, P. Boccazzi, A. J. Sinskey, and R. J. Ram, "Microfluidic chemostat and turbidostat with flow rate, oxygen, and temperature control for dynamic continuous culture," *Lab Chip*, 2011, doi: 10.1039/c1lc20019d.

[40] V. Bazargan and B. Stoeber, "Flow control using a thermally actuated microfluidic relay valve," *J. Microelectromechanical Syst.*, 2010, doi: 10.1109/JMEMS.2010.2067195.

[41] H. Bridle, M. Millingen, and A. Jesorka, "On-chip fabrication to add temperature control to a microfluidic solution exchange system," *Lab Chip*, 2008, doi: 10.1039/b718368b.

[42] L. Liu, S. Peng, W. Wen, and P. Sheng, "Micro thermoindicators and optical-electronic temperature control for microfluidic applications," *Appl. Phys. Lett.*, 2007, doi: 10.1063/1.2776848.

[43] J. D. Adams, C. L. Ebbesen, R. Barnkob, A. H. J. Yang, H. T. Soh, and H. Bruus, "High-throughput, temperature-controlled microchannel acoustophoresis device made with rapid prototyping," *J. Micromechanics Microengineering*, 2012, doi: 10.1088/0960-1317/22/7/075017.

[44] A. Y. C. Liu, H. Bian, L. E. Huangi, and Y. K. Lee, "Transient cold shock induces the heat shock response upon recovery at 37 °C in human cells," *J. Biol. Chem.*, 1994, doi: 10.1016/s0021-9258(17)36691-7.

[45] L.-Y. Hsu and C. E. Nordman, "Phase Transition and Crystal Structure of the 37 ° C Form of Cholesterol," *Science (80-.).*, vol. 220, no. 4597, pp. 604–606, 1983.

[46] U. Łapińska, G. Glover, P. Capilla-Lasheras, A. J. Young, and S. Pagliara, "Bacterial ageing in the absence

of external stressors," *Philos. Trans. R. Soc. B Biol. Sci.*, 2019, doi: 10.1098/rstb.2018.0442.

[47] S. Pagliara, S. L. Dettmer, and U. F. Keyser, "Channel-facilitated diffusion boosted by particle binding at the channel entrance," *Phys. Rev. Lett.*, 2014, doi: 10.1103/PhysRevLett.113.048102.

[48] E. M. Nestorovich, C. Danelon, M. Winterhalter, and S. M. Bezrukov, "Designed to penetrate: Time-resolved interaction of single antibiotic molecules with bacterial pores," *Proc. Natl. Acad. Sci. U. S. A.*, 2002, doi: 10.1073/pnas.152206799.

[49] S. Gravelle, L. Joly, F. Detcheverry, C. Ybert, C. Cottin-Bizonne, and L. Bocquet, "Optimizing water permeability through the hourglass shape of aquaporins," *Proc. Natl. Acad. Sci. U. S. A.*, 2013, doi: 10.1073/pnas.1306447110.

[50] J. J. McGrath, "Quantitative measurement of cell membrane transport: Technology and applications," *Cryobiology*, 1997, doi: 10.1006/cryo.1997.2013.

[51] D. Y. Gao, J. J. McGrath, J. Tao, C. T. Benson, E. S. Critser, and J. K. Critser, "Membrane transport properties of mammalian oocytes: A micropipette perfusion technique," *J. Reprod. Fertil.*, 1994, doi: 10.1530/jrf.0.1020385.

[52] J. J. McGrath, "A microscope diffusion chamber for the determination of the equilibrium and non-equilibrium osmotic response of individual cells," *J. Microsc.*, 1985, doi: 10.1111/j.1365-2818.1985.tb02641.x.

[53] F. Guo *et al.*, "Three-dimensional manipulation of single cells using surface acoustic waves," *Proc. Natl. Acad. Sci. U. S. A.*, 2016, doi: 10.1073/pnas.1524813113.

[54] D. R. Gossett *et al.*, "Hydrodynamic stretching of single cells for large population mechanical phenotyping," *Proc. Natl. Acad. Sci. U. S. A.*, 2012, doi: 10.1073/pnas.1200107109.

[55] S. Pagliara *et al.*, "Transition from pluripotency in embryonic stem cells distinguished by an auxetic nucleus," *Nat. Mater.*, 2015.

[56] R. A. Bamford, A. Smith, J. Metz, G. Glover, R. W. Titball, and S. Pagliara, "Investigating the physiology of viable but non-culturable bacteria by microfluidics and time-lapse microscopy," *BMC Biol.*, 2017, doi: 10.1186/s12915-017-0465-4.

[57] A. S. Verkman *et al.*, "Water transport across mammalian cell membranes," *American Journal of Physiology - Cell Physiology*. 1996, doi: 10.1152/ajpcell.1996.270.1.c12.

[58] H. M. Ji, V. Samper, Y. Chen, C. K. Heng, T. M. Lim, and L. Yobas, "Silicon-based microfilters for whole blood cell separation," *Biomed. Microdevices*, 2008, doi: 10.1007/s10544-007-9131-x.

[59] O. Kedem, "Commentary on 'Thermodynamic analysis of the permeability of biological membranes to non-electrolytes' by O. Kedem and A. Katchalsky Biochim. Biophys. Acta 27 (1958) 229-246," *BBA - Biochim. Biophys. Acta*, 1989, doi: 10.1016/s0006-3002(89)80036-8.

[60] D. R. Gossett *et al.*, "Label-free cell separation and sorting in microfluidic systems," *Analytical and Bioanalytical Chemistry*. 2010, doi: 10.1007/s00216-010-3721-9.

[61] H. hung Chen, J. J. P. Purtteman, S. Heimfeld, A. Folch, and D. Gao, "Development of a microfluidic device for determination of cell osmotic behavior and membrane transport properties," *Cryobiology*, vol. 55,

no. 3, pp. 200–209, 2007, doi: 10.1016/j.cryobiol.2007.08.001.

[62] D. Di Carlo, L. Y. Wu, and L. P. Lee, “Dynamic single cell culture array,” *Lab Chip*, 2006, doi: 10.1039/b605937f.

[63] Y. S. Heo *et al.*, “Controlled loading of cryoprotectants (CPAs) to oocyte with linear and complex CPA profiles on a microfluidic platform,” *Lab Chip*, vol. 11, no. 20, pp. 3530–3537, 2011, doi: 10.1039/c1lc20377k.

[64] I. K. Dimov, L. Basabe-Desmonts, J. L. Garcia-Cordero, B. M. Ross, A. J. Ricco, and L. P. Lee, “Stand-alone self-powered integrated microfluidic blood analysis system (SIMBAS),” *Lab Chip*, 2011, doi: 10.1039/c0lc00403k.

[65] J. Liu, S. Li, and D. Mitra, “Multiphysical phenomenon of air bubble growth in polydimethylsiloxane channel corners under microfluidic negative pressure-driven flow,” *Int. J. Heat Mass Transf.*, 2015, doi: 10.1016/j.ijheatmasstransfer.2015.08.006.

[66] Q. Zhu *et al.*, “Digital PCR on an integrated self-priming compartmentalization chip,” *Lab Chip*, 2014, doi: 10.1039/c3lc51327k.

[67] A. M. Vian and A. Z. Higgins, “Membrane permeability of the human granulocyte to water, dimethyl sulfoxide, glycerol, propylene glycol and ethylene glycol,” *Cryobiology*, 2014, doi: 10.1016/j.cryobiol.2013.11.004.

[68] Z. Shu *et al.*, “A study of the osmotic characteristics, water permeability, and cryoprotectant permeability of human vaginal immune cells,” *Cryobiology*, 2016, doi: 10.1016/j.cryobiol.2016.03.003.

[69] Z. Shu, “Development of Optimal Biopreservation Methods and Technology for Cellular Therapy and Clinical Diagnosis,” University of Washington, 2013.

[70] F. Arnaud, E. Kapnik, and H. T. Meryman, “Use of hollow fiber membrane filtration for the removal of DMSO from platelet concentrates,” *Platelets*, vol. 14, no. 3, pp. 131–137, 2003, doi: 10.1080/0953710031000092811.

[71] W. Ding, J. Yu, E. Woods, S. Heimfeld, and D. Gao, “Simulation of removing permeable cryoprotective agents from cryopreserved blood with hollow fiber modules,” *J. Memb. Sci.*, vol. 288, no. 1–2, pp. 85–93, 2007, doi: 10.1016/j.memsci.2006.11.007.

[72] W. Ding, X. Zhou, S. Heimfeld, J. A. Reems, and D. Gao, “A steady-state mass transfer model of removing CPAs from cryopreserved blood with hollow fiber modules,” *J. Biomech. Eng.*, vol. 132, no. 1, pp. 1–7, 2010, doi: 10.1115/1.4000110.

[73] W. Ding, S. Sun, C. Liu, S. Heimfeld, and D. Gao, “A random method for theoretical estimation of RBC osmotic damage in removing CPAs from cryopreserved blood with hollow fiber modules: Closed-loop blood flow mode,” *J. Memb. Sci.*, vol. 360, no. 1–2, pp. 17–25, 2010, doi: 10.1016/j.memsci.2010.04.040.

[74] X. Zhou *et al.*, “A dilution-filtration system for removing cryoprotective agents,” *J. Biomech. Eng.*, vol. 133, no. 2, pp. 1–7, 2011, doi: 10.1115/1.4003317.

[75] H. Qiao, W. Ding, S. Sun, L. Gong, and D. Gao, “Theoretical optimization of the removal of cryoprotective agents using a dilution-filtration system,” *Biomed. Eng. Online*, vol. 13, no. 1, pp. 1–11, 2014, doi:

10.1186/1475-925X-13-120.

[76] J. Liu *et al.*, “Deglycerolization of red blood cells: A new dilution-filtration system,” *Cryobiology*, vol. 81, no. January, pp. 160–167, 2018, doi: 10.1016/j.cryobiol.2018.01.006.

[77] M. J. Rosenbluth, W. A. Lam, and D. A. Fletcher, “Force microscopy of nonadherent cells: A comparison of leukemia cell deformability,” *Biophys. J.*, vol. 90, no. 8, pp. 2994–3003, 2006, doi: 10.1529/biophysj.105.067496.

[78] Zhijie Liao, “Numerical and experimetnal studies of mass transfer in artificial kidney and hemodialysis,” University of Kentucky, 2554.

[79] T. Yang, J. Peng, Z. Shu, P. K. Sekar, S. Li, and D. Gao, “Determination of the membrane transport properties of jurkat cells with a microfluidic device,” *Micromachines*, vol. 10, no. 12, pp. 1–13, 2019, doi: 10.3390/mi10120832.

[80] B. Rubinsky, E. G. Cravalho, and B. Mikic, “Thermal stresses in frozen organs,” *Cryobiology*, 1980, doi: 10.1016/0011-2240(80)90009-7.

[81] B. Rubinsky and E. G. Cravalho, “The determination of the thermal history in a one-dimensional freezing system by a perturbation method,” *J. Heat Transfer*, 1979, doi: 10.1115/1.3450968.

[82] B. Rubinsky and E. G. Cravalho, “ANALYSIS FOR THE TEMPERATURE DISTRIBUTION DURING THE THAWING OF A FROZEN BIOLOGICAL ORGAN.,” 1979.

[83] G. M. Fahy, J. Saur, and R. J. Williams, “Physical problems with the vitrification of large biological systems,” *Cryobiology*, 1990, doi: 10.1016/0011-2240(90)90038-6.

[84] Y. Rabin and P. S. Steif, “Thermal stress modeling in cryosurgery,” *Int. J. Solids Struct.*, 2000, doi: 10.1016/S0020-7683(98)00345-X.

[85] Y. Rabin and P. S. Steif, “Analysis of thermal stresses around a cryosurgical probe,” *Cryobiology*, 1996, doi: 10.1006/cryo.1996.0028.

[86] Y. Rabin, N. Wolmark, and M. J. Taylor, “Thermal Expansion Measurements of Frozen Biological Tissues at Cryogenic Temperatures,” *J. Biomech. Eng.*, 1998, doi: 10.1115/1.2798310.

[87] Y. Rabin and E. Bell, “Thermal expansion measurements of cryoprotective agents. Part I: A new experimental apparatus,” *Cryobiology*, 2003, doi: 10.1016/S0011-2240(03)00042-7.

[88] Y. Rabin and E. Bell, “Thermal expansion measurements of cryoprotective agents. Part II: Measurements of DP6 and VS55, and comparison with DMSO,” *Cryobiology*, 2003, doi: 10.1016/S0011-2240(03)00041-5.

[89] X. He and J. C. Bischof, “Analysis of thermal stress in cryosurgery of kidneys,” *J. Biomech. Eng.*, 2005, doi: 10.1115/1.1934021.

[90] S. Baicu, M. J. Taylor, Z. Chen, and Y. Rabin, “Cryopreservation of carotid artery segments via vitrification subject to marginal thermal conditions: Correlation of freezing visualization with functional recovery,” *Cryobiology*, 2008, doi: 10.1016/j.cryobiol.2008.03.002.

[91] G. Pascual, N. García-Honduvilla, M. Rodríguez, F. Turégano, and J. Bujan, “Effect of the thawing process on cryopreserved arteries,” *Ann. Vasc. Surg.*, 2001, doi: 10.1007/s100160010130.

[92] R. Hilpert, “Wärmeabgabe von geheizten Drähten und Rohren im Luftstrom,” *Forsch. auf dem Gebiete des*

Ingenieurwesens, 1933, doi: 10.1007/BF02719754.

[93] S. W. Churchill and H. H. S. Chu, "Correlating equations for laminar and turbulent free convection from a vertical plate," *Int. J. Heat Mass Transf.*, 1975, doi: 10.1016/0017-9310(75)90243-4.

[94] T. L. Bergman, A. S. Lavine, F. P. Incropera, and D. P. Dewitt, *Fundamentals of Heat and Mass Transfer. 7th Edition*. 2011.

[95] X. M. Liang *et al.*, "High accuracy thermal conductivity measurement of aqueous cryoprotective agents and semi-rigid biological tissues using a microfabricated thermal sensor," *Sci. Rep.*, 2015, doi: 10.1038/srep10377.

[96] S. Ren, "Development of Automatic Electromagnetic Resonance Rewarming System for Cryopreservation of Large-Scale Biomaterials," University of Washington, 2020.

[97] S. Seki and P. Mazur, "The dominance of warming rate over cooling rate in the survival of mouse oocytes subjected to a vitrification procedure," *Cryobiology*, 2009, doi: 10.1016/j.cryobiol.2009.04.012.

[98] T. H. Wood and A. M. Rosenberg, "Freezing in yeast cells," *BBA - Biochim. Biophys. Acta*, 1957, doi: 10.1016/0006-3002(57)90421-3.

[99] P. MAZUR, "KINETICS OF WATER LOSS FROM CELLS AT SUBZERO TEMPERATURES AND THE LIKELIHOOD OF INTRACELLULAR FREEZING.," *J. Gen. Physiol.*, 1963, doi: 10.1085/jgp.47.2.347.

[100] F. W. Kleinhans and P. Mazur, "Determination of the water permeability (Lp) of mouse oocytes at -25 °C and its activation energy at subzero temperatures," *Cryobiology*, 2009, doi: 10.1016/j.cryobiol.2008.12.008.

[101] R. L. Levin, M. Ushiyama, and E. G. Cravalho, "Water permeability of yeast cells at sub-zero temperatures," *J. Membr. Biol.*, 1979, doi: 10.1007/BF01961376.

[102] C. McCaa, K. R. Diller, S. J. Aggarwal, and T. Takahashi, "Cryomicroscopic determination of the membrane osmotic properties of human monocytes at subfreezing temperatures," *Cryobiology*, 1991, doi: 10.1016/0011-2240(91)90046-Q.

[103] H. G. Hempling and S. White, "Permeability of cultured megakaryocytopoietic cells of the rat to dimethyl sulfoxide," *Cryobiology*, 1984, doi: 10.1016/0011-2240(84)90204-9.

[104] S. J. Aggarwal, K. R. Diller, and C. R. Baxter, "Hydraulic permeability and activation energy of human keratinocytes at subzero temperatures," *Cryobiology*, 1988, doi: 10.1016/0011-2240(88)90027-2.

[105] S. K. Balasubramanian, J. C. Bischof, and A. Hubel, "Water transport and IIF parameters for a connective tissue equivalent," *Cryobiology*, 2006, doi: 10.1016/j.cryobiol.2005.09.009.

[106] B. Korniski, T. B. Darr, and A. Hubel, "Subzero osmotic characteristics of intact and disaggregated hepatocyte spheroids," *Cryobiology*, 1999, doi: 10.1006/cryo.1999.2177.

[107] M. L. YARMUSH, M. TONER, J. C. Y. DUNN, A. ROTEM, A. HUBEL, and R. G. TOMPKINS, "Hepatic Tissue Engineering: Development of Critical Technologies," *Ann. N. Y. Acad. Sci.*, 1992, doi: 10.1111/j.1749-6632.1992.tb42588.x.

[108] M. Toner, R. G. Tompkins, E. G. Cravalho, and M. L. Yarmush, "Transport phenomena during freezing of isolated hepatocytes," *AIChE J.*, 1992, doi: 10.1002/aic.690381004.

[109] J. O. Karlsson, E. G. Cravalho, I. H. Borel Rinkes, R. G. Tompkins, M. L. Yarmush, and M. Toner, "Nucleation and growth of ice crystals inside cultured hepatocytes during freezing in the presence of dimethyl sulfoxide," *Biophys. J.*, 1993, doi: 10.1016/S0006-3495(93)81319-5.

[110] T. Te Lin, R. E. Pitt, and P. L. Steponkus, "Osmometric behavior of Drosophila melanogaster embryos," *Cryobiology*, 1989, doi: 10.1016/0011-2240(89)90070-9.

[111] R. E. Pitt, S. P. Myers, T. Te Lin, and P. L. Steponkus, "Subfreezing volumetric behavior and stochastic modeling of intracellular ice formation in Drosophila melanogaster embryos," *Cryobiology*, 1991, doi: 10.1016/0011-2240(91)90009-D.

[112] S. P. Leibo, "Water permeability and its activation energy of fertilized and unfertilized mouse ova," *J. Membr. Biol.*, 1980, doi: 10.1007/BF01868823.

[113] M. Toner, E. G. Cravalho, and D. R. Armant, "Water transport and estimated transmembrane potential during freezing of mouse oocytes," *J. Membr. Biol.*, 1990, doi: 10.1007/BF01868641.

[114] C. T. Benson and J. K. Critser, "Variation of Water Permeability (Lp) and Its Activation Energy (Ea) among Unfertilized Golden Hamster and ICR Murine Oocytes," *Cryobiology*, 1994, doi: 10.1006/cryo.1994.1027.

[115] M. Toner *et al.*, "Nonequilibrium freezing of one-cell mouse embryos. Membrane integrity and developmental potential," *Biophys. J.*, 1993, doi: 10.1016/S0006-3495(93)81562-5.

[116] K. Edashige *et al.*, "Channel-dependent permeation of water and glycerol in mouse morulae," *Biol. Reprod.*, 2006, doi: 10.1095/biolreprod.105.045823.

[117] S. J. Paynter, B. J. Fuller, and R. W. Shaw, "Temperature dependence of Kedem-Katchalsky membrane transport coefficients for mature mouse oocytes in the presence of ethylene glycol," *Cryobiology*, 1999, doi: 10.1006/cryo.1999.2199.

[118] R. V. Devireddy, D. Raha, and J. C. Bischof, "Measurement of Water Transport during Freezing in Cell Suspensions Using a Differential Scanning Calorimeter," *Cryobiology*, 1998, doi: 10.1006/cryo.1997.2071.

[119] J. Pan *et al.*, "Towards uniform and fast rewarming for cryopreservation with electromagnetic resonance cavity: numerical simulation and experimental investigation," *Appl. Therm. Eng.*, vol. 140, no. May, pp. 787–798, 2018, doi: 10.1016/j.applthermaleng.2018.05.015.